Numerical and Experimental Investigation of Thermocapillary Pumping in Closed-End Microchannels for Micro Heat Engines

by

P. Stephen Glockner, M.Sc., E.I.T.

A thesis

presented to the University of Manitoba

in fulfilment of the

thesis requirement for the degree of

Doctor of Philosophy

in

Mechanical and Manufacturing Engineering

Winnipeg, Manitoba, Canada 2006

THE UNIVERSITY OF MANITOBA

FACULTY OF GRADUATE STUDIES

*****

COPYRIGHT PERMISSION

Numerical and Experimental Investigation of Thermocapillary Pumping in Closed-End Microchannels for Micro Heat Engines

BY

P. Stephen Glockner

A Thesis/Practicum submitted to the Faculty of Graduate Studies of The University of Manitoba in partial fulfillment of the requirement of the degree

OF

DOCTOR OF PHILOSOPHY

Abstract

This thesis investigates thermocapillary pumping (TCP) for cyclic displacement of discrete liquid droplets within closed-end microchannels. The droplets would act like pistons that expand and compress the surrounding gas chambers. This compression and expansion would flex piezoelectric membranes at the ends of the microchannels and generate electrical potentials across the membranes, from which electricity could be derived. The combination of several microchannels in parallel is the basis for a novel micro heat engine proposed in this thesis.

A prototype of a micro heat engine was manufactured with microchannels, fluid access holes, heaters and heater leads. Water droplets were imbibed into the corresponding microchanels without any external pumping. An experimental examination of thermocapillary pumping in polymer-based microchannels with a heater temperature of 35°C displaced a water droplet approximately 83μm. The droplet flowed in an irregular manner due to the relatively large surface roughness caused by the manufacturing procedure.

A new method of cyclic flow control with an external heat source was developed. Unlike past studies with a moving heat source at the receding edge of the droplet, this new technique involves a stationary cyclic heat source embedded within an adjoining silicon substrate. Thermocapillary pumping of the micro-droplet is examined numerically (finite volume method) and theoretically (slug-flow approximation).

The numerical formulation uses a new adaptive grid formulation with a sliding staggered grid in the micro-droplet, an expanding / contracting grid in the compressed gas section and an adaptive grid in the substrate section of the microchannel. Unlike past studies with a Poiseuille velocity profile, this thesis simulates re-circulation in the corners of the micro-droplet. These predictions entail fully coupled pressure / velocity fields at the droplet / air interface. Furthermore, in contrast to past studies with a uniform interfacial pressure, the numerical model accommodates a varying interfacial pressure along the receding edge of the micro-droplet. Temperature boundary conditions for a stationary heat source are applied at the interface between the substrate and its surroundings, rather than along the microchannel wall. The fluid momentum equations are solved with a staggered grid and adaptive mesh refinement at the liquid / gas interfaces. This refinement uses Bernstein polynomials and control points to adjust the grid spacing. Heat transfer across a thermal bridge within the substrate generates cyclic heating and cooling periods during the micro-droplet transport.

The theoretical model approximates the droplet as an undistorted slug within the microchannel. The capillary, friction and external forces acting on the slug are used in Newtons's Second Law of Motion to predict droplet acceleration. The velocity and position of the droplet are determined by numerical integration of the predicted acceleration. The temperature distribution is approximated by assuming that the domain is comprised of two adjoing semi-infinite solids during the heating period. A lumped capacitance model for the cooling period involves certain simplifying assumptions in the theoretical formulation. Close agreement between theoretical and predicted results of micro-droplet displacement provide useful validation of the formulations.

Acknowledgements

I would first like to thank my wife for all of her support while I worked on this thesis. Next, I would like to thank my advisor, Dr. G. F. Naterer, for his valuable consultations and support throughout this thesis. I would also like to thank my advisory committee, Dr. M. Tachie and Dr. R. Sri Ranjan, for valuable comments during meetings. I would also like to thank Dr. Shafai for his assistance in the Nanofabrication Lab and my colleagues and friends who helped keep my sane during the last three years. Support of this research from the Natural Sciences and Engineering Research Council of Canada, as well as a University of Manitoba Graduate Fellowship, is gratefully acknowledged.

Contents

List of Figures

List of Tables

Nomenclature

a	Empirical constant
b	Channel width, empirical constant, right-hand-side value
d	Channel height
G	Geometry-dependent constant
l, L	Characteristic length
$\dot{m}$	Mass flow rate
nx	Number of columns of real control-volumes
P_e	Peclet number
P	Pressure, control point
R	Gas constant
S	Source Term
t	Time, local coordinate
T	Temperature
u, v	Velocity components at control faces
U	Velocity component at node
V	Velocity component at node, volume
x, y	Coordinate directions

Leaf inserted to correct page numbering

Greek

α	Weighting coefficient, thermal diffusivity
β	Diffusion weighting coefficient
Γ	Diffusion coefficient
μ	Viscosity
ϕ	Scalar variable
ρ	Density
σ	Surface Tension

Subscripts

A, R	Advancing and receding ends of droplet
c	Capillary
e	External

Chapter 1

Introduction

Nanotechnology refers to the creation of functional materials, devices and systems through control of matter on the nanometer length scale (1-100 nanometers), and exploitation of novel phenomena and properties (physical, chemical, biological, mechanical and electrical) at that length scale. The fabrication of novel nano-devices is rapidly gaining worldwide attention due to its promising potential in various technological applications. For comparison, 10 nanometers is 1000 times smaller than the diameter of a human hair [1].

The great potential of ultra-small structures as a result of nanoscience opens a whole world of potential commercial applications. Experts at the US National Science Foundation have suggested that the value of the worldwide commercial market for nanotechnology-based products might reach $1 trillion or more between 2010 and 2015. Financial investors from around the world are optimistic that nanotechnology will become a significant contributor to the world economy. A report published by InfoShop estimates that the US nanotechnology R&D market will reach nearly $3.3

billion in 2007. The commercial markets could be a factor of 10× to 100× larger than the R&D market [2].

At present, however, nanotechnology is still relatively new. Today"s manufacturing methods are very crude at the molecular level. A Directions Magazine article written by Kevin Coleman states that "it is like trying to make things out of LEGO blocks with boxing gloves on your hands. Yes, you can push the LEGO blocks into great heaps and pile them up; but you cannot really snap them together the way you would like." [3]

Microtechnology, though dealing with devices and systems one thousand times larger than nanotechnology, has successfully offered an alternative to conventional technologies. To date, it has made great contributions to the areas of computer peripherals, sensors, bioscience systems and small actuators. Microelectromechanical Systems (MEMS) are the integration of mechanical components, electronics, sensors and actuators into a common device using microfabrication technology. Some examples of innovative micro-devices are accelerometers for automobile airbags, keyless entry systems, dense arrays of optical mirrors for high-definition optical displays and scanning electron microscope tips to visualize single atoms [4]. Micro heat exchangers have been developed for convective cooling of microelectronic circuits [5, 6]. The MEMS have also been applied in biomedical applications, such as microsystems for separating biological cells, blood analyzers and pressure transducers for catheters [7]. Other recent advances have utilized EBSM (Entropy Based Surface Micro-profiling) for purposes of flow control, drag reduction and entropy generation minimization [8]. Some other recent innovative examples include micro energy sources [9] and near-wall flow control [10]. These applications require effective control of microfluidic motion,

either with pressure driven forces [11] or electromagnetic forces [12].

Many of the aforementioned microtechnologies are merely components of macro systems, such as accelerometers for automobile airbags. These microtechnologies may be powered by the system into which they are being incorporated. It doesn't, however, make sense to manufacture standalone microdevices unless there are matching micro power sources. Thus, there is a great interest to develop micro power sources that have the same scale as the devices they will eventually power. It is the focus of this thesis to examine one embodiment of a micro-energy source, namely a micro heat engine.

1.1 Micro Power Sources

Universities and government labs, rather than industry, are largely dominating the micro engine field. The US National Nanotechnology Initiative is making it difficult for major companies to remobilize resources and dominate this field. Nanotech advancements require a multi-disciplinary approach, which is most economically achieved in a university setting. The National Nanotechnology Infrastructure Network (NNIN) has 13 university sites that form an integrated, nationwide system of user facilities to support research and education in nanoscale science, engineering and technology. The NNIN is for a five-year period investing at least $70 million for nanoscale science and engineering research. With this kind of funding for research and development, universities are less likely to seek industry support, thus explaining the reason why so much research and development is conducted outside of industry.

Engineering researchers in Oregon State University's Department of Electrical

and Computer Engineering have teamed up with researchers at Washington State University and the US Army Research Lab to develop a new micro-heat engine, dubbed the P3 [13]. An external heat source is used to increase the quality (fraction of mixture that is gaseous) and volume of a saturated mixture that is contained within a chamber. The expansion process flexes a piezoelectric membrane to generate a voltage. The quality and volume of the saturated mixture is then decreased through a cooling cycle. Repeated heating and cooling cycles are required to maintain engine operation. Three of the units (each of which is twice the thickness of a human hair and two millimeters square) can produce 40 micro-watts of electricity, which is enough to power a wristwatch using the body heat of the wearer.

Researchers at the University of California, Berkeley are developing two nano-engines [14]. The first focus is an internal combustion engine, a "mini engine" that could replace batteries as a power source for portable electronic devices. The engine is about the size of three stacked pennies. The engine uses liquid hydrocarbon fuels like butane, propane and gasoline to produce electrical and mechanical power for small-scale devices. The mini engine will run for about two hours on one fluid ounce of fuel. The second project focused on a smaller "micro engine" made from silicon components that could power MEMs. It is anticipated that the micro engine could run for about 67 days on one fluid ounce of fuel. The micro engine is expected to be powering devices within the next couple of years.

Researchers at Birmingham University have developed a micro engine that runs on lighter fluid, and it can generate 300 times more energy than a similarly sized battery [15]. The leader of the research team predicts that all portable devices that currently use batteries will derive their power from micro engines before 2010.

Researchers from the Alberta Research Council have developed a proprietary micro solid oxide fuel cell source of energy that could one day be used in small-scale portable applications such as laptops or personal digital assistants (PDAs) [16]. The group sees the development as an important milestone toward a strategic initiative in fuel cell technologies. The project began in mid 2001 and it involves both scientists and a commercial analyst. ARC had invested $700,000 into the project and it has filed five patent applications up to the end of 2002.

Researchers from the National Institute for Nanotechnology at the University of Alberta have made a device that directly converts water pressure to electricity [17]. The device gathers a small amount of electricity from the interaction between flowing water and the surfaces of millions of microscopic channels. The interaction at the boundary between the water and microchannels leaves the walls negatively charged, which in turn attracts positive hydrogen ions contained in the water. Water forced through a microchannel produces a streaming electric current by transporting the positively-charged ions in the direction of the water current. The researchers produced electrical currents of 1 to 2 millionths of an amp by flowing water through a glass filter containing millions of microscopic channels with a 30-centimeter hydrostatic pressure drop. The researchers were able to increase the electrical flow by increasing the salt concentration in the flowing solution. The device produced enough electricity to power a light-emitting diode.

In 2002, the University of Florida, University of California at Los Angeles and the University of Utah, began a five-year collaborative effort funded by a $5 million grant from the US Office of Naval Research to create a three-dimensional, millimeter sized battery [18]. The researchers have created nano-anodes and nano-cathodes that are

up to 100× more powerful than traditional electrodes. Current lithium ion battery electrode technology is able to sustain an average of 500 charges and discharges before wearing out. The group is anticipating that a prototype will be available in the next two years.

1.2 Micro-Pumping

Most of the micro power sources require a fluid to be transported within the microdevice and thus require that some type of pumping is incorporated into the device. Additionally, many MEMS that are not power sources require fluid transport. Microelectronic integrated circuits can be considered the "brains" of a system and MEMS augments this decision-making capability with "eyes" and "arms", to allow microsystems to sense and control the environment [19]. Most MEMS thus require some form of micropump to actuate these "arms", in order for the MEMS to interact with their environment and serve a useful purpose. Effective methods of microfluidic transport thus have significance in numerous emerging technologies of microscale engineering.

Microfluidic transport can be controlled by an applied pressure difference [11], electrical potential difference [12] or thermocapillary transport [20]. A comprehensive review of micro-pumping technologies was documented by Singhal et al. [21]. Limitations and advantages of about twenty different types of micro-pumps were described. The maximum flow rates of different micro-pumps were compared. Other comparisons involving actuation voltage, frequency of operation, cost of fabrication and electronics cooling capabilities were reported.

Various cross-sectional profiles of microchannels have been studied previously,

including circular profiles of microtubes [22], pressure-driven flow of water through trapezoidal microchannels [23], surface micro-grooves [10] and others.

1.2.1 Electro-osmotic Flow

Electrocapillary transport uses an electrical potential gradient between two immiscible conducting fluids to generate a spatial change of surface tension. This resulting fluid motion is called continuous electrowetting (CEW). Lee and Kim [24,25] have reported CEW control with a micro-droplet of liquid metal in circular microchannels. Using an applied voltage of 2.8 V and a micromotor, the authors have reported that liquid metal droplets can be transported along a microchannel loop in an electrolyte. Issues regarding the micromachining process, material compatibility, electrode polarization and electrolysis were documented by the authors.

Yun et al. fabricated a electrolyte-filled microchannel on a glass wafer in which surface-tension-induced motion of a mercury drop is used as actuation energy for a micropump [26]. The micro-pump operates under both low-voltage and low-power conditions. The moving droplet drags the electrolyte, thereby deflecting a membrane on a second adjoining silicon wafer. Inlet and outlet chambers on another silicon wafer are connected with a tube that completes the micro-pump loop. The configuration allows a maximum pump pressure of 800 Pa, with an applied voltage of 2.3 V at an operating frequency of 25 Hz and power consumption of 170 W.

1.2.2 Thermocapillary Pumping

There have been several numerical, analytical and experimental studies examining the thermocapillary properties of various fluids interacting with various solids and gases. Following is a brief summary of some of these studies.

Numerical Studies

Gurrum et al. [27] studied thermocapillary flow in a microchannel through a two-dimensional level set model. Values of surface tension were applied at both ends of the droplet and the level set results were compared with data obtained from a Poiseuille flow profile. The model predicted a lower average velocity, due to the departure of parallel flow in the proximity of the droplet ends.

A paper by Sammarco and Burns [28] outlined a thermal analysis of TCP within a microchannel. The analysis investigates both fluid flow and energy transport to develop materials, designs and operational guidelines for effective pumping performance. For pumping velocities less than 0.1 cm/s, it was shown that a uniform interface temperature is possible, when pumping water across a fused silica substrate with a glass microchannel.

Yoshida et al. [29] performed a two-dimensional numerical analysis of a micro-pump system driven by surface tension. Gas was trapped between thermoelectric elements interspersed within the channel. The surface force along the interface between the trapped gas and adjacent liquid drove the pump. The thermoelectric elements controlled the magnitude of the surface force. The authors varied certain design parameters of the micro-pump to determine effects of geometrical changes on system

performance.

When predicting convective transport in multiphase problems, past studies suggest that pressure weighted upwinding [30, 31], sub-grid quadrature refinement [32] or entropy residual reduction [33] can substantially improve the overall solution accuracy.

Analytical Studies

Riehl et al. [34] developed an analytical formulation of thermocapillary convection in a microchannel condenser. The researchers found that the capillary forces on the liquid methanol were affected by the meniscus shape. Results were presented at a Reynolds number of 6, for flow in channles with a hydraulic diameter of $D_h = 1.5$ mm and a mean velocity of $\bar{u} = 3$ mm/s. Relatively high values of the Nusselt number (approximately 150) were obtained due to the presence of a porous boundary. Additional results were presented for the vapor interface temperature, pressure and meniscus curvature. It was concluded that microchannel condensers with a porous boundary could be effectively used in applications involving high heat dissipation requirements within small enclosed areas.

Sen and Davis [35] have developed an analytical matched-expansion formulation of thermocapillary flow in 2-D slots. In their studies, the Reynolds number was 1.0 and the fluid Prandtl number was 0.2. Effects of heat conduction between the liquid and air phases were reported by the authors. Uniformly spaced temperature contours agreed well with predictions based on heat conduction alone in the theoretical analysis. Both heat conduction and convection affect thermocapillary transport. Heat transfer rates within irregular geometries can be predicted with shape factors [36].

Experimental Studies - Open Channels

Thermocapillary convection in a fluid layer with a horizontal free surface, subjected to a uniform applied heat flux, was reported by Hirt [37]. The velocity profile resembles that of a shear driven cavity flow, though a surface tension imbalance (as opposed to the driving wall in the shear driven cavity problem) drives the fluid rotation. No-slip conditions were applied along the wall below the layer and a specified pressure was applied at the right boundary of the domain. A non-uniform 10×21 grid was used in numerical simulations. The thermocapillary force was computed in terms of the applied temperature gradient at the boundary. The free surface remained nearly flat, so the normal surface tension forces (along the free surface) became negligible. Fluid motion is driven to the left, as the magnitude of thermocapillary forces is higher on the cooler left side. The author reported that comparisons against experimental data would be useful, but until such data is available, the predictions could only be compared against analytical solutions.

Thermocapillary forces have been used successfully for flow control along micro-patterned surfaces [38]. Surface micro-grooves can have useful benefits, in regards to reducing entropy production of convective heat transfer [8]. Thermocapillary mixing on micropattered surfaces was documented by Darhuber et al. [39]. The configurations have useful applications to mixing in chemical microreactors or gas sensors. Predictions were compared against confocal fluorescence microscopy measurements, in regards to interfacial diffusive broadening in adjacent flowing streams. The authors reported analogies between the mixing regimes, Rhines / Young shear-augmented diffusion and Taylor / Aris dispersion.

Thermocapillary heat transfer in a thin liquid film on a horizontal stretching sheet

was investigated with a similarity solution by Dandapat et al. [40]. A maximum local velocity occurred within the film, when the thermocapillary forces drag the film along the stretching sheet. As thermocapillary forces diminish, the boundary layer is confined to the lower part of the film.

Experimental Studies - Closed Channels

Thermocapillary forces may be used to control both vapour microbubbles and liquid microdroplets in closed-end microchannels. Ghiaasiaan and Chedester [41] have reported that thermocapillary forces suppress micro-bubbles forming in wall cavities of microchannels. They suggest that incipience in microchannels can be effectively controlled with thermocapillary forces. It is suggested that the onset of significant void in micro-tubes occurs with bubble departure from wall cavities, which may be controlled by thermocapillary forces on bubbles near the wall [42].

Thermocapillary transport can also be effectively used to create pressure gradients across a vapor bubble in a capillary [43]. The difference of surface tension across a bubble leads to multiphase convection towards the region of higher temperature. DeBar and Liepmann [44] have manufactured and tested silicon and quartz thermocapillary pumps with a square cross-sectional area. Three heaters were used, with one heater to generate a fluid-vapor interface and two other heaters to control the spatial temperature gradient. The pumps operated under a variety of conditions, in order to evaluate performance characteristics. In phase change problems with evaporating droplets, thermocapillary forces affect the critical wave number in the development of Marangoni instabilities [45]. During phase change, the boundary layer near the free surface of the droplet induces cellular motion due to Marangoni instabilities. Unlike

solid / liquid phase change [31,46,47], both diffusion and thermocapillary forces affect the spatial distortion of the evaporating droplet during phase change. Surface tension forces have significance in other multiphase systems, such as nucleate pool boiling [48] and three-phase problems [31].

Sammarco and Burns [49] have described how TCP can be used to pump small volumes of fluid within a micro-fabricated flow channel. TCP velocities up to 20 mm/min were measured for various liquids, with temperature differences ranging from 10°C to 70°C. Experiments yielded TCP velocities comparable to theoretical expressions derived for the TCP velocity [49].

An innovative TCP application involves optical fibres, when a small moving micro-droplet can re-direct a light beam by refraction or reflection to a different path [37]. Once the beam enters the fiber, it can be trapped by these internal reflections. Thermocapillary transport can be used as an optical "switch" to re-direct light from one fiber to another fiber. The droplet in the microchannel would intersect the fiber-optic light beam. When the micro-droplet moves to the position of the intersecting light beam, the beam is reflected to a different fiber. Recent FLOW-3D simulations [37] have studied thermocapillarity in a 14-micron channel (heated at the bottom boundary) for optical fiber applications. CFD studies [37] have predicted surface amplitudes of thermocapillary convection that are notably lesser than reported previously by Sasmal and Hochstein [50].

A miniaturized optical switch involving thermocapillary transport was presented by Togo et al. [51]. Temperature variations within the liquid produce a spatial change of surface tension, thereby driving microfluidic motion for purposes of pumping or switching.

Another recent innovation involving microfluidic thermocapillary transport is alignment of nano-wires suspended in an incompressible fluid for applications to electronic and photonic device assembly [52]. The technique involves thermocapillary motion of a droplet with suspended nano-wires in a microchannel. Parallel arrays are fabricated by nano-wires deposited on a patterned surface. The authors reported that the wetting liquid (hexadecane / octadecane solution with 1% mercaptoethanol) allowed the gold nano-wires to be produced with a typical diameter of 200 nm in an electrodeposition process. Thermocapillary heating of the microchannel was applied with a 5 W heater. Results indicated that thermocapillary transport of the micro-droplet allowed spatial control of geometrical orientation of the nano-wires.

TCP has potential bio-medical applications. Blood and urine samples are typically sent to labs for analysis of medical processes. With current technology, results from the sample may take several days. Additionally, errors such as mislabelling and lost samples may hamper with processing of data [7]. A lab-on-a-chip is a compact micro-device for point-of-care clinical testing, whereby all operations can be performed instantly on a small chip. Nanoliter samples of fluid can be transported within the chip to various processing stages using TCP. Since the fluid does not contact any physical pumping mechanism, the sample would not be contaminated. Unlike conventional micro-pumps, another advantage of TCP is it can move fluid in either direction, depending on the location of the surface heat source.

Past studies have also investigated thermocapillary pumping applications to flow control in microdevices. A plasma deposited surface coating was developed by Clements [53] to enhance the rate of thermocapillary pumping in microsystems. The surface coating was fabricated with a diode-pumped frequency tripled Nd:YAG laser. Ther-

mocapillary forces were successfully utilized to control flow rates in microchannels, in contrast to conventional pressure-driven or electro-osmotic methods.

1.3 Thermocapillary Pumping in a Micro Power Source

This thesis will develop a new micro power source that uses thermocapillary pumping (TCP) to drive a discrete microdroplet within a microchannel. The microdroplet would act like a piston that expands and compresses gas chambers. Non uniform heating of the droplet will generate temperature-dependent changes of fluid surface tension. It is driven by internal pressure differences resulting from surface tension variations at the ends of the discrete droplet, due to an applied temperature gradient.

Consider a droplet enclosed within a closed microchannel (see Figure 1.1). Heat is transferred through a thermal bridge across a substrate from a stationary cyclic source, which turns on / off to control thermocapillary transport of the enclosed micro-droplet. During heat input, thermocapillary forces induce fluid motion from left to right. Heat transfer to one end of the droplet leads to temperature variations within the liquid. Thermocapillary pumping arises when such variations, and differences between contact angles at both ends of the droplet, contribute to an effective pressure difference across the liquid. This difference induces fluid motion within the microchannel. When the droplet moves from left to right (see Figure1.1), the air pressure increases in the right section of the microchannel and decreases in the left section. During the cooling period when the heat source is turned off, these relative air pressures drives fluid back towards the initial equilibrium position of the droplet.

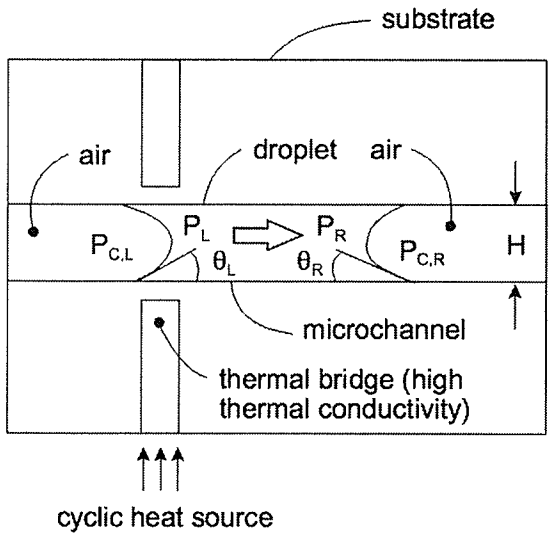

Figure 1.1: Schematic of Thermocapillary Pumping.

The cyclic heat source could be readily connected to several microchannels in parallel (see Figure 1.2). In this way, microfluidic transport within a larger network of microchannels could be effectively controlled by TCP.

Internal fluid motion within the droplet is governed by the Navier-Stokes equations, subject to appropriate boundary pressures at both ends of the droplet. An external pressure is generated when the droplet moves in the micochannel. In practical applications, this external pressure can be used when triggering a sensor, activating a switch or operating a flow control device in a microsystem. In Figure 1.1, the capillary pressure difference across the droplet can be expressed in the following way,

$$\Delta P_c = P_{c,R} - P_{c,L} = \left(\frac{G\sigma\cos\theta}{d}\right)_R - \left(\frac{G\sigma\cos\theta}{d}\right)_L \tag{1.1}$$

where $P_{c,L}$ is the capillary pressure on the left side of the droplet, $P_{c,R}$ is the capillary pressure on the right side of the droplet, θ is the contact angle between the liquid

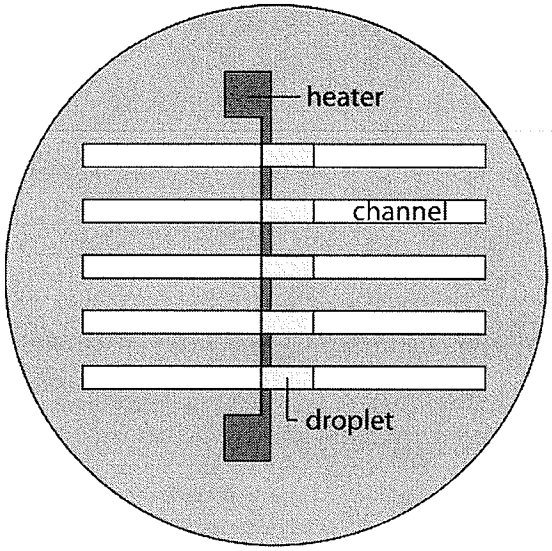

Figure 1.2: Multiple Microchannels Powered by a Shared Heat Source.

and solid wall and d is the channel height. Also, G is a constant (specific to the problem geometry). For example, $G = 4$ for a circular microtube, $G = 2$ for slit-like microchannels and for rectangular microchannels. In multiphase systems with droplets, the droplet is hydrophilic if the droplet is the wetting fluid, in which case $\theta < 90°$. On the other hand, the droplet is considered hydrophobic if the surrounding fluid is the wetting fluid, for which $\theta > 90°$. In Figure 1.1, θ is the contact angle and P represents pressure. The subscripts L and R refer to the left and right edges of the droplet, respectively. The contact angle is measured through the fluid of interest. If the contact angle is measured through the wetting fluid, it is always less than 90°.

During thermocapillary pumping, the advancing contact angle is generally larger than the receding contact angle. In this thesis, the receding and advancing contact angles were both assumed to be zero. For a contact angle of 10 degrees, the error of the predicted thermocapillary pressure (due to the assumption of a zero contact angle)

is about 1.5%. This deviation could be readily incorporated into the thermocapillary model, provided the contact angles were known. Such data in closed microchannels is unfortunately not available in the archival literature (to my knowledge). Different contact angles exist between the wall and liquid at both ends of the droplet in the physical problem. The numerical formulation will use orthogonal grids within the fluid regions. The meniscus is modeled as a flat surface that is perpendicular to the channel walls ($\theta = 90°$). This approach is a reasonable approximation, due to the small volume of the droplet ends, relative to the total volume of the droplet.

The surface tension along the receding meniscus of the droplet in Figure 1.1 decreases with increasing temperature. As a result, it decreases when the receding end of the droplet is heated, which lowers the capillary pressure and causes relaxation of the meniscus. The net decrease in capillary pressure is slightly offset by a corresponding increase associated with a smaller receding contact angle. In order to maintain a constant droplet volume, the advancing contact angle (θ_R) increases, thereby resulting in a decrease of interfacial capillary pressure and accompanying increase in P_R. The resulting pressure gradient within the droplet is reflected through a change in the shapes of the menisci at both receding and advancing edges of the droplet.

The initial result of heating the receding end of the droplet is a change of the droplet shape. Initial reluctance of the droplet to move when an end is heated is called surface tension hysteresis. There exists a point, however, at which the advancing end of the droplet will stop deforming. At this point, the internal pressure of the receding end of the droplet will be larger than the internal pressure of the advancing end of the droplet. This internal pressure gradient drives the microfluidic motion during thermocapillary pumping.

During the change of surface tension across the droplet, the resulting pressure difference induces bulk motion internally within the liquid. The change of surface tension at the heated meniscus with temperature, T, can be represented as follows [28],

$$\sigma = A - BT \tag{1.2}$$

where A and B are constants (i.e. $A = 75.83$ dyn/cm and $B = 0.1477$ dyn/cmK for water). A desirable feature of the working fluid is a high change of surface tension with temperature, which would generate the largest pressure difference for a given heat input. For example, water and d_2O_2 have high coefficients of B (most desirable). But surface tension must overcome friction within the droplet. When divided by dynamic viscosity, other fluids (such as toluene) become more effective as a working fluid. The working fluid should generate a high tension-induced pressure difference, in excess of a fixed frictional resistance within the liquid.

The influence of the coefficient B relative to the dynamic viscosity μ, may be characterized by the ratio of the thermocapillary force to the viscous drag force. This ratio may be written as

$$\frac{F_c}{F_f} = \frac{2B\Delta T\,(d+b)\,d}{12\mu u_b L b} = \frac{B\Delta T\,(d^2/b+d)}{6\mu u_b L} \tag{1.3}$$

where b is the channel depth and where the viscous drag force has been approximated based on the Poiseuille velocity profile for a given bulk velocity. For a given channel configuration and droplet velocity, the ratio differs only through B and μ. Table 1.3 compares this ratio for water, mineral oil and toluene. It can be seen that toluene is most suited to thermocapillary pumping, but water was chosen in this thesis because

Table 1.1: Influence of the Coefficients B and μ.

d	L	b	ΔT	u_b
2 μm	100 μm	100 μm	10 K	1 mm/s

	water	mineral oil	toluene
F_c/F_f	3.1416	0.1734	4.2106

of its safety and availability.

Chapter 2 will focus on the application of thermocapillary pumping to a micro heat engine. Possible configurations of the proposed heat engine will be discussed, alternative heat engines will be summarized and the manufacturing procedure of one embodiment of the proposed micro heat engine will be presented. Chapter 3 develops a theoretical model to analytically predict thermocapillary pumping in closed-end microchannels. The theoretical model is based on Newtons Second Law of motion. Chapter 4 develops a more detailed numerical method to fully simulate thermocapillary pumping in closed-end microchannels. A finite volume method is developed to discretize the domain and predict heat transfer and fluid motion in the microchannel. Chapter 5 presents the results of several simulations, including validation cases. Finally, chapter 6 will conclude the thesis and make recommendations for future research.

Chapter 2

New Type of Micro Heat Engine

Section 1.1 discussed the technological need for micro-heat engines to power microdevices. A heat engine is a device that converts heat energy into mechanical energy. Examples of heat engines include a steam engine, a diesel engine and a gasoline engine. All heat engines operate between a high-temperature source and a low-temperature sink, as shown in Figure 2.1. The high-temperature source may be solar radiation, combustion of fossil fuels (including waste heat) or nuclear fission. A part of the heat flowing from the heat source is converted to work, often using a turbine. The remaining heat is rejected to a low-temperature sink. The waste heat may be used to pressurize a different working fluid, which operates a different heat engine cycle. The above processes operate in cycles of heating and pressurizing a working fluid and rejecting waste heat to the low-temperature sink.

All of the work input to a system may be converted into heat. The opposite, however, is not true. All heat engines must expel some heat to a low-temperature sink, and the work output from a heat engine will always be less than the heat input

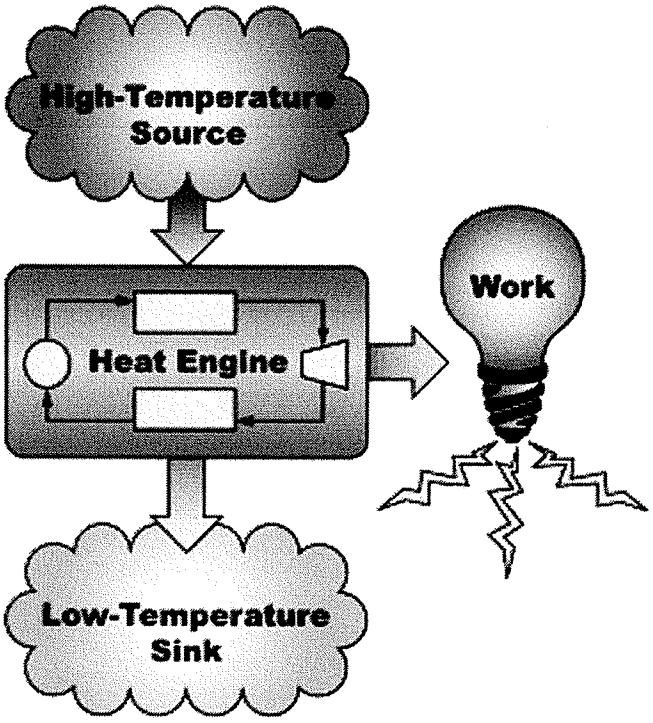

Figure 2.1: Conceptual View of a Heat Engine.

to the engine. The fraction of thermal energy that is converted into work is called the thermal efficiency of the heat engine. The maximum efficiency occurs for an ideal Carnot cycle. The thermal efficiency of the Carnot Cycle may be written as

$$\eta = \frac{T_H - T_L}{T_H} \tag{2.1}$$

where η is the thermal efficiency of the heat engine, T_H is the source temperature and T_L is the sink temperature, in Kelvin degrees.

A micro-heat engine operates on the same principles as a macro-heat engine, but it is smaller in scale. It is believed that micro-heat engines will have future capabilities to produce an equivalent specific work output as their macro-scale counterparts,

simply by scaling down all components of existing heat engines. However, the relative importance of various physical processes change at the micro-scale, due to the large surface area to volume ratio of micro-devices. Though some researchers are pursuing scaled down versions of macro-heat engines, it is novel micro-heat engines that are believed to have more promising potential as new alternatives to batteries and energy sources for MEMS. The next section presents a proposed embodiment of a micro heat engine, which has been developed in this Ph.D. project and recently patented.

2.1 Thermocapillary-Driven Micro Heat Engine

A front view of the new micro heat engine (μHE) is depicted in Figure 2.2. Several of these μHEs may be etched in parallel into a silicon wafer, as shown in Figure 1.2. It can be manufactured using standard batch processing technologies found in the micro-electronics industry. A water droplet is inserted into the center of each microchannel, so that one of its ends is aligned with a thermal bridge. The thermal bridges are metal tabs with high thermal conductivities and specific heats that effectively transfer heat from an external source to the receding edge of the droplet. Narrow air gaps adjacent to the thermal bridges reduce lateral heat transfer to the substrate. When the thermal bridge contacts the external heat source, heat is transferred locally to the receding edge of the microdroplet. Local heating raises the temperature at this end of the microdroplet. This is accompanied by a local decrease in surface tension and capillary pressure, as suggested by Eqs. (1.2) and (1.1). The difference between the capillary pressures at the ends of the droplet leads to a net pressure difference across the droplet and translation of the microdroplet in the direction of decreasing

temperature.

Each droplet is located between two gas chambers. The pressure of the gas chamber upstream of the microdroplet decreases as the chamber expands, causing upstream piezoelectric membranes at the ends of the microchannel to flex inward. The pressure of the gas chamber downstream of the microdroplet increases as the chamber compresses, causing the downstream piezoelectric membranes to flex outward. The flexing of the membranes creates electrical potentials across them. Electrical conditioning circuits connected to the membranes convert this electrical potential into an electrical current that may be used to charge a battery or power actuators. After the compression/expansion stroke, the heat source is removed. The temperature gradient across the microdroplet decreases, due to cooling by both convection to the surroundings and conduction through the μHE. This reduction in the temperature gradient across the microdroplet decreases the magnitude of the thermocapillary force. The positive external (gas) pressure difference forces the microdroplet back towards its starting position. The heat source is cycled to sustain cyclic microdroplet motion. This embodiment of a new micro heat engine will be called a THE (Thermocapillary Heat Engine).

One embodiment of the THE is shown in Figure 2.2. The microchannels are plasma etched into a 500 μm-thick silicon wafer to a depth of approximately 2 μm. The width and length of each microchannel are 100 μm and 2 mm, respectively. Three trenches are KOH etched into the backside of the substrate below each microchannel. These trenches permit fluid access holes to be bored into the bottoms of the microchannels and they reduce the thickness of the substrate in the vicinity of the thermal bridges. PZT piezoelectric membranes are deposited along the upper and

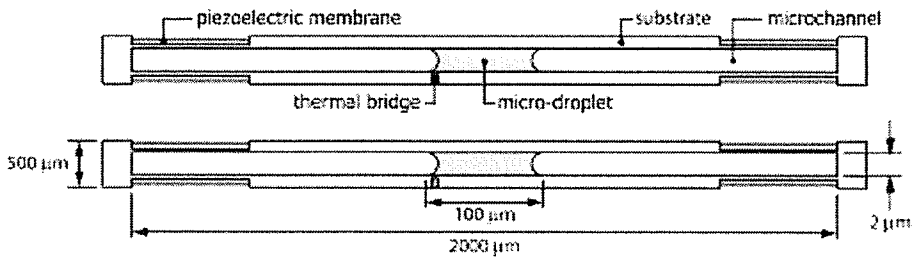

Figure 2.2: One Embodiment of a Thermocapillary Micro Heat Engine.

lower channel walls at each end of the microchannel, both upstream and downstream of the droplet. The substrate on which the membranes are deposited are thinned down to approximately 10 μm to allow flexure.

2.2 Manufacturing of THE

Various manufacturing steps were completed in order to determine the feasibility of the proposed design and realize limitations of the manufacturing techniques. Some concerns were whether a straight, 20 μm-deep fluid access hole could be plasma etched through the bottom of the microchannels, whether water could be drawn into the microchannel through these fill holes, how narrow the resistance heater can be deposited within the backside trenches of the wafer and what surface charactersists would exist in the microchannels.

The THE (without piezoelectric membranes) was manufactured with standard batch processing operations used in the microelectronics industry. The following procedure will be employed for manufacturing of the micro-heat engine. The designs feature a variety of channel widths and hole sizes and they affect the type of manufacturing procedures. After the manufacturing procedure and system parameters are

finalized, a micro-heat engine with piezoelectric membranes could be manufactured.

The first step starts with a 500 μm-thick silicon wafer with a 2 μm oxide layer on each side (Figure 2.9a).

Backside Trenches (Figures 2.9b-d):

1. spin photoresist on frontside to protect the surface
2. soft bake at 100°C for 1 minute
3. oven bake at 120°C for 10 minutes
4. spin photoresist on backside to become the trench mask for the oxide layer
5. soft bake at 110°C for 1 minute to cure photoresist
6. lithography on backside
7. develop photoresist
8. oven bake at 120°C for 10 minutes to cure photoresist
9. cover frontside with black tape to better protet surface
10. etch in 10:1 buffered oxide etch (BOE) for approximately 45 minutes to remove oxide layer, which becomes the mask for the Si etch
11. remove photoresist with acetone and blow dry with N_2
12. etch in KOH at 80°C for approximately 6.5 hours to form trenches, etch rate approximately 1 μm/minute, stop with approximately 22 μm left, oxide has been thinned to approximately 0.5 μm on backside

Frontside channels (Figures 2.9e-i):

1. thermal evaporation of aluminum of frontside to become channel mask
2. spin photoresist on aluminum to become aluminum mask
3. soft bake at 110°C for 1 minute
4. lithography on frontside

5. develop photoresist
6. oven bake at 120°C for 10 minutes
7. etch aluminum to reveal mask for channels
8. plasma etch frontside oxide 0.5 μm to expose the silicon surface
9. plasma etch silicon for frontside channels 2 μm deep
10. remove photoresist with acetone and blow dry with N_2 or remove resist with piranha etch
11. perform an aluminum etch to remove the aluminum mask

The mask used for a wafer containing both large and small microchannels can be seen in Figure 2.3. The dark areas shadow the photoresist during exposure and these unexposed regions are removed when the mask is developed. A prototpye silicon wafer with four large microchannels may be seen in Figure 2.4. The light horizontal stripes along the top and bottom of the wafer were caused by shadowing, due to fastening clamps that supported the wafer during thermal evaporation of the aluminum mask (to be used in plasma etching of channels). The shiny blue region encompasing the microchannels is a thin oxide layer that remained after plasma etching of the channels. The dull gray region around the perimeter is bare silicon, where the aluminum mask and oxide layer did not survive the plasma etching. A significant number of undesirable irregularities can be seen, which are a result of improper handling and surface contamination.

Frontside access holes (between channels and trenches) (Figures 2.9j-n):

1. deposit 0.5 μm Al to frontside using thermal evaporator to become mask for plasma etching access holes
2. deposit 0.1 μm Cr (to become heater leads) in vacuum system followed by 0.6

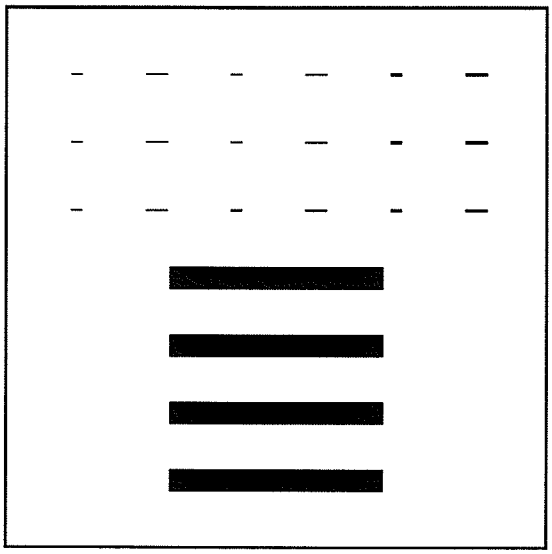

Figure 2.3: Mask for Forming Channels.

μm Al (to become heaters)

Cr Deposition

- one rod used
- voltage tap 5 V, 42%, 9.7 A
- deposition rate of approximately 1.5 Å/s
- vessel pressure of 3.5×10^{-7} Torr

Al Deposition

- 1.5 ft of wire used
- voltage tap 5 V, 37%, 22.2 A
- deposition rate of approximately 16.0 Å/s
- vessel pressure of 3.0×10^{-6} Torr

3. spin photoresist on backside to become mask for etching Al mask
4. soft bake at 110°C for 1 minute

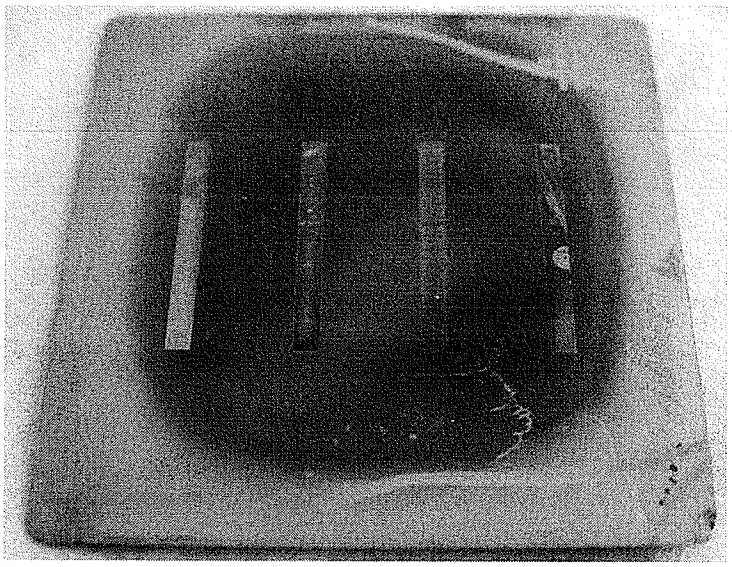

Figure 2.4: Silicon Wafer with Four 2mm×20mm×2μm Microchannels.

5. lithography on backside for Al heater leads
6. develop photoresist
7. oven bake at 120°C for 10 minutes to cure photoresist
8. etch aluminum (remaining aluminum becomes the mask for plasma etching)
9. remove photoresist with acetone
10. plasma etch holes until backside chrome is reached (approximately 20 μm)
11. etch aluminum to remove frontside mask

Photoresist was initially used as a mask for the holes during plasma etching. Plasma etching to a depth of 20 μm required approximately six minutes. The photoresist was not thick enough to survive this duration and no mask remained around the periphery of the silicon wafer. It was thus decided to implement the aluminum mask algorithm listed previously for subsequent plasma etching of access holes. A magnified image of an access hole (width 120 μm) may be seen in Figure 2.5. Figure

2.6 shows magnified views of an incompletely-etched fluid access hole. Figure 2.6a focuses on the top of the hole and Figure 2.6b focuses on the bottom of the hole. The top and bottom widths of the hole, as measured under an optical microscope, are 150 μm and 118 μm, respectively, with a hole depth of approximately 21 μm. This yields an etch angle of approximately 52.7°. Plasma etching was chosen for the microchannels because it yields an etch angle of approximately 90° for shallow features. The large depth and narrow width of the access holes clearly influenced the etch angle.

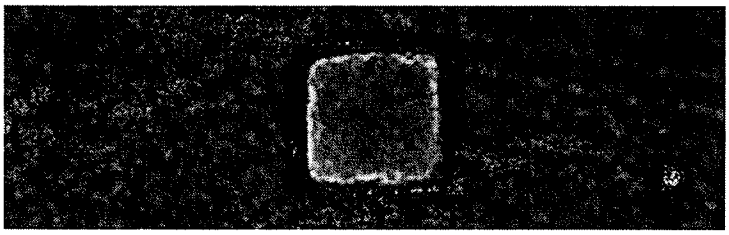

Figure 2.5: Magnified Frontside View of Fluid Access Hole.

The THE could receive heat from a waste heat source or solar radiation. During the micro heat engine design and testing phases, resistance heaters would provide a heat source. For this reason, heating strips were incorporated into the prototype design to determine manufacturing limits.

Backside heaters (Figures 2.9o-r):

1. spin photoresist on backside to become mask for heater leads
2. soft bake at 110°C for 1 minute
3. lithography on backside (for Al heater leads)
4. develop photoresist
5. oven bake at 120°C for 10 minutes
6. etch aluminum to create heater leads

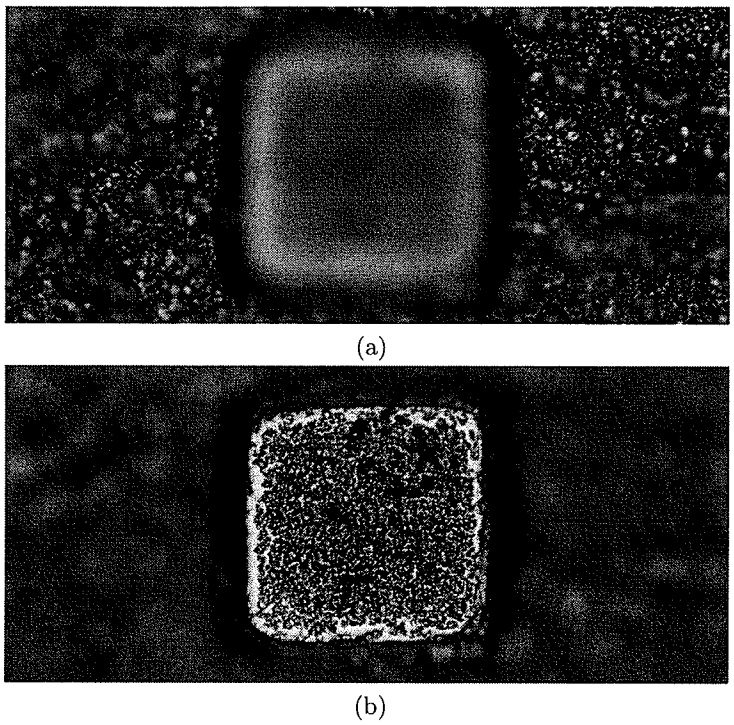

(a)

(b)

Figure 2.6: Magnified Front Side View of an Incompletely-Etched Fluid Access Hole; a) Top of Hole Focused, b) Bottom of Hole Focused.

7. remove photoresist with acetone
8. spin photoresist on backside to become mask for Cr heaters
9. soft bake at 110°C for 1 minute
10. lithography on backside (for Cr heaters)
11. develop photoresist
12. oven bake at 120°C for 10 minutes
13. etch chrome to form heaters
14. remove resist with acetone

The aluminum heater leads were successfully applied to the backside of the wafers. Figure 2.7 shows a portion of an aluminum heater lead on the backside of the wafer.

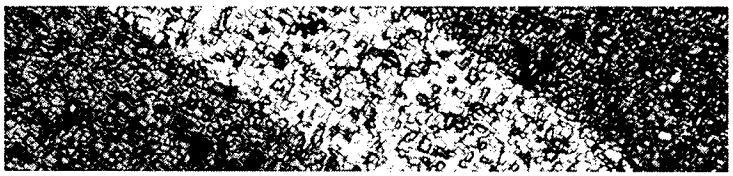

Figure 2.7: Aluminum Heater Lead on Backside of Wafer.

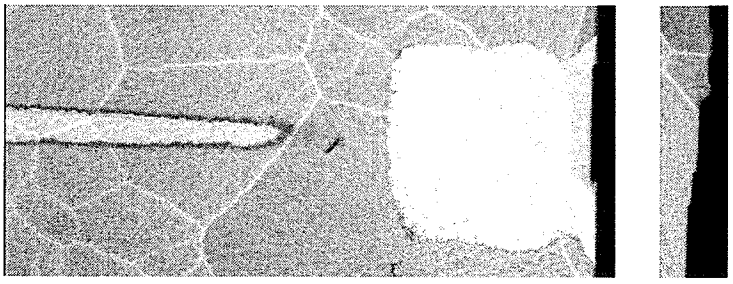

Figure 2.8: Unsuccessful Heater Showing a Discontinuity Due to Pooling Photoresist During Masking and a Poorly Masked Trench Edge.

The surface of the wafer appears very grainy, but the heater leads show no discontinuities anywhere, expect the bottom of the trenches. Figure 2.8 (left) shows a heater and heater lead at the edge of a trench. The pooling of photoresist in the bottom corners of the trench during spin coating resulted in poor application of the heater lead. The heaters showed discontinuities everywhere along the trench, indicating that the heater masks were too thin, thereby resulting in undercutting during etching. A thicker heater would ensure incomplete undercutting and guarantee unboken heaters. The right part of the Figure shows the trench wall, beside the heater lead. Both of the trench walls in the Figure are jagged. This indicates limitations in the printing procedure used for the masks. The printers that were used have a resolution of seven microns and they are printed on transparencies. A better printer is required for straighter walls.

When all of the appropriate dimensions have been established the following pro-

cedure would spin-coat the piezoelectric membrane onto the channel reservoir. The reservoirs are areas of the substrate that are thinned to permit flexure.

Bottom electrode:

1. create mask on silicon
2. deposit titanium (approximately 20 nm) onto silicon
3. vapor-deposit platinum (approximately 200 nm) onto titanium

Piezoelectric membrane:

1. spin-coat PZT (solution of Pb, Zr and Ti in proper stoichiometric ratio) onto reservoir
2. soft bake at 100°C for 5 minutes
3. soft bake at 350°C for 5 minutes
4. repeat until desired thickness is achieved (approximately 0.5 μm)
5. oven bake at 700°C for 15 minutes

Top electrode:

1. create mask on silicon
2. vapor-deposit gold (approximately 200 nm) onto piezoelectric membrane

A glass wafer, anodically bonded to the frontside silicon, forms the upper channel wall and it provides visual access into the channels for experimental analysis (Figure 2.9s). The droplets are drawn into the channels by capillary forces. It may prove useful to first fill the channel with CO_2 to aid imbibation. This may also aid in the formation of one continuous droplet, rather than several smaller droplets separated by air gaps. A variety of access hole sizes need to be tested to determine an appropriate size. If imbibation is not realized, it may be possible to insert water droplets manually before

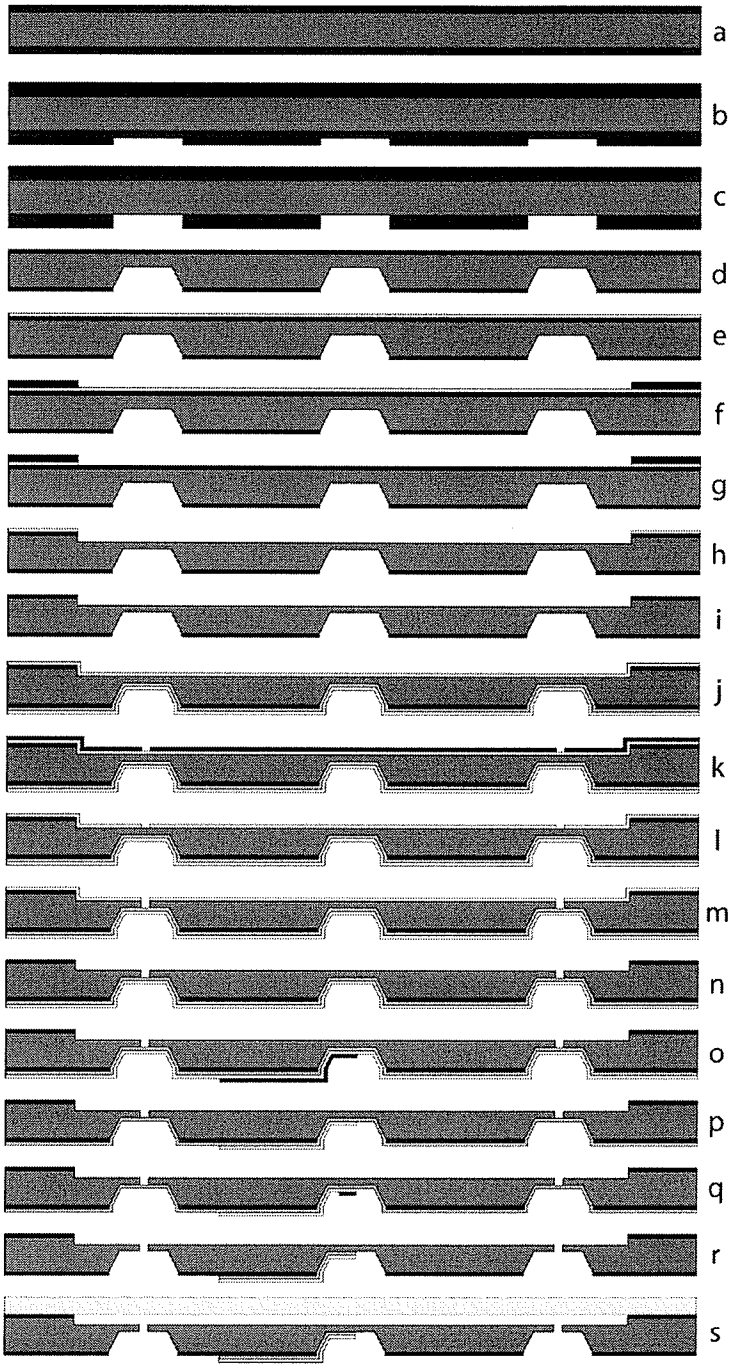

Figure 2.9: Manufacturing Procedure for One Embodiment of the Micro Heat Engine.

anodically bonding the glass substrate or mechanically pumping droplets through the access holes. The position of the droplets may be altered with external pressurization or thermocapillary pumping via an array of resistance heaters below the substrate. Positioning of the droplets has been accomplished previously by researchers studying thermocapillary pumping in open-ended microchannels. The access holes will need to be sealed after the microdroplets are injected into the microchannels. Wax may be an appropriate material because it dries quickly and it will not imbibe into the channel to a great extent.

The surface roughness of the silicon microchannels, which were manufactured in the Nanofabrication Laboratory at the University of Manitoba, was undetectable using the alpha step available in the laboratory. Figure 2.17 shows a magnified view of the microchannel surface, beside a fluid access hole (bottom right). The light objects dispersed throughout the Figure indicate incomplete etching. These objects range from a few microns to a few tens of microns and they are undetectable by the human eye or the image alignment equipment used during lithography. Particles between the silicon surface and the exposure light will shadow the photoresist during lithography. Particles on the silicon surface during plasma etching would also detrimentally affect the etch quality. Lithography, wet chemical etching and chemical vapour deposition were necessarily performed outside of the clean room, where there exists no particle control system. This lead to contamination of the wafer during manufacturing. The manufacturing of microdevices should be performed within a cleanroom environment. The Nanofabrication Laboratory at the University of Manitoba is currently being rennovated to conform with this requirement.

2.3 Configurations

The thermocapillary heat engine requires a cyclically displaced micro-droplet, with compressing and expanding gas chambers. The type of substrate, droplet fluid and gas chamber fluid may be chosen to best complement the operating environment. Two possible operating configurations are discussed below.

2.3.1 Cyclic Point Heat Source

Cycling of the heat source may be accomplished by bringing the heat source in and out of contact with the thermal bridge. Tabs underneath the substrate could be fabricated with a piezoelectric material. The uncharged state of the tabs would have the thermal bridge in contact with the heat source (heating stage). After the droplet has been sufficiently displaced, a small voltage would cause the tabs to flex (like a cantilever), or elongate to push the substrate away from the thermal bridge. When the external voltage is removed and the circuit is opened, the deflection would remain, thereby keeping the heat source out of contact with the thermal bridge. When the droplet has returned sufficiently, the circuit could be closed, thereby allowing the tabs to return to their uncharged state (un-flexed) and bring the thermal bridge back into contact with the heat source, to commence another heating cycle. Some of the energy stored in the tabs while flexed could be recovered to improve efficiency.

This concept could also work in reverse, where the uncharged state of the tab would have the thermal bridge out of contact with the heat source. By reversing the polarity of the voltage (compared to the above strategy), the tabs would contract when charged and bring the thermal bridge into contact with the heat source to

initiate the heating cycle.

The heat engine could also be activated by a heat sink, rather than a heat source. The thermal bridge would cool the advancing end of the droplet, rather than heating the receding end of the droplet. No changes would be required to the numerical formulation (Chapter 4) or the physical embodiment of the micro heat engine.

The operation of a thermocapillary-driven micro heat engine, with a cyclic point heat source is the major focus of this thesis. It will be discussed in Chapters 3-5. This configuration actively drives a compression stroke when the heat source is brought into contact with the engine, but it relies on passive heat dissipation to the surroundings, to return the system back to its equilibrium state before another compression stroke can be initiated. The cooling process is highly dependent on the nature of the surroundings. The next section discusses an alternative configuration that uses a reversing temperature gradient to actively drive a droplet back and forth within a microchannel.

2.3.2 Natural Convection Cell

The THE, like the P3 [13], requires cyclic heating and cooling cycles. Unlike the P3, which requires the working fluid to change phase from a gas to a liquid, the THE does not require a phase change (complete cooling) before the cycle can be repeated. Any temperature gradient across the droplet creates a pressure difference that can be used to displace the droplet. Rather than reducing the temperature difference across the microdroplet by removing the heat source to complete the cycle, the temperature gradient across the microdroplet may be reversed to initiate a pressurization stroke in the opposite direction. One method of reversing the temperature gradient would be

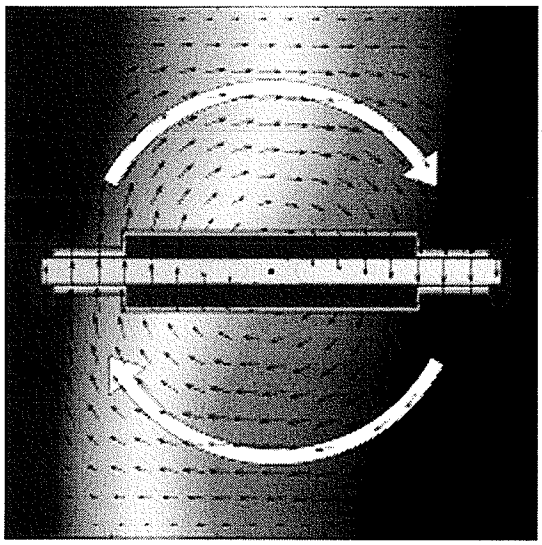

Figure 2.10: Natural Convection Cell to Provide a Cyclic Temperature Gradient Across the Microdroplet.

to place the micro heat engine in a natural convection cell, which would both rotate the engine and supply the temperature gradient (see Figure2.10). The cell could be built into any surface that has a temperature gradient across it, such as an exhaust pipe, engine block or computer case.

Natural convection of water was simulated for a Rayleigh number of $\mathrm{Ra} = 10^3$ in a square cavity with sides of 3 mm length. The following buoyancy term was included in the source terms of both the x- and y-momentum equations as follows

$$F_B = g\rho_{\mathrm{ref}}\beta\left(T - T_{\mathrm{ref}}\right)\cos\phi \tag{2.2}$$

where g is the acceleration due to gravity, β is the volumetric thermal expansion coefficient and ϕ is the angle of tilt of the cavity (assumed to be zero). The parameters for this simulation may be found in Table 2.1. The Rayleigh number is defined as

follows,

$$\mathrm{Ra} = \frac{\beta g L^3 \rho^2 c_p \Delta T}{\mu k} \tag{2.3}$$

where ΔT is the difference between the nodal temperature and the average of the specified hot and cold wall temperatures. Using the parameters in Table 2.1, a Rayleigh number of $\mathrm{Ra} = 10^3$ is obtained with a temperature difference of $\Delta T = 2.321°\mathrm{C}$. The resulting centerline u- and v-velocity fields are plotted in Figures 2.11 and 2.12, respectively.

An approximation for the time required for the micro heat engine to complete one revolution, and thus one compression cycle in each direction, was determined as follows. For each node along the horizontal and vertical midplane of the cavity, the circumerence of the circular path about the center of the cavity was determined. It was assumed that the fluid will travel along this circular path with its midplane speed. The time required to complete one revolution along the circular path was determined for each node. The average was determined from both u and v data. The resulting revolution times are $t_{R,u} = 6.819$ seconds and $t_{R,v} = 6.983$ seconds. Averaging these times yield a revolution time of approximately $t_R = 6.901$ seconds.

Without perfoming a simulation, the external pressure generated by the micro heat engine under the aformentioned conditions may be approximated. Consider that the duration of the compression stroke is equal to half of the time required for a rotation, $T_R/2 \approx 3.45$ seconds. This is larger than the compression time of approximately 0.00175 seconds, which is suggested by numerical simulations presented in chapter 5 (see Figure 5.29). It is thus reasonable to assume that the temperature field will be changing slowly enough that the droplet will have an approximately stationary equilibrium state when the temperature field begins to reverse, marking the end of

Table 2.1: Simulation Parameters for Natural Convection of Water in a Square Cavity.

Property	Value
Density (ρ)	998.0 kg/m^3
Dynamic Viscosity (μ)	959×10^{-6} Ns/m^2
Thermal Conductivity (k)	0.606 W/mK
Specific Heat (c_p)	4181.0 J/kgK
Volumetric Thermal Expansion Coefficient (β)	0.227×10^{-3} K^{-1}
Length of Cavity Wall (L)	3.0 mm
Number of x **control volumes** (nx)	20
Number of y **control volumes** (ny)	20

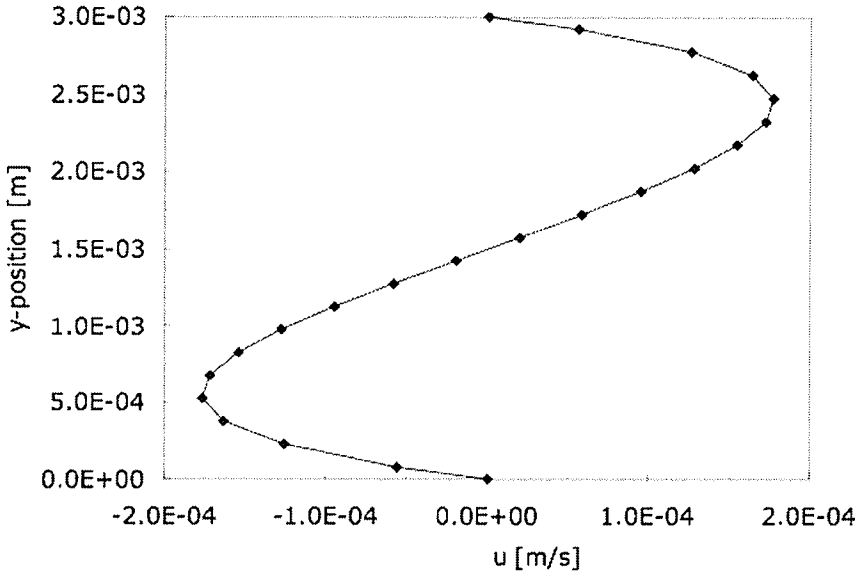

Figure 2.11: Midplane u-Velocity Profile Used to Determine Rotation Times.

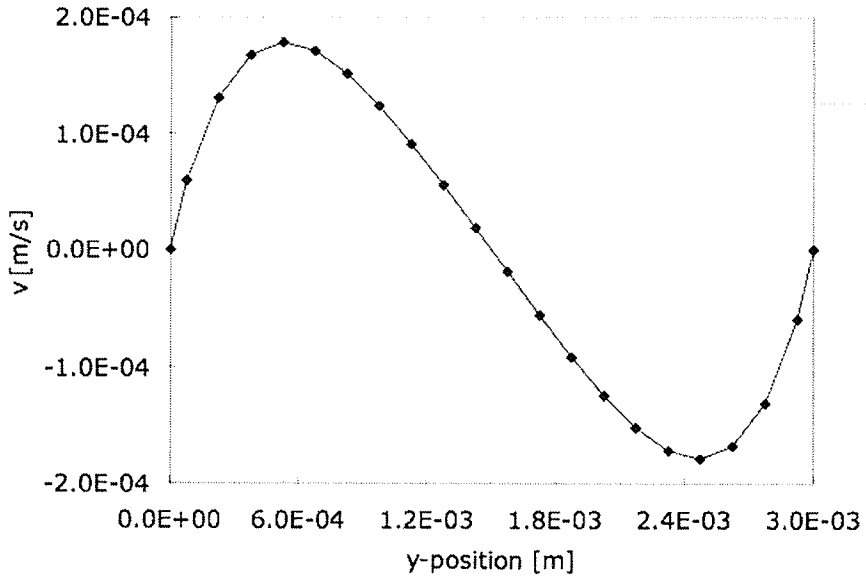

Figure 2.12: Midplane v-Velocity Profile Used to Determine Rotation Times.

the rightward compression stroke. In this case, the thermocapillary force will be balanced by the external air pressure. Combining Eqs. (1.2) and (1.1), we may write

$$\Delta P_c = \frac{GB\Delta T}{d} \tag{2.4}$$

This difference in capillary pressure is balanced by the external pressure difference across the droplet,

$$\Delta P_e = \frac{m_L R T_L}{(x_L + \Delta x)\, bd} - \frac{m_R R T_R}{(L_c - x_L - L_d - \Delta x)\, bd} \tag{2.5}$$

where x_L is the location of the left edge of the droplet (equal to the length of the left air chamber), m_L is the mass of air in the left gas chambers, m_R is the mass of air in the right gas chamber, Δx is the displacement of the droplet from its equilibrium position,

L_c is the channel length and L_d is the droplet length. Natural convection simulations show that a temperature difference of $\Delta T = 2.321°C$ between the hot and cold cavity walls corresponds to a temperature difference across the droplet of approximately $100\mu m/3000\mu m \times 2.321°C = 0.0737°C$. This is a very small temperature difference across the droplet. Thus, it would only produce a small difference in capillary pressure across the droplet. Thus, changes are needed to the natural convection cycle in a THE application.

Increasing the length of the droplet to nearly fill the microchannel would greatly increase the temperature difference across the droplet, given the same cavity boundary conditions. For example, the tempeature difference across a droplet of length 1500 μm would be approximately $1500\mu m/3000\mu m \times 2.321°C = 1.1605°C$. Thus, for the same cavity boundary conditions (and thus the same cycle time), the longer droplet would generate an external pressure difference that is approximately fifteen times larger than the difference generated by the shorter droplet. It can be shown that a temperature difference of $\Delta T = 1.1605°C$ across the droplet will displace the droplet by approximately 0.3093 microns and generate an external pressure difference across the doplet of approximately 241.78 Pa.

Another alternative is to increase the temperature difference across the cavity. This would effectively increase the temperature difference across the droplet, while increasing the Rayleigh number and decreasing the cycle time. Maintaining a droplet length of 1500 μm and increasing the tempeature difference across the cavity to 92.84°C would yield a natual convection cell with a Rayleigh number of 4×10^4. The temperature difference across the droplet becomes approximately $1500\mu m/3000\mu m \times 92.84°C = 46.42°C$. This temperature difference would displace the droplet by ap-

proximately 8.935 microns and it would generate an external pressure difference across the doplet of approximately 6.994 kPa. The cycle time for this configuration would be approximately 0.983 seconds. These calculations aim to show that various options and configurations exist for practical operation of the micro heat engine.

2.4 Experimental Investigation of Thermocapillary Pumping in Prefabricated Microchannels

An experimental study of thermocapillary pumping was performed using polymer-based microchannels manufactured by Epigem, which were part of a Fluence Microfluidic Tool Kit. A Fluence interconnection system was used, where a microfluidic baseboard provides the platform for the interconnection of multiple microfluidic chips. The distribution baseboard comprises an array of straight microchannels, with a corresponding array of mounting holes for aligning and accommodating the functional microfluidic chips. The baseboards are 6mm thick and they are provided with 100μm $\times$ 100μm microfluidic channels. The standard footprint for the microfluidic chips is 36 $\times$ 36mm. It comprises a square array of four fluid connection ports, each configurable as input, output, or no connection. In addition to the connection ports, each chip comprises 2 mounting holes to facilitate alignment and mounting to the tool kit distribution baseboard. The microfluidic chips are 4mm thick and they are provided with 100μm $\times$ 100μm microfluidic channels.

The experimental setup is shown in Figure 2.13. The objectives for the Leica DM RIM optical microscope are intended to focus on objects near the surface of the microscope"s X-Y table. The baseboard onto which the chips are affixed raises the

microchannels within the chips beyond the focal length of the objectives. As a result, the entire assembly was mounted upside down. This created interference between the fluid interconnects and the microscope objectives. A heating strip affixed to a 30 mm delay chip (illustrated in Figure 2.14) was chosen for experimentation because it provided the longest straight section of microchannel onto which the microcsope could focus.

(a) (b)

Figure 2.13: Experimental Setup for Thermocapillary Pumping in Open-End Epigem Microchannel.

The fluid was injected and positioned within the microchannel using a Kloehn V6 syringe drive module. This module is a stepping syringe drive unit that allows for very small fluid displacments. Smooth fluid motion was realizable within the flexible tubing connected to the board, as well as within the microchannels. Cheminert flangless tube end fittings (illustrated in Figure 2.15) connected the flexible tubing to the syringe pump and the baseboard. The droplets exiting these fittings pass completely through the chip, presumably due to pressure buildup within the fittings. A droplet was positioned within the chip only once, thereby allowing for little experimentation.

The receding edge of the droplet was positioned over the heating strip using the syringe drive module. A thermocouple, affixed between the microchannel and the heating strip, measured the temperature of the microchannel below the heating strip.

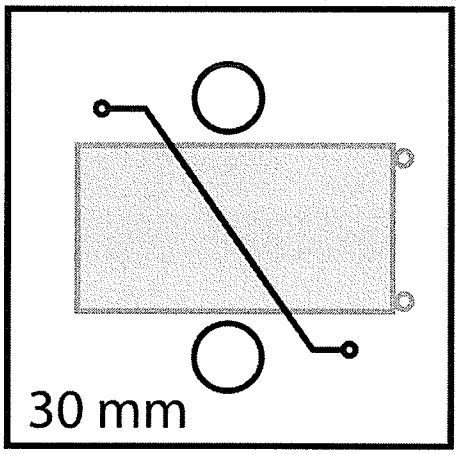

Figure 2.14: Illustrtaion of the 30mm Delay Chip with the Heating Tab Affixed.

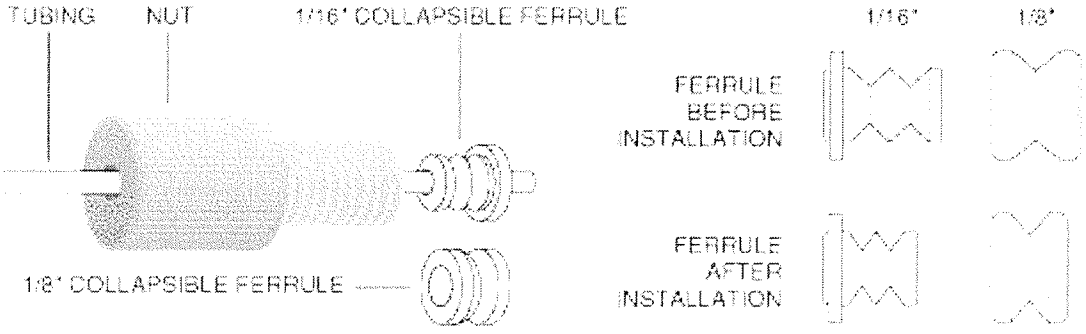

Figure 2.15: Illustration of Cheminert Flangless Tube Fittings.

The setpoint of the heater was set to 35°C, which was attained in approximately 5 seconds with no overshoot. A Kodak ES 1.0 CCD camera controlled by FlowManager Partical Image Velocimetry (PIV)) software was used to acquire images of the droplet motion through a Leica DM RIM optical microscope. An optical interconnect cable carried light from a Xenon lamp into the microscope. The initial and final positions of the droplet can be seen in Figure 2.16. A comparison of the two Figures indicates a droplet displacement of approximately 83μm. The displacement of the droplet in the images are compared against the channel width, which was known to be 100 μm. The images span 7 seconds, afer which time the dropet showed no further displacement. A rough approximation of the droplet velocity during this time is $83/7 = 11.86$ μm/s. The interface of the droplet in Figure 2.16a is not perpendicular to the channel walls. Also, the droplet was observed to flow in an irregular manner. The surface roughness caused by the manufacturing procedure influences the droplet motion. This may be insignificant for certain applications of the microfluidics tool kit, such as microchemical and microbiological applications. In these applications, the flow rate (reaction times) and mixing lengths are more important than the nature of the flow itself.

Examination of thermocapillary droplet motion within the open-ended Epigem microchannel demonstrated that large surface roughness leads to irregular droplet motion. Figure 2.17 shows a magnified view of the channel surface beside a fluid access hole. The larger, more lightly colored areas were virtually unetched, indicating contaminant on the surface of the wafer that acted like a mask during etching. The grainy region has a surface roughness that was undetectable with the alpha step in the Nanofabriaction Lab. This is an encouraging observation that indicates that the

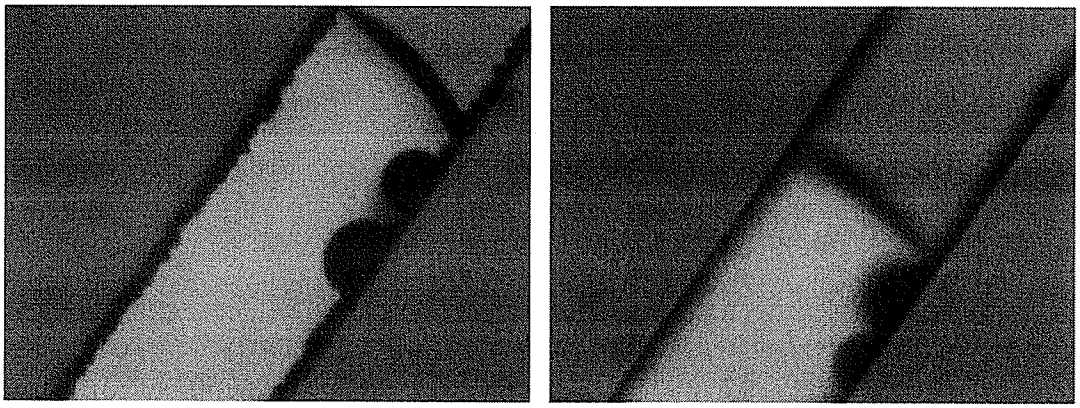

(a) (b)

Figure 2.16: Inital (a) and Final (b) Positions of a Water Droplet in a 100μm-wide Microchannel.

proposed manufacturing procedure will produce microchannels that are suitable for thermcapillary pumping.

This chapter has presented a novel thermocapillary-driven micro heat engine. A manufacturing procedure was proposed with standard batch processing procedures employed in the microeletronics industry. A majority of the manufacturing procedures were performed in the Nanofabriaction Lab at the University of Manitoba. Due to various limitations with the experimental facilities, such as microchannel surface roughness and micro PIV limitations, a full working micro heat engine prototype could not be fabricated. However, the experimental work in the chapter has made useful accomplishments towards this goal.

For example, backside trenches were successfully etched to reduce the thickness of the substrate around fluid access holes and heating strips. It was confirmed that fluid access holes could be plasma etched to a depth of 20 μm. Some of the holes were incompletely etched, even though the etching time should have been more than sufficient to penetrate to a depth of more than 20 μm. The walls of the holes sloped in

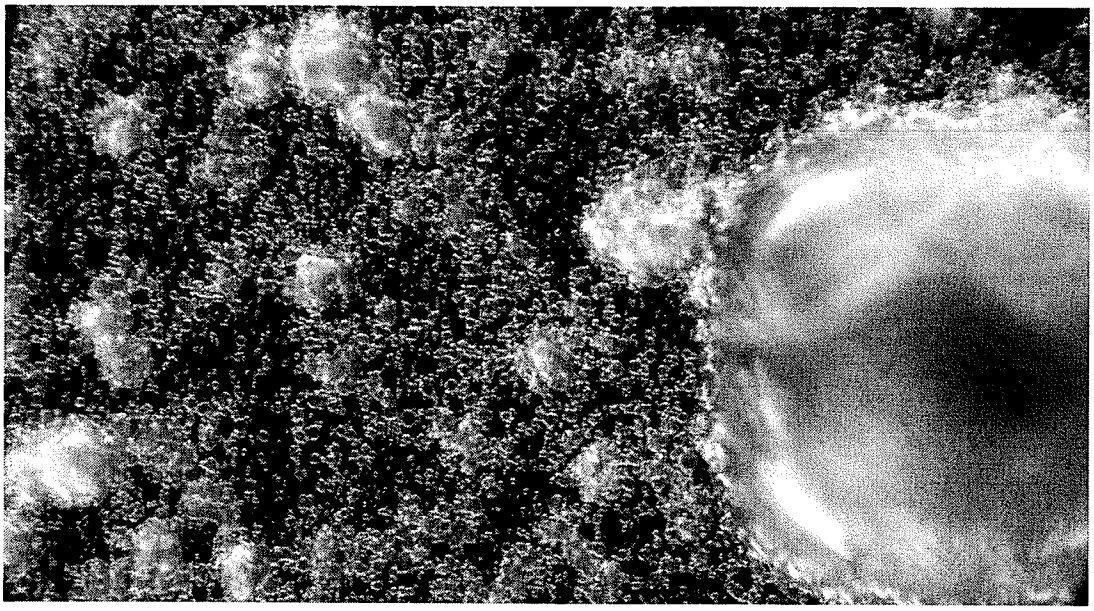

Figure 2.17: Magnified View of Microchannel Surface Adjacent to a Fluid Access Hole.

at an angle of approximately 57°C, rather than the expected 90°C. This suggests that a KOH etch could have been used instead. It was confirmed that water freely imbibes into the fluid access holes without requiring external pumping. The microchannels were successfully plasma etched to a depth of approximately two microns and they had a surface roughness that was undetectable by the available alpha step. Aluminum heater leads were successfully applied to the backside of the wafer. Pooling of photoresist in the corners of the trenches prevented any of the heaters from being successfuly applied to the bottom of the trenches. Slightly thicker heaters would alleviate this problem.

Chapters 3 and 4 will present a theroretical model and a numerical formulation for predicting thermocapillary pumping in closed-end microchannels, respectively. Such predications of droplet dynamics will aid in optimizing the performance of the micro

heat engines.

Chapter 3

Theoretical Model of Cyclic TCP

This chapter outlines a new theoretical model that was developed to quickly predict overall trends of cyclic thermocapillary pumping that was proposed to power the thermocapillary micro heat engine explained in the previous chapter. Consider heat transfer to a droplet within a closed microchannel (see Figure 2.2) from an external source, through a thermal bridge embedded in a substrate. A thin air gap between the thermal bridge and silicon substrate attempts to minimize lateral heat conduction, which would reduce the net heat input into the microchannel and the thermocapillary driving force on the moving droplet. At the substrate / droplet boundary, the heat input by conduction leads to convective heat exchange within the moving droplet.

Due to the complexity of this transient 2-D problem and the unknown conjugate boundary condition at the substrate / droplet interface, an analytical solution cannot be derived. Furthermore, the composite nature of the domain renders any general solution difficult. Each of the four phase regions (left air region, droplet, right air region and silicon substrate region) has different thermophysical properties. Addi-

tionally, heat transfer occurs within the liquid, solid and gas regions by coupled heat conduction and thermal convection. The thermal bridge transfers heat from the cyclic heat source to the droplet. Any theoretical predictions short of a full CFD solution would yield certain errors. However, a goal of the following theoretical model is predicting overall trends of the droplet motion, not the exact internal dynamics within a droplet. In this way, a simplified theoretical model can be used for global optimization studies. After certain global parameters are established, a detailed solution of the full NavierStokes equations can provide additional details regarding internal re-circulation within the moving micro-droplet.

3.1 Heating Period

In the following theoretical model, the droplet / air regions are approximated by two adjacent quasi one-dimensional semi-infinite domains. This approximation is supported by full numerical simulations, which indicate that convective cooling at the interface between the substrate and its surroundings is small compared to axial conduction across the domain. The dominant mode of heat transfer within the droplet may be examined with a scaling analysis of both conduction across and advection through the droplet. The convective heat transfer scales as

$$q_{conv} = udb\rho c_p \Delta T \tag{3.1}$$

while the conductive heat transfer scales as

$$q_{cond} = \frac{kdb\Delta T}{L} \tag{3.2}$$

where ΔT is a measure of the temperature difference above ambient conditions. The Peclet number (Pe) may thus be calculated as

$$\mathrm{Pe} = \frac{q_{conv}}{q_{cond}} = \frac{u\rho c_p L}{k} = \frac{uL}{\alpha} \tag{3.3}$$

Assuming a velocity of 1 mm/s, thermal diffusivity of 1.4523×10^{-7} m^2/K and a length of 100 μm, Pe has a value of 0.69. In practice, Pe would be much lower. A majority of heat transfer occurs in the vicinity of the heat source, so that the length scale over which conduction occurs is much smaller than L. Also, high temperature fluid is advected away from the heat source along the center third of the droplet ($d/3$), while low temperature fluid is returning along the outer two-thirds of the droplet adjacent to the channel walls. Radial heat conduction between these counter-flowing heat lanes reduces the thermal energy advected towards the advancing end of the droplet.

The heat source is assumed to span the entire height of the microchannel in Figure 2.2. In order to determine the magnitude of heat flow towards the left air / substrate region (left side of the heater) and droplet / substrate region (right side of the heater), it is assumed that each semi-infinite region has its own heat source at the shared interface. Then an interfacial condition is applied, whereby each region has the same interface temperature and the sum of heat flows from each region balances the total supplied heat flow from the heat source. The thermal bridge is not included in the theoretical model and it is not implemented in the numerical model, when comparisons between theoretical and numerical solution methods are made. Additionally, the heat source is changed in the numerical model to match the source in the theoretical model.

Under these assumptions, the heater becomes aligned with the left receding edge of the droplet. The interface temperature of either semi-infinite region, subject to a constant interfacial (surface) heat flux, q''_s, becomes

$$T(0,t) = T_i + \frac{2q''_s(\alpha t/\pi)^{1/2}}{k} \tag{3.4}$$

which may be written for the left and right sides of the heater as follows,

$$T_L(0,t) = T_i + \frac{2q''_{s,L}(\alpha_L t/\pi)^{1/2}}{k_L} \tag{3.5}$$

and

$$T_R(0,t) = T_i + \frac{2q''_{s,R}(\alpha_R t/\pi)^{1/2}}{k_R} \tag{3.6}$$

Equating temperatures in Eqs. (3.5) - (3.6) at the interface ($x = 0$) and re-arranging,

$$q''_{s,L}\frac{(\alpha_L)^{1/2}}{k_l} = q''_{s,R}\frac{(\alpha_R)^{1/2}}{k_R} \tag{3.7}$$

The total supplied heat flux from the thermal bridge matches the sum of heat flows from each region, so

$$q''_{s,R} = q''_s - q''_{s,L} \tag{3.8}$$

Using this heat balance in Eq. (3.7) yields the following result,

$$q''_{s,L} = \frac{q''_s\dfrac{(\alpha_R)^{1/2}}{k_R}}{\dfrac{(\alpha_L)^{1/2}}{k_L} + \dfrac{(\alpha_R)^{1/2}}{k_R}} \tag{3.9}$$

After the value of $q''_{s,L}$ is determined, then the value of $q''_{s,R}$ can be solved with Eq.

(3.8). This procedure allows heat conduction within the domain to be modeled as two separate problems, with matching temperatures at the interface between both regions.

In the previous analysis, the values of α_L and α_R are properties of the composite material. The thermal conductivity of the left semi-infinite solid is approximated as

$$k_L = k_a \left(\frac{d_a}{d_t}\right) + k_s \left(\frac{d_s}{d_t}\right) \tag{3.10}$$

Similarly, the conductivity of the right semi-infinite solid is written as

$$k_R = k_d \left(\frac{d_d}{d_t}\right) + k_s \left(\frac{d_s}{d_t}\right) \tag{3.11}$$

where d refers to height. The subscripts a, d, s and t refer to air, droplet, substrate and total, respectively.

Then, the thermal diffusivity of the left semi-infinite domain can be estimated as

$$\alpha_L = \frac{k_L}{\rho_a c_{p,a} d_a/d_t + \rho_s c_{p,s} d_s/d_t} \tag{3.12}$$

Similarly, for the right semi-infinite region,

$$\alpha_R = \frac{k_R}{\rho_d c_{p,d} d_d/d_t + \rho_s c_{p,s} d_s/d_t} \tag{3.13}$$

In order to validate this assumption, thermocapillary pumping problems in chapter 5 will be analyzed with both numerical (FVM; finite volume method) and theoretical methods. This section has considered the heating period when the droplet would

be aligned above the thermal bridge. After it passes beyond the thermal bridge, a cooling period is encountered (next section).

3.2 Cooling Period

The second stage of droplet motion occurs during the cooling period, after the receding edge of the droplet moves past the thermal bridge in Figure 2.2. During the cooling period, a lumped capacitance approximation (called an LC Model) will be adopted, as a semi-infinite assumption is no longer adequate. A non-uniform initial temperature distribution and unknown transient surface temperature and heat flux make a semi-infinite assumption unrealistic. The LC approximation neglects spatial temperature variations within the droplet, but it predicts temporal changes of the receding edge temperature over time. This assumption is considered reasonable, in view of the tiny thermal mass of the micro-droplet. Though the dominant mode of heat transfer is axial conduction through the channel, the lumped capacitance considers convective cooling at the interface between the substrate and its surroundings. The portion of the domain considered in the LC Model is about 100 microns (length of the droplet) on either side of the heat source. Numerical simulations with the finite volume method confirmed that temperatures changed little outside of this range.

Based on the lumped capacitance assumption for cooling of the droplet [31],

$$T = T_o + (T_i - T_o) \exp\left[-\frac{hA_s t}{\rho V c_p}\right] \tag{3.14}$$

Alternatively,

$$t = \frac{\rho V c_p}{h A_s} \ln\left(\frac{T_i - T_o}{T - T_o}\right) \tag{3.15}$$

where T_i is the initial temperature in the cooling period. Also, A_s is the surface area exposed to the surroundings having a heat transfer coefficient of h and a temperature of T_o. The value of h was approximated from the heating temperature profile of Eq. (3.4). The heating profile was considered in reverse, as a cooling curve from the point (T_c, t_c) to $(T_i, 0)$, where the subscript c refers to a critical point when the droplet has been displaced by a specified amount.

For example, (T_5, t_5) corresponds to conditions when the droplet is displaced by 5 μm. In this case, the approximation of the heat transfer coefficient during the cooling period becomes

$$h = \frac{\rho c_p V}{t_5 A_5} \ln\left(T_5 - T_0\right) \tag{3.16}$$

where

$$\rho c_p = \frac{\rho c_{p,a} d_a + \rho c_{p,d} d_d + 2\rho c_{p,s} d_s}{2 d_t} \tag{3.17}$$

The previous analysis provides an approximation of the droplet temperature during the cooling period. Heating of the droplet is controlled by an external heat source, while cooling of the droplet depends of the nature of the surroundings (substrate and adjacent air regions). Though the system state at the end of the heating period has major importance, a better approximation of the cooling period is needed.

3.3 Microfluidic Forces of TCP

Figure 2.2 illustrates the region of interest for thermocapillary pumping (TCP) of a discrete droplet enclosed within a rectangular microchannel. Heat transfer to the left end of the droplet generates temperature variations within the liquid. The surface tension at an edge of the droplet varies with temperature, T, in the following manner,

$$\sigma = A - BT \tag{3.18}$$

where $A = 75.83$ dyn/cm and $B = 0.1477$ dyn/cmK for water. A large change of surface tension with temperature is desirable, as it would generate the largest pressure difference for a given heat input. This suggests that B in Eq. (3.18) is the most significant coefficient. Considering that surface tension must overcome friction within the channel, a working fluid with a high B/μ ratio is also desirable. This thesis utilizes water as a working fluid, as water ($B/\mu = 15.5$ cm/sK) is more effective than other fluids (such as mineral oil, $B/\mu = 0.85$ cm/sK, or H_2O_2, $B/\mu = 12.4$ cm/sK) as a thermocapillary working fluid.

In the following theoretical model, consider an approximation whereby the micro-droplet is treated as a non-deformable slug transported through the closed microchannel. A heat source located at the receding edge of the micro-droplet generates a thermocapillary force and fluid motion occurs from left to right in Figure 2.2. During this droplet transport, the enclosed air section on the right side is compressed and the air on the left side is expanded. As a result, the rightward acceleration of the droplet is reduced, relative to a corresponding case for droplet motion in an open-ended channel. Frictional resistance also reduces the rightward acceleration of the

droplet. Based on the resulting net force (F), the droplet velocity (u) and displacement (x) can be determined from temporal integration over a discrete time step, Δt, of Newtons Second Law as follows,

$$u = u^o + \frac{F\Delta t}{m} \tag{3.19}$$

$$x = x^o + u\Delta t \tag{3.20}$$

where m and the subscript o refer to the droplet mass and previous time step, respectively. This approach will be called an SA Model (slug-flow approximation), as slug-like motion is predicted without internal distortion of the droplet. This simplified model will be compared afterwards to full numerical simulations of the Navier-Stokes equations within the droplet, in order to confirm the models reliability.

The net force on the droplet consists of a sum of three components, namely: (i) a thermocapillary force (F_c), (ii) external air forces (F_a) and (iii) a frictional drag force (F_f). These forces will be predicted in the following sub-sections.

3.3.1 Thermocapillary Force (F_c)

The thermocapillary force is a transient force acting on the slug, which arises from a temperature difference and resulting surface tension difference across the slug. Axial heat conduction is assumed as the dominant mode of heat transfer across the droplet. It is several orders of magnitude larger than convective exchange with the surrounding substrate. The droplet length is much larger than its height, so heat conduction in a semi-infinite domain was approximated during the heating period (see section 3.1).

Using temperatures calculated from Eq. (3.4), the variation of surface tension

with temperature can be predicted. Then, the resulting thermocapillary force due to the pressure difference across the droplet becomes

$$F_c = \Delta P_c A = (P_{c,R} - P_{c,L})\, A = GA \left[\left(\frac{\sigma cos\theta}{d} \right)_R - \left(\frac{\sigma cos\theta}{d} \right)_L \right] \tag{3.21}$$

where $P_{c,L}$ and $P_{,cR}$ are capillary pressures on the left and right edges of the droplet, respectively. Also, θ is the contact angle between the liquid and solid wall (assumed to be zero) and d is the channel height. The value of G depends on the specific problem geometry. For example, $G = 4$ for a circular microtube, while $G = 2$ for slit-like microchannels and $G = 2(1 + \text{height/width})$ for square and rectangular microchannels.

3.3.2 External Air Force (F_a)

An external air force on the micro-droplet occurs from compression / expansion of the gas downstream / upstream of the droplet, respectively. For example, during droplet translation from left to right in Figure 2.2, the compressed air exerts resistance on droplet motion. The air was approximated as a perfect gas according to the ideal gas law,

$$PV = mRT \tag{3.22}$$

where $R = 287$ J/kgK. The mass within each air region was calculated based on specified initial conditions, while the volume of each air region was determined from the droplet translation.

3.3.3 Frictional Force (F_f)

The frictional force imposed on the slug by the channel walls was estimated from the steady-state velocity profile for Poiseuille flow, i.e.,

$$u = -\frac{d^2}{2\mu}\frac{\partial P}{\partial x}\left[\left(\frac{y}{d}\right)^2 - \frac{y}{d}\right] \tag{3.23}$$

where y is measured from the microchannel wall. The bulk velocity, u_b, may be determined from Eq. (3.23). It becomes 2/3 of the centerline velocity, so

$$u_b = -\frac{d^2}{12\mu}\frac{\partial P}{\partial x} \tag{3.24}$$

A steady-state flow field is generated by a constant pressure gradient, so the pressure gradient, $\partial P/\partial x$, is assumed to have a constant value for a given time step. Then the wall shear stress on the slug can be approximated from Eqs. (3.23) - (3.24), after differentiating the velocity profile and multiplying the resulting wall shear stress by the surface area of the wall / droplet interface, $2\Delta x b$, thereby yielding

$$F_f = \frac{12}{d}\mu\Delta x b u_b \tag{3.25}$$

where b is the channel width. This force resists thermocapillary motion of the microdroplet from left to right in Figure 2.2. A force balance at steady state reveals that the frictional resistance is balanced by the driving force caused by the external pressure difference across the microdroplet, so

$$\frac{12}{d}\mu\Delta x b u_b = A\Delta P \tag{3.26}$$

Combining the previous thermocapillary, air and friction forces gives the following net force on the micro-droplet,

$$F = GA\left[\left(\frac{\sigma cos\theta}{d}\right)_R - \left(\frac{\sigma cos\theta}{d}\right)_L\right] + AR\left[\left(\frac{m_a T_a}{V_a}\right)_L - \left(\frac{m_a T_a}{V_a}\right)_R\right] + A\Delta P \quad (3.27)$$

This net force will be used to determine the droplet velocity and displacement in Eqs. (3.19) and (3.20). During the cooling period, the air force (second term on right side) assists the droplet motion, rather than resisting its motion. The theoretical formulation presented in this chapter is called the SA Model (slug-flow approximation). In the next chapter, detailed CFD simulations of the full Navier-Stokes equations within the droplet are developed for comparison purposes and validation of this theoretical formulation.

Chapter 4

Numerical Formulation of TCP

In addition to the theoretical formulation presented in chapter 3, a numerical method was developed to predict thermocapillary pumping in closed-end microchannels. The formulation uses a finite volume method (FVM) to discretize the governing equations. Unlike the theoretical model, the numerical formulation solves the internal flow within the accelerating droplet and the heat transfer throughout the entire domain, with temperature boundary conditions applied only along the outer boundary of the domain. The numerical formulation also incorporates a thermal bridge. The thermal bridge is a laterally insulated strip of highly-conductive metal that directs heat from the heat source towards one edge of the droplet.

This chapter begins by presenting the rationale for the chosen domain discretization method. The governing equations are presented, followed by a description of the meshing scheme. Difficulties with enforcing internal boundary conditions, along with the proposed solution, are discussed next. New pressure and velocity boundary conditions are presented for the new meshing scheme. Finally, a formulation is

proposed to predict heat transfer in the vicinity of the thermal bridge, where steep temperature gradients exist and compositions of the composite control volumes are rapidly changing.

4.1 Discretization of the Domain

The formulation for solving TCP in closed-end microchannels began as an FVM-based computational fluid dynamics (CFD) code for solving general two-dimensional fluid flow and heat transfer problems on uniform meshes. All of the boundary conditions were applied to fictitious control volumes along the boundaries of the droplet. The boundary conditions for the heat source were applied directly to the receding end of the droplet, similarly as performed by previous authors. Unfortunately, the temperature boundary condition is generally unknown in the physical embodiment of the micro heat engine in chapter 2. Additionally, the temperature boundary conditions would be applied to the bottom of the microchannel substrate (silicon wafer into which the microchannels are etched). As a result, the model was revised to include the substrate and air chambers that surround the droplet.

The fluid flow portion of the numerical model was left intact, including the mesh for the momentum equations. The droplet flow is still solved in the reference plane of the microchannel. No-slip velocity boundary conditions are applied along the microchannel walls and the velocity field resembles Poiseuille flow, as shown in Figure 4.1a. After each time step, the momentum equation mesh is translated, so it remains aligned with the droplet. When viewed in the droplet reference frame, a recirculating flow is observed (see Figure 4.1b). Recall that thermocapillary flows are driven by

a surface tension imbalance across the droplet, which is induced by a temperature difference across the droplet. The boundary conditions for the droplet flow thus require an accurate prediction of the temperatures at each end of the droplet.

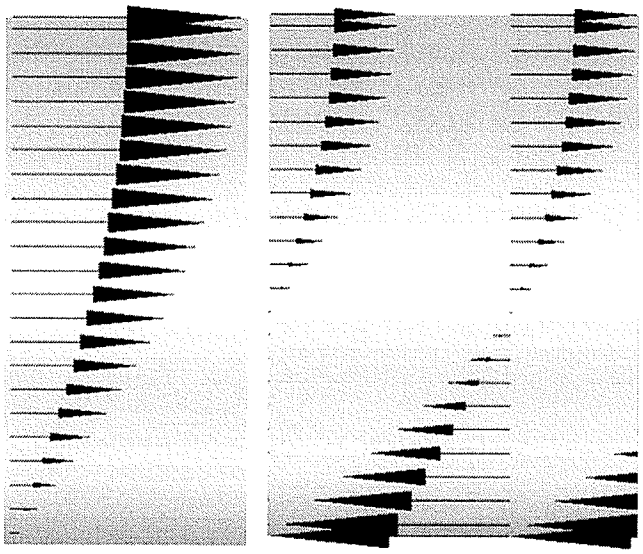

Figure 4.1: Velocity Profile for the Bottom Half of the Symmetric Domain in a) the Reference Frame of the Microchannel, b) the Reference Plane of the Droplet.

A separate temperature equation mesh was generated, whereby temperature fields for all four phase regions are predicted. The momentum equation mesh overlaps the droplet portion of the temperature mesh. The pressure nodal points from the momentum equation mesh have the same locations as the nodal points from the temperature mesh. The mesh within the substrate is horizontally aligned with the three adjacent meshes. When the droplet moves within the microchannel (and thus within the temperature domain), the temperature equation mesh is regenerated. The droplet portion of the mesh translates, so it remains beneath the momentum equation mesh, but it remains undistorted. The mesh of the upstream air chamber is stretched to accom-

modate the droplet translation, while the downstream air chamber is compressed. The substrate mesh is distorted to maintain alignment with the control volumes of the fluid phases.

The fluid flow equations for the droplet are solved on the momentum equation mesh, while the energy equation is solved on the temperature equation mesh. The velocity field from the momentum equation mesh is used when calculating the advection terms for the droplet portion of the energy equation. The following section explains how the governing equations are discretized using a finite volume method.

4.2 Discretization of the Governing Equations

The following two-dimensional conservation equations for mass, momentum and energy are solved when simulating thermocapillary pumping in closed-end microchannels.

$$\frac{\partial}{\partial t}(\rho) + \frac{\partial}{\partial x}(\rho u) + \frac{\partial}{\partial y}(\rho v) = 0 \tag{4.1}$$

$$\frac{\partial}{\partial t}(\rho u) + \frac{\partial}{\partial x}(\rho u u) + \frac{\partial}{\partial y}(\rho v u) = -\frac{\partial p}{\partial x} + \frac{\partial}{\partial x}\left(\mu\frac{\partial u}{\partial x}\right) + \frac{\partial}{\partial y}\left(\mu\frac{\partial u}{\partial y}\right) + \dot{S}_u''' \tag{4.2}$$

$$\frac{\partial}{\partial t}(\rho v) + \frac{\partial}{\partial x}(\rho u v) + \frac{\partial}{\partial y}(\rho v v) = -\frac{\partial p}{\partial y} + \frac{\partial}{\partial x}\left(\mu\frac{\partial v}{\partial x}\right) + \frac{\partial}{\partial y}\left(\mu\frac{\partial v}{\partial y}\right) + \dot{S}_v''' \tag{4.3}$$

$$\frac{\partial}{\partial t}(\rho c_p T) + \frac{\partial}{\partial x}(\rho u c_p T) + \frac{\partial}{\partial y}(\rho v c_p T) = \frac{\partial}{\partial x}\left(k\frac{\partial T}{\partial x}\right) + \frac{\partial}{\partial y}\left(k\frac{\partial T}{\partial y}\right) + \dot{S}_T''' \tag{4.4}$$

The SIMPLEC procedure [54] with a staggered grid was used to solve the coupled mass and momentum equations within the droplet. A sliding non-uniform orthogonal grid is implemented within the droplet, while an adaptive deforming grid accommodates the compressed / expanding gas phases at the ends of the microchannel. When

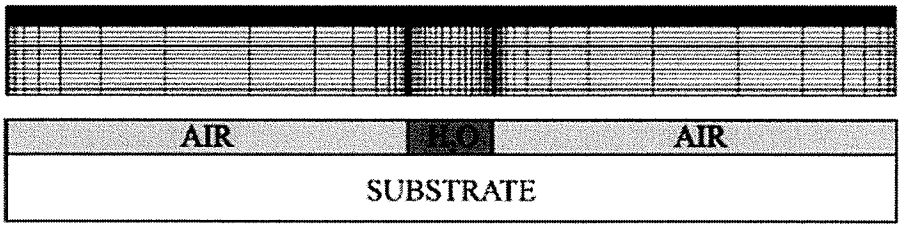

Figure 4.2: Temperature Mesh and Associated Phase Regions.

the droplet moves, these moving grids slide / stretch with a compliant uniform grid within the solid substrate (see Figure 4.2).

For heat transfer within the microchannel, integration of Eq. (4.4) over a discrete volume, V, and time step, Δt, yields

$$\underbrace{\int_t^{t+\Delta t}\int_V \frac{\partial}{\partial t}(\rho c_p T)dVdt}_{T1} + \underbrace{\int_t^{t+\Delta t}\int_V \frac{\partial}{\partial x}(\rho u c_p T)dVdt}_{T2} + \underbrace{\int_t^{t+\Delta t}\int_V \frac{\partial}{\partial y}(\rho v c_p T)dVdt}_{T3} = \underbrace{\int_t^{t+\Delta t}\int_V \frac{\partial}{\partial x}\left(k\frac{\partial T}{\partial x}\right)dVdt}_{T4} + \underbrace{\int_t^{t+\Delta t}\int_V \frac{\partial}{\partial y}\left(k\frac{\partial T}{\partial y}\right)dVdt}_{T5} + \underbrace{\int_t^{t+\Delta t}\int_V \dot{S}_T'''dVdt}_{T6} \quad (4.5)$$

The transient term is approximated with a backward difference, i.e.,

$$\int_t^{t+\Delta t}\int_V \frac{\partial}{\partial t}(\rho c_p T)dVdt \approx c_p\left(M_P T_P - M_P^o T_P^o\right) \quad (4.6)$$

where M_P is the mass of control volume P.

The x-convection term is approximated by

$$\int_t^{t+\Delta t}\int_V \frac{\partial}{\partial x}(\rho U c_p T)dV\,dt \approx \int_t^{t+\Delta t} c_p(\rho_e A_e U_e T_e - \rho_w A_w U_w T_w)dt$$
$$= \int_t^{t+\Delta t} c_p(\dot{m}_e T_e - \dot{m}_w T_w)dt \tag{4.7}$$

The lower case subscripts refer to variables along control faces while upper case subscripts refer to variables at nodal points. The predicted temperatures at the east (subscript e) and west (subscript w) integration points are determined from

$$T_e = \alpha_e T_P + (1-\alpha_e)\,T_E \tag{4.8}$$

$$T_w = \alpha_w T_W + (1-\alpha_w)\,T_P \tag{4.9}$$

where α is a dimensionless coefficient that depends on the Peclet number. This approach represents Peclet weighted upwinding of the convective flux [54].

The difference between heat flows by conduction across the east and west integration points is approximated as

$$\int_t^{t+\Delta t}\int_A\int_w^e \frac{\partial}{\partial x}\left(k\frac{\partial T}{\partial x}\right)dx\,dA\,dt = \int_t^{t+\Delta t}\left(k_e A_e \left.\frac{\partial T}{\partial x}\right|_e - k_w A_w \left.\frac{\partial T}{\partial x}\right|_w\right)dt \tag{4.10}$$

Using linear interpolation between nodal values of temperature, the following result is obtained for the temperature gradients at the edge of the control volume (see Figure 4.3),

$$\left.\frac{\partial T}{\partial x}\right|_e = \beta_e \frac{(T_E - T_P)}{(\Delta x)_e} \tag{4.11}$$

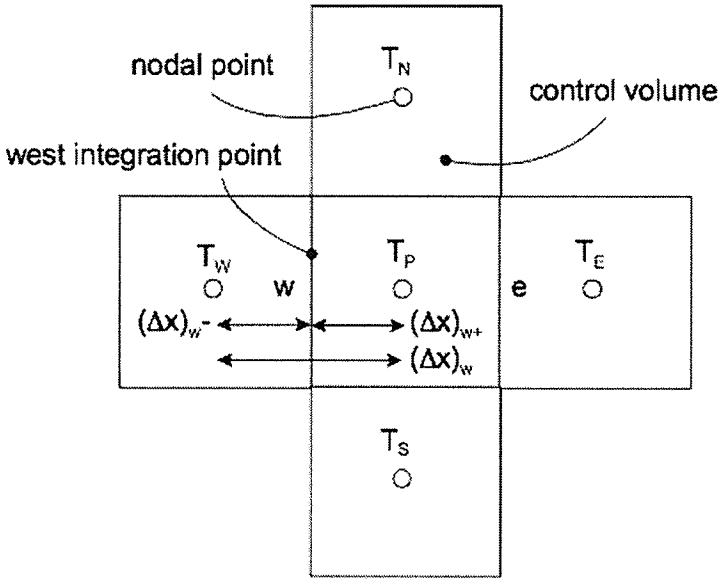

Figure 4.3: Full-Width Control Volume at a Phase Boundary.

$$\left.\frac{\partial T}{\partial x}\right|_w = \beta_w \frac{(T_P - T_W)}{(\Delta x)_w} \tag{4.12}$$

where β is a diffusion weighting coefficient [54].

A similar formulation is adopted for the y-direction component of heat conduction, thereby yielding

$$T5 = \left\{ \left[\frac{k_n A_n \beta_n}{(\Delta y)_n} \right] T_N + \left[\frac{k_s A_s \beta_s}{(\Delta y)_s} \right] T_S - \left[\frac{k_n A_n \beta_n}{(\Delta y)_n} + \frac{k_s A_s \beta_s}{(\Delta y)_s} \right] T_P \right\} \Delta t \tag{4.13}$$

Assembling the previous terms into Eq. (4.5) and dividing by Δt yields

$$a_P^T T_P = \sum a_{NP}^T T_{NP} + b_P^T \tag{4.14}$$

where

$$\sum a_{NP}^T T_{NP} = a_E^T T_E + a_W^T T_W + a_N^T T_N + a_S^T T_S \tag{4.15}$$

and

$$a_E^T = \max\left[0, (1 - 0.1\,|\mathrm{Pe}_e|)^5\right] \frac{k_e A_e}{(\Delta x)_e} + \max\left(-\dot{m}_e, 0\right) \tag{4.16}$$

$$a_W^T = \max\left[0, (1 - 0.1\,|\mathrm{Pe}_w|)^5\right] \frac{k_w A_w}{(\Delta x)_w} + \max\left(\dot{m}_w, 0\right) \tag{4.17}$$

$$a_N^T = \max\left[0, (1 - 0.1\,|\mathrm{Pe}_n|)^5\right] \frac{k_n A_n}{(\Delta x)_n} + \max\left(-\dot{m}_n, 0\right) \tag{4.18}$$

$$a_S^T = \max\left[0, (1 - 0.1\,|\mathrm{Pe}_s|)^5\right] \frac{k_s A_s}{(\Delta x)_s} + \max\left(\dot{m}_s, 0\right) \tag{4.19}$$

$$a_P^T = \frac{M_P}{\Delta t} + a_W^T + a_E^T + a_N^T + a_S^T \tag{4.20}$$

$$b_P^T = \frac{M_p^o}{\Delta t} T_P^o + \dot{m}_e - \dot{m}_w + \dot{m}_n - \dot{m}_s \tag{4.21}$$

The numerical procedure for solving the fluid flow equations can be summarized in the following steps. Firstly, the inlet and outlet boundary conditions for the u-velocity are calculated. The same u-velocity is specified at every node along both menisci to ensure that the droplet remains undistorted. Then, the momentum equations are solved with the current pressure field to obtain new u and v fields. Based on the current temperature field, the new thermocapillary pressure boundary conditions can be specified. Then, the pressure correction equation [54] is solved to obtain the new pressure (P) field. Finally, the u and v fields are corrected by the new P field and the steps are repeated until convergence is reached. More detailed information regarding these iterations and the steps within the SIMPLEC procedure are outlined in Ref. [54].

The discretized equations in this section are locally solved for each control volume. The predicted pressures, velocities and temperatures are stored at nodal points, which are centrally located within each control volume. At the end of each times step, the temperature mesh is regenerated to reflect the droplet translation. The following

section describes the momentum and temperature equation meshes, including their mutual interaction.

4.3 Adaptive Moving Grid Procedure

Fluid motion within the droplet will be predicted from a numerical simulation of the Navier-Stokes equations on a non-deforming momentum equation mesh. This momentum equation mesh slides over the stationary mesh on which the energy equations are solved. The temperature equation mesh is regenerated at the end of a time step and the temperature field within the substrate is transformed onto the newly generated mesh. The adaptive grid formulation was developed to accommodate the translation of the droplet and droplet mesh, relative to the substrate.

4.3.1 Bezier Mesh

The driving force on the droplet (which controls the fluid flow within the droplet) is highly dependent on the temperature distribution within the entire domain (air regions, droplet and substrate). Accurate predictions of the spatial gradients of temperature and velocity are required near each phase interface. Non-uniform Bezier grids, based on Bernstein polynomials, provide the necessary grid refinement near the phase boundaries. Grid refinement near phase boundaries reduces the number of control volumes within the domain, rather than increasing the entire grid density, thereby reducing computational costs. The form of the fifth-order Bernstein

polynomial is

$$g(x) = x/L = (1-t)^5 P_0 + (1-t)^4 t P_1 + (1-t)^3 t^2 P_2 + (1-t)^2 t^3 P_3 + (1-t) t^4 P_4 + t^5 P_5 \quad (4.22)$$

where t is the local coordinate bounded by $0 \leq t \leq 1$ and x/L is a fraction of the domain length. The P-variables are control points that control the mesh expansion ratio. The user specifies P_1, with other control points determined as follows,

$$P_0 = 0 \quad (4.23)$$

$$P_2 = 2P_1 \quad (4.24)$$

$$P_3 = 1 - P_2 \quad (4.25)$$

$$P_4 = 1 - P_1 \quad (4.26)$$

$$P_5 = 1 \quad (4.27)$$

It is required that

$$0 < P_1 < \frac{1}{4} \quad (4.28)$$

$P_1 = 0.2$ yields a uniform mesh. Each of the fluid regions may be assigned different values of P_1. The same value of P_1 is used for the pressure, velocity and temperature meshes. For a majority of simulations, the values of P_1 for the left air, droplet and right air regions were 0.01, 0.05 and 0.05, respectively.

The finite volume method uses a staggered grid, which requires a u-velocity mesh with one fewer column than that used for pressure and temperature. Figure 4.4

depicts the relation between typical P and u-velocity grids. A requirement of the u-velocity mesh is that the centers of the fictitious control-volumes are located along the outer edges of the outer-most columns of P control-volumes. Another requirement is that the widths of fictitious control-volumes are the same as its outer-most columns of internal control-volumes. This requirement reduces the complexity of applying external boundary conditions by locating the boundaries (control faces) of the P-mesh midway between u-velocity nodal points.

Examination of Figure 4.4 allows the length of the u-velocity mesh, L, to be derived based on an existing P mesh and the Bernstein polynomial of Eq. (4.22). Let the variable nx represent the number of columns of real control volumes in the P mesh. Based on these variables, it can be shown that

$$(L_0 - 2a)\, g\left(\frac{1}{nx-1}\right) = 2a \tag{4.29}$$

Re-arranging Eq. (4.29) yields an expression for a in the following form,

$$a = \frac{gL_0/(nx-1)}{2 + 2g/(nx-1)} \tag{4.30}$$

From Figure 4.4, it can be observed that

$$L = L_0 - 2a \tag{4.31}$$

Equations (4.30) and (4.31) are combined to yield the following expression for L.

$$L = \frac{(nx-1)}{L_0 nx - a + g} \tag{4.32}$$

After the value of L is determined, the function $g(t)$ can be used to generate the u-velocity mesh.

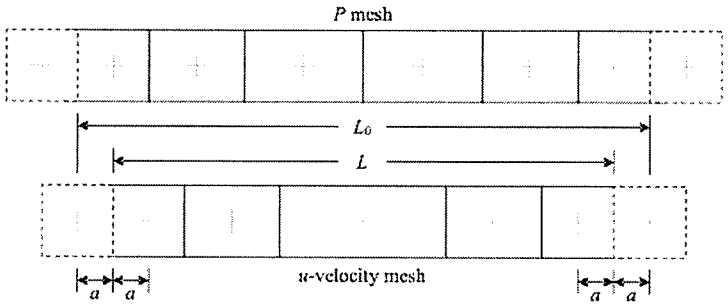

Figure 4.4: Pressure and Velocity Grids.

Unlike uniform meshes, u-velocity nodal points of staggered meshes are not located along control faces of pressure, v-velocity or temperature control volumes, as shown in Figure 4.4. A linear interpolation scheme was used to approximate the u-velocities (and thus mass flow rates) along control volume faces when generating coefficients of the P, v-velocity and T equations.

4.3.2 Temperature Formulation

The surface tension imbalance that drives droplet motion results from the temperature difference across a droplet. Only an accurate prediction of the temperature field will yield reasonable boundary conditions for the fluid flow equations. Only one system of equations is assembled for the temperature field. Each row of coefficients corresponds to Eq. (4.14) for a particular control volume. Although the form of the temperature equation is the same for each phase region, different assumptions are made when generating the coefficients.

The velocity fields are not predicted numerically within the air chambers. It was assumed that there is no v-velocity component, and the u-velocity varies linearly from zero at the lateral walls, to the bulk droplet velocity at the air/droplet interface. The pressure is assumed constant throughout the air chamber, and it is determined from ideal gas assumptions. The control volumes within the air chambers are regenerated after each time step to accomodate the dropet motion. The mesh expansion ratio (P_1) remains constant in Eq. (4.22). As a result, the control volumes traverse the microchannel with the same velocity as the fluid within them. The advection terms are neglected from the energy equations for the air regions, because there is no fluid flow across control volume faces. There would exist a v-velocity component along the air/droplet interface, and it would exactly match the droplet value. Heat transfer between the air and droplet occurs by conduction alone, since there exists no relative velocity between the two fluids.

Fluid motion within the droplet is predicted from a numerical simulation of the Navier-Stokes equations in the reference plane of the microchannel (stationary). The velocity field for a majority of the droplet resembles Poiseuille flow, with all of the fluid travelling in the same direction. The momentum equation mesh on which the velocity field is predicted traverses the domain at the droplet's bulk velocity, as does the droplet portion of the temperature mesh. The mass flow rate of fluid crossing control volume faces must be considered in the reference plane of the droplet. The velocity field predicted on the momentum mesh, minus the bulk droplet velocity, is used for the advection terms in the droplet portion of the temperature equation.

The newly predicted temperature field corresponds to the updated mesh in the gas and liquid regions, because the fluids within these regions move at the local bulk

speed of their respective control volumes. The substrate is a solid, experiencing no fluid flow. Thus the temperature mesh within the substrate is not updated with each time step. This creates a discontinuous mesh along the solid/fluid interface, as shown in Figure 4.5. To maintain mesh alignment between phases, the mesh within the substrate is updated with each time step and it remains aligned with the fluid meshes. This requires that the temperature field is updated with each time step. The temperature field in most of the new substrate mesh is linearly interpolated from the old temperature field and nodal point locations. Special attention is required near the thermal bridge, where control volumes are composed of several materials and they have composition changes with each time step. The assumption of a constant heat flux through these composite control volumes is made to approximate the temperature profile between nodal points (see Figure 4.6). The substrate temperature , T_N, corresponding to the new x-location, x_N, is specified as

$$T_N = T_L + \sum_{k=1}^{k=5} \left[\frac{l_k}{L_k} \frac{R_k}{R_{TOT}} (T_R - T_L) \right] \tag{4.33}$$

where T_L and T_R represent the left and right nodal temperatures bounding T_N. Also, l/L is the fraction of each composite region "overtake", R_k is the thermal resistance of a given region and R_{TOT} is the total thermal resistance between nodal points.

The droplet's velocity field must be adapted appropriately for the temperature equations. The resulting temperature field is used to generate the boundary conditions for the pressure correction equation. The determination of suitable pressure and velocity boundary conditions is discussed in the next section.

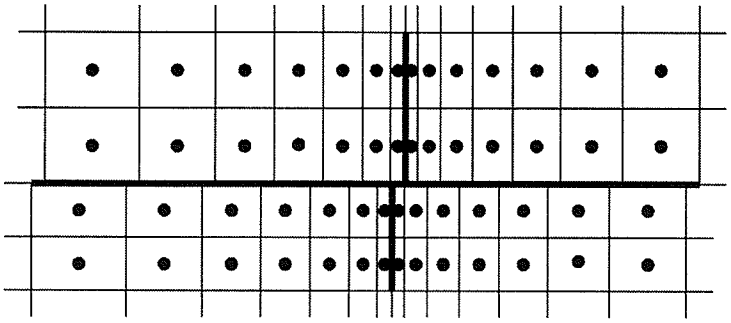

Figure 4.5: Mesh Misalignment Resulting from Not Regenerating the Substrate Mesh.

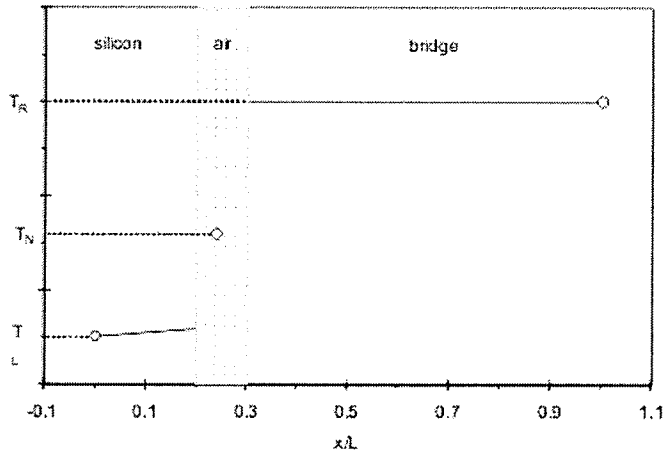

Figure 4.6: Steady-State Temperature Profile across a Composite Control Volume.

4.4 Pressure-Velocity Coupling

In addition to the governing equations (Eqs. (4.1) - (4.4)), boundary conditions are needed for problem closure. A no-slip condition is applied along the microchannel walls. Along the top of the domain (plane of symmetry), a zero-flux condition is placed on the u-velocity while the v-velocity is specified to be zero. Along the left and right edges, a zero-flux condition is applied for the v-velocity while a Dircihlet condition is

applied for the u-velocity. The same value is specified along the entire edge, ensuring that the droplet remains undistorted. After solving the mass-conserving velocity field, the pressure correction equation is solved and the velocity field is corrected. The u-velocity boundary condition for the new iteration requires that the boundary velocity yields the same mass flow rate as the corrected velocity field from the previous iteration. This boundary velocity is estimated in the following manner,

$$U_{bc} = \frac{\sum_{i=1}^{i_{max}} \left[\sum_{j=1}^{j_{max}} (u_{i,j}\, \Delta y_{i,j}) \right]}{i_{max} d} \tag{4.34}$$

where the subscripts i and j refer to the row and column numbers, respectively. The droplet displacement is calculated at the end of each iteration based on the updated bulk velocity. The mass of each air region in Figure 2.2 was calculated based on initial conditions and this mass remained constant during the simulations. As the droplet moves, the volumes of the air regions decrease / increase due to compression / expansion. The air pressures in the air region are calculated from the ideal gas law based on the region's average temperature, volume and mass. The updated external pressure is calculated based on this updated bulk velocity without actually displacing the droplet and regenerating the mesh. At the end of a time step, the droplet is translated and the mesh is regenerated.

The pressure boundary conditions were specified in the control volumes adjacent to the wall for both left and right boundaries of the droplet. A reference pressure of zero was maintained in the right control volume. The unknown driving pressure in the bottom left corner is the value that yields an average pressure difference across the droplet equal to ΔP, which is the sum of the thermocapillary pressure caused by the

difference of surface tension across the droplet and the external pressure difference. The pressure in the bottom left corner of the droplet was iteratively determined in following way,

$$P_L^{m+1} = P_L^m + \left[\left(\overline{P}_R - \overline{P}_L\right)^m - \Delta P_{spec}\right] \tag{4.35}$$

This local pressure specification induces fluid motion outwards from the corners of the droplet. The superscripts m and $m+1$ indicate values at the previous iteration and current iteration, respectively. The average left and right pressures represent the weighted averages of pressures across the left and right boundaries of the droplet, respectively. The difference of the average pressures equals the specified pressure difference across the droplet (i.e., $P_L^{m+1} = P_R^m$) upon convergence.

In the next section, the numerical formulation for implementing internal conjugate interface conditions is developed.

4.5 Heat Transfer at the Moving Droplet / Air Interface

Accurate temperature calculations at both ends of the droplet are needed to accurately predict the thermocapillary pressure. The temperature field within the droplet depends on heat exchange with the surrounding substrate and air regions. The governing equation for temperature within the air regions excludes advection because control volumes are assumed to be moving at the speed of the air phase. The two-dimensional transient heat conduction equations are solved within the silicon substrate, thermal bridge and air regions. A thin air gap was placed between the thermal bridge and

adjoining substrate, in order to reduce lateral heat losses through the thermal bridge. Thus, energy input is primarily transferred to the droplet in the microchannel, not laterally through the substrate.

Past studies [27] have applied Dirichlet temperature boundary conditions along the entire channel wall without consideration of the substrate, while others [28] have applied a Dirichlet heater boundary condition along the substrate / fluid interface. Unlike these studies with specified boundary conditions at the substrate / droplet interface in an open microchannel, the problem configuration in Figure 2.2 applies heater boundary conditions along the substrate wall with a conjugate boundary condition along the substrate / fluid interface, since temperatures and heat flows along the microchannel walls are unknown. For example, at the interface between the substrate and droplet (along the microchannel wall), a conjugate boundary condition is needed for implicit coupling between heat conduction in the solid and convection in the fluid. Similarly, conjugate conditions are needed at the moving droplet / air interface.

The interfacial energy balance at the droplet (subscript d) / air (subscript a) interface is

$$\left(-k\frac{\partial T}{\partial x}\right)_d = \left(-k\frac{\partial T}{\partial x}\right)_a \tag{4.36}$$

With a conventional implementation of the external boundary condition, each of the four phase domains would be solved separately, with boundary temperatures matched in an iterative manner. Avoiding iteration by solving the temperature field throughout the domain would be highly beneficial, as it would greatly reduce computational time. However, Eq. (4.36) cannot be readily implemented internally as a boundary condition, if full width control volumes are used (see Figure 4.3, where

control volume P is within the droplet, while control volume W is within the air). All temperatures are stored at nodal points, which are centrally located within the control volumes. Thus, the integration point temperature of the meniscus, T_w, requires interpolation between T_W and T_P.

Consider again the discretized form of Eq. (4.36) at the droplet / air interface. Typical full-width control volumes and mesh spacings are illustrated in Figure 4.3. Using a compass notation, with the P control volume associated with the droplet, Eq. (4.36) becomes

$$k_W \frac{T_w - T_W}{(\Delta x)_{w-}} = k_P \frac{T_P - T_w}{(\Delta x)_{w+}} \tag{4.37}$$

Uppercase subscripts designate a nodal value, while lowercase subscripts refer to a control volume edge value. A lever rule approximates the interface temperature as

$$T_w = \frac{(\Delta x)_{w-}}{(\Delta x)_w} T_P + \frac{(\Delta x)_{w+}}{(\Delta x)_w} T_W \tag{4.38}$$

This result is used to re-arrange Eq. (4.37) in the following manner,

$$k_W \frac{T_P - T_W}{(\Delta x)_w} = k_P \frac{T_P - T_W}{(\Delta x)_w} \tag{4.39}$$

The above equation can be true only if $k_W = k_P$, or if the temperature fluxes are zero. An appropriate prediction of T_w requires consideration of the transient temperature profile through each phase. This requires additional variables and computational cost.

The shortcoming of full-width control volumes for conjugate boundary conditions is addressed by locating zero-width control volumes (10^{-32} m thickness in the nu-

merical model) along the conjugate boundaries. The zero-width control volumes successfully enforce Eq. (4.36) without receiving any special attention at the substrate / droplet, substrate / air, or droplet / air interfaces. The energy balance for the P control volume in Figure 4.7 becomes

$$k_W \frac{T_P - T_W}{(\Delta x)_w} = k_E \frac{T_E - T_P}{(\Delta x)_e} \tag{4.40}$$

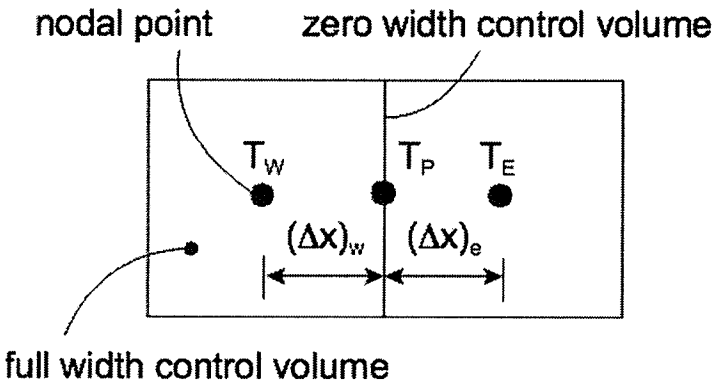

Figure 4.7: Zero-Width Control Volume at a Phase Boundary.

The masses in both air regions of Figure 2.2 are calculated from initial conditions. These masses remain constant throughout the simulations, but the volumes increase / decrease when the droplet moves. The air pressures are calculated based on each region's average temperature, volume and mass from the ideal gas law. The velocity of the air is assumed to vary linearly from zero at the wall to the bulk droplet velocity at the droplet / air interface.

Unlike past studies, these numerical simulations allow detailed predictions of fluid flow and heat transfer within the moving micro-droplet. Since these CFD simulations can become very time-consuming, the previously described SA Model (Chapter

3)provides useful guidance in regards to overall trends in the system. For example, it provides reasonable predictions regarding effects of geometrical changes, different working fluids and temperature boundary conditions. In the next chapter, results from both analytical and numerical formulations will be presented and compared.

4.6 Temperature Boundary Conditions

In addition to the "internal boundary condition" described in the previous section, boundary conditions are applied along the outer perimeter of the temperature domain. Only the bottom half of the domain is simulated due to problem symmetry. A Robin temperature boundary condition is applied to the left, right and bottom edges of the domain. The environment temperature is assumed to be 20 °C with a heat transfer coefficient of 37 W/m^2K, as suggested in Ref. [28]. A zero-flux temperature boundary condition is applied along the symmetric top edge of the domain. The heater boundary conditions are applied along the interface between the thermal bridge and heat source. Both Neumann and Dirichlet boundary conditions were implemented, but Dirichlet boundary conditions were used for almost all simulations. An algorithm was developed to search the domain to determine to which control volumes the lateral edges of the thermal bridge belong. All control volumes completely contained within the thermal bridge have their boundary conditions specified according to the methodology of Patankar [54]. If Dirichlet boundary conditions are required, a weighted average temperature is specified along the edge of the control

volume that contains the edges of the thermal bridge, so

$$T = \left(\frac{L_B}{L_{CV}}\right) T_B + \left(\frac{L_{\mathrm{CV}} - L_B}{L_{CV}}\right) T_{CV}^{\mathrm{old}} \tag{4.41}$$

where L_B is the length of the thermal bridge within the control volume, L_{CV} is the length of the control volume, and T_{CV}^{old} is the boundary temperature of the control volume from the previous time step. If Neumann conditions are required, the heat flux is sccaled relative to the fraction of the control volume that comes into contact with the heat source, so

$$q'' = \left(\frac{L_B}{L_{CV}}\right) q''_{\mathrm{spec}} \tag{4.42}$$

where q''_{spec} is the user-specified heat flux between the heat source and the thermal bridge.

This chapter has presented a numerical formulation to precit thermocapillary pumping in closed-end microchannels. The next chapter presents validations for both the theoretical model and the numerical formulation, as well as discussions of simulations with each method.

Chapter 5

Results and Discussion

Chapters 3 and 4 have presented several new methods of predicting thermocapillary pumping in closed-end microchannels. These methods may be used to predict system characteristics of the micro heat engines proposed in Chapter 2. This chapter presents results of various simulations using both theoretical and numerical models develped in Chapters 3 - 4.

5.1 Validation of the Theortical Model

The theoretical model must be validated before it can be used to predict physical trends associated with TCP. The theoretical model was developed in stages, with each stage tested as the model evolved.

5.1.1 Prescribed Forcing Function

The first stage of the model simulated the motion of a solid body affected by external body forces. The following sinusoidal forcing function was chosen,

$$F = \sin t \tag{5.1}$$

The mass of a slug was assumed to be 3 kg. Integrating Eq. (5.1) provides the following analytical velocity field,

$$U = \int_{t=0}^{t=T} \frac{F}{m} dt = \frac{1 - \cos T}{m} \tag{5.2}$$

Integrating again yields the slug position,

$$x = \int_{t=0}^{t=T} U dt = \frac{T - \sin T}{m} \tag{5.3}$$

This theoretical model was used to predict the motion of the body. The theoretically predicted velocity and position histories are compared against the analytically determined histories (obtained by integrating Eq.(5.1)) in Figure 5.1. The results are too close to be distinguished.

After the formulation of Newton's Second Law of Motion was validated, a framework of TCP was implemented. The thermocapillary force was added, based on the temperature at the receding edge of the droplet. The temperature of the advancing edge of the droplet was assumed to remain unchanged. The relationship between the droplet displacement and air pressure was established and the frictional drag force was incorporated.

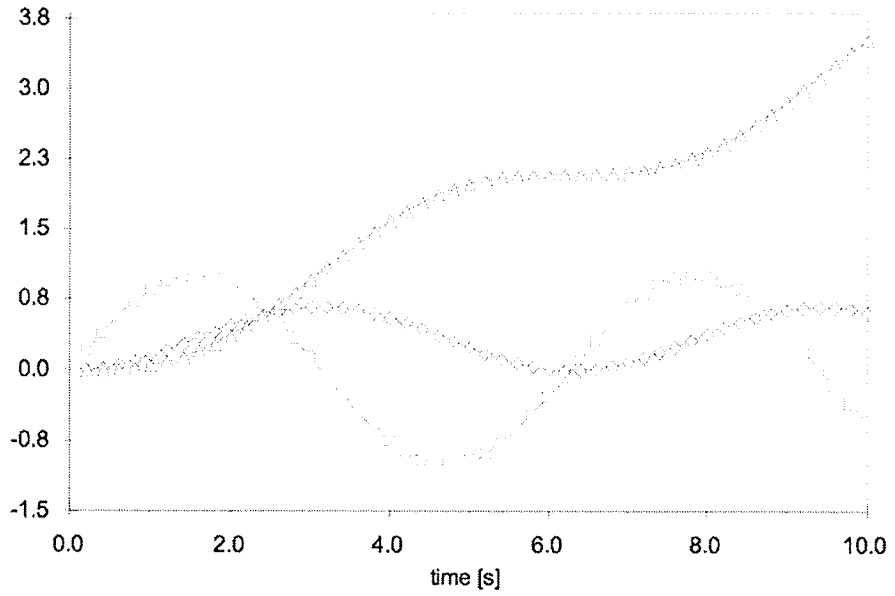

Figure 5.1: Comparison Between Analytical and Theoretical Solutions for Velocity and Displacement. The Units of Force (□), Velocity (◇) and Position (△) are [N], [m/s] and [m], respectively.

5.1.2 Transient Poiseuille Flow

The droplet dynamics was first tested by applying a constant pressure gradient across the droplet, which would be equivalent to maintaining a constant temperature along the receding edge of the droplet. The theoretical model was used to predict the motion of the droplet and the results were compared against the following analytical solution.

$$u(y,t) = -\frac{d^2}{2\mu}\frac{\partial P}{\partial x} \left\{1 - \left(\frac{y}{d}\right)^2 - \frac{32}{\pi^3}\sum_{k=1}^{\infty}\frac{(-1)^{k+1}}{(2k-1)^3}\cos\left[\frac{(2k-1)\pi}{2}\frac{y}{d}\right]\exp\left[-\frac{(2k-1)^2\pi^2}{4d^2}\nu t\right]\right\} \quad (5.4)$$

The results of this comparison may be found in Figure 5.2.

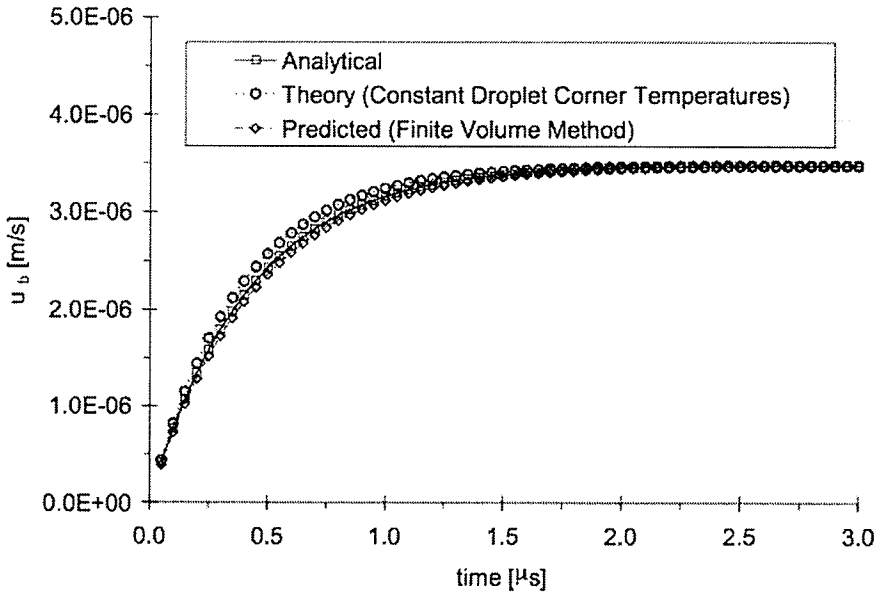

Figure 5.2: Comparison Between Theoretical Prediction and Analytical Solution of the Transient Bulk Velocity for Poiseuille Flow with a Constant Pressure Gradient.

The theoretical model slightly over-predicts the bulk velocity in the early developing stages of the flow. This is due to the fact that the frictional drag force is estimated with the assumption of a fully developed velocity profile for each time step. For early time steps, the velocity profile is actually flatter than the fully developed profile. The velocity gradient at the wall and the wall shear stresses are higher than values associated with fully developed flow, thereby leading to an under-prediction of frictional drag.

5.1.3 Contant Pressure Pumping in a Closed Microchannel

After the theoretical model successfully predicted transient Poiseuille flow in an open channel, the ends of the channel were then closed. The air upstream and downstream

of the droplet will now experience expansion and compression, respectively, when the droplet translates. There is no available analytical solution for this problem. The theoretical model was compared against the FVM predictions in Figure 5.3. Both methods were used to simulate transient droplet translation in a closed channel.

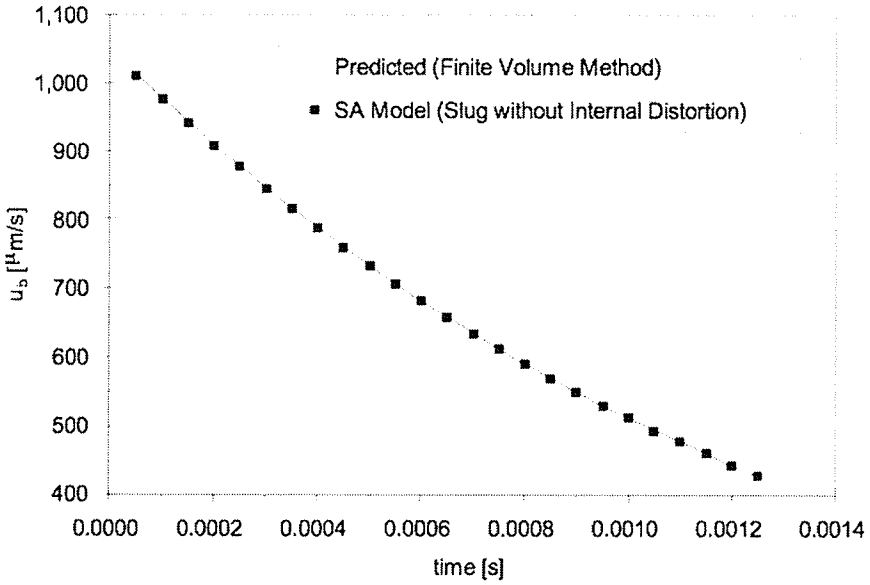

Figure 5.3: Comparison of Theoretical and FVM Predictions of Bulk Droplet Velocity for Constant Pressure Flow in a Closed Microchannel.

The results from different methods in Figure 5.3 are so close that they cannot be distinguished. This suggests that the theoretical model reasonably matches the physics of the full FVM. Given the correct boundary condition for the thermocapillary pressure, the theoretical model may be used to predict the droplet translation. The next (more difficult) step is to implement heat transfer into the theoretical model, to predict the temperature at the receding corner of the droplet.

5.1.4 Thermocapillary Pumping in a Closed Microchannel with Specified Left Droplet Temperature

The final step in the validation of the theoretical model is to implement the temperature difference across the droplet for the driving force of the droplet motion. This will be accomplished in two steps. This sub-section will present the case where the temperatures of the droplet ends are prescribed for each time step. This will ensure that the driving force is correctly implemented. The next subsection will approximate the temperature of the left edge of the droplet, as described in Chapter 3.

For this validation, the droplet's left temperature was specified for each time step. The temperature values were imported from a data file generated by simulations based on the FVM in Chapter 4. The droplet"s right temperature was assumed to remain at its initial temperature.

The FVM simulation was allowed to proceed until the droplet reached its peak displacement twice. This should provide sufficient information about the droplet dynamics to allow a reasonable evaluation. About 0.009 seconds of TCP was simulated, for which the appropriate temperature data were exported. The theoretical model was used to simulate the same TCP conditions using the imported temperatures. The resulting velocity history may be seen in Figure 5.4. The theoretical and FVM results are too close to distinguish, indicating that the theoretical model imposed the correct driving force based on the temperatures at the droplet ends.

The validations presented in section 5.1 indicate that a theoretical model based on Newton"s Second Law yields reasonable results for thermocapillary pumping in closed microchannels, provided that an accurate predication of the temperature distribution

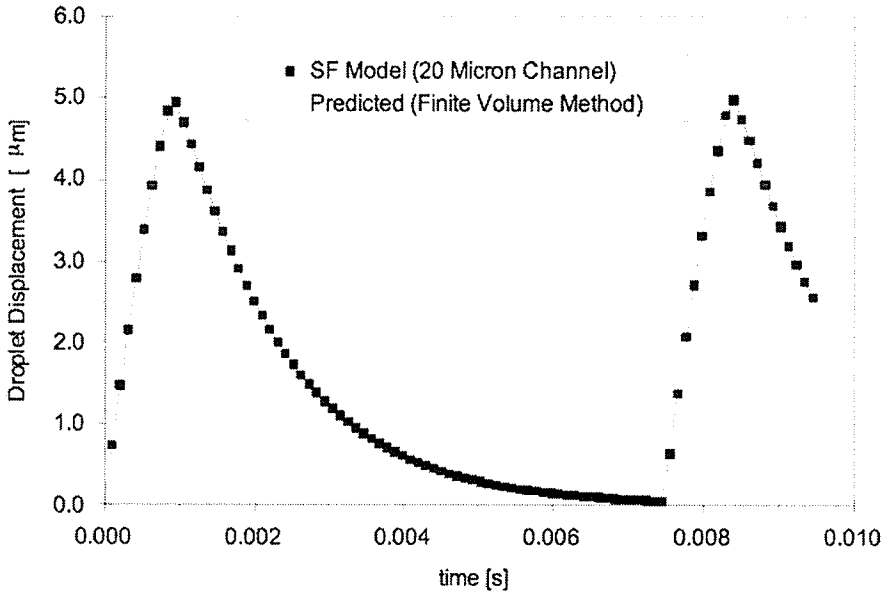

Figure 5.4: Comparison of the Theoretical and FVM Predictions Droplet Displacement for TCP in a Closed Microchannel with the Left Temperature Specified.

is available. Additionally, treating the domain as two semi-infinite solids during heating, while using a lumped capacitance method during cooling, accurately predicts trends involving droplet temperature, velocity and displacement. It would appear that the model can be used to predict the effects of varying channel geometry, thermal boundary conditions or different fluids. The theoretical model will be used to predict thermocapillary pumping in closed-end microchannels in section 5.5.

5.2 Effects of Microchannel Height on Microdroplet Dynamics

In order to examine the effects of channel height on the dynamic forces, droplet velocities and displacements, the theoretical model was used to simulate thermocapillary pumping in closed microchannels with three different channel heights: 0.5 microns, 1 micron and 2 microns. The heights represent the channel height simulated numerically (1 μm), as well as half and double this size. The simulation parameters are the same as values used for validating the semi-infinite solid assumption in section 5.5.

Examination of Eq. (3.21) indicates that the capillary force is independent of channel height (with $A = db$), except through the dependence of the temperature on the channel height. Equation (3.22) reveals that the air force is directly proportional to the channel height. It is also a function of air temperatures, air volumes, and therefore the droplet displacement. Equation (3.25) indicates that the frictional force is inversely proportional to the channel height. However, it is also a function of the droplet velocity. Changing the channel height affects all of the forces differently, and some of the forces are dependent on others. Thus, it is not intuitive what effect a change in the channel height will have on TCP.

To determine the effect of channel height, TCP was simulated for 2 ms for each of the three channel heights. The heat source was removed when the droplet had been displaced 5 microns. The resultant force history can be found in Figure 5.5. Figure 5.5a shows that the thermocapillary force follows almost the exact same curve for all of the channel heights. This occurs because all of the channel heights are small, relative to the thickness of the substrate, thereby resulting in only slight variations in

the net values of α for each geometry. The time at which the microdroplet attains its maximum displacement, however, varies with channel height. Figure 5.5b indicates that the external air force is proportional to the channel height. While equal droplet displacements yield equal external pressures, the force is directly proportional to the droplet height. Figure 5.5c indicates that the frictional drag force is smaller for droplets in larger channels. This is supported by Eq. (3.25), which indicates that the frictional force is inversely proportional to the channel height.

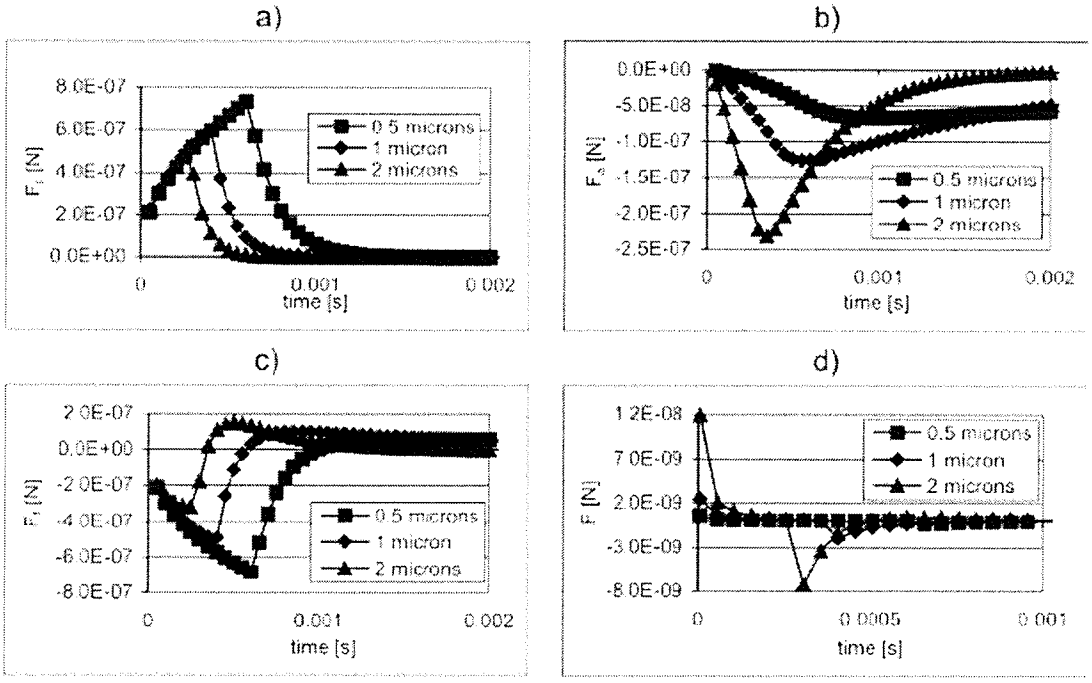

Figure 5.5: Comparison of Forces Acting on Microdroplets of Varying Height.

Newton's Second Law of Motion indicates that the acceleration of the droplet is inversely proportional to the mass of the droplet. This indicates that doubling of the channel height would require a doubling of the net force acting on the droplet, if identical droplet displacement histories were desired. Figure 5.5d indicates that the

net force acting on the droplet in the largest channel is more than four times as large as the force acting on the droplet in the smallest channel. Thus, the droplet in the largest channel should accelerate faster and reach a displacement of 5 microns in a shorter time. Similar arguments hold for the 1 μm channel. The droplet displacement histories of Figure 5.6 and the droplet bulk velocity histories of Figure 5.7 show these trends. It should be noted that the net force acting on the droplet becomes negative shortly after the heat source is removed, resulting in a rapidly decreasing thermocapillary force.

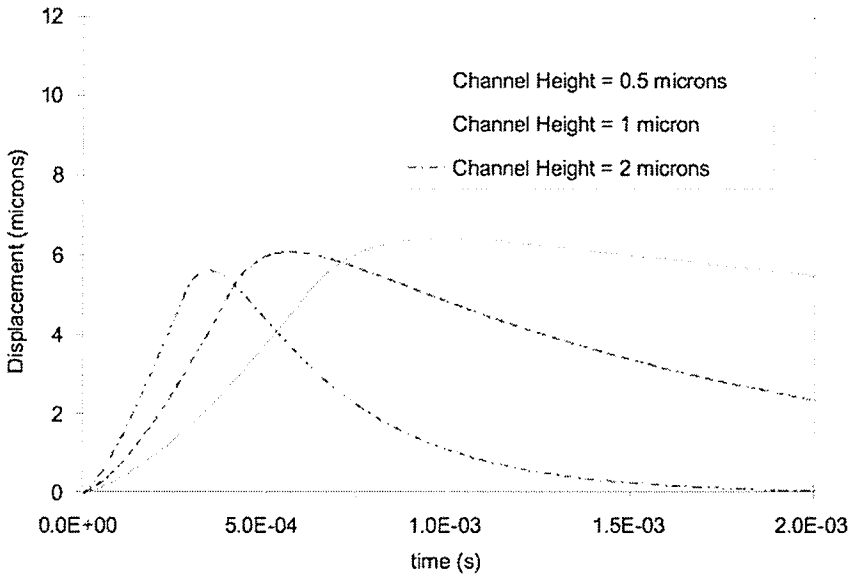

Figure 5.6: Comparison of the Effect of Microchannel Height on the Displacement History.

Figure 5.6 and Figure 5.7 indicate that increasing the channel height decreases the time required for the droplet to be displaced 5 μm. Figure 5.6 also indicates that larger droplets experience smaller overall displacements, and they will produce less external pressure. In practical aplications, this information could be used to match a

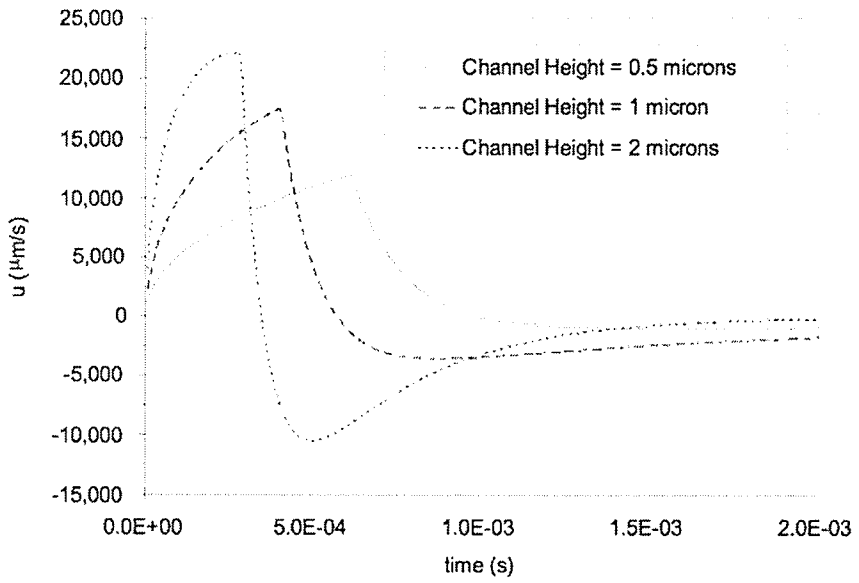

Figure 5.7: Comparison of the Effect of Microchannel Height on the Bulk Velocity.

given resonance frequency or achieve a given pressure requirement of a thermal switch or valve.

5.3 Validation of the Finite-Volume Method

The FVM needs to be validated before it can be used to confidently predict thermocapillary droplet motion. Both heat transfer and fluid flow portions of the numerical code were validated separately by comparing simulation results with analytical solutions for both transient conduction within a rectangular plate and developing channel flow. This section presents results of these validations.

5.3.1 Transient Cooling of a Stationary Fluid Element

An important component of the thermocapillary pumping problem is transient heat conduction, so a test problem of two-dimensional transient conduction was studied for validation purposes (see Figure 5.8). The domain was initially at $T = 1°C$. At time $t = 0$, the four edges were suddenly brought to $T = 0°C$. A square domain with side lengths of 60 μm (similar to the length scale of 48 μm used later in the thesis) was discretized with a 30×30 mesh. Due to the problem symmetry, the temperature distribution was predicted only in the upper right quadrant of the domain, with zero gradient boundary conditions along the interior boundaries. The mesh was divided into six regions, corresponding to the fluid and solid portions of the left air, droplet and right air regions of the TCP formulation. Zero-thickness control volumes were implemented between region boundaries. The fluid properties are k = 1 W/mK (thermal conductivity), ρ = 1,000 kg/m^3 (density) and c_p = 1,000 J/kgK (specific heat), so that $\alpha = 1 \times 10^{-6}$ m^2/s (thermal diffusivity). The time step for the numerical simulations was selected to be $\Delta t = 1 \times 10^{-4}$ s.

The analytical solution for this problem can be derived from a product of two 1-D solutions, involving heat conduction in a semi-infinite medium [55]. The 1-D solution in the x-direction may be written as

$$T(x, l, t) = \frac{4}{\pi} \sum_{n=0}^{\infty} \left\{ \frac{(-1)^n}{2n+1} \exp\left[-\frac{\alpha (2n+1)^2 \pi^2 t}{4l^2} \right] \cos\left[\frac{(2n+1)\pi x}{L} \right] \right\} \tag{5.5}$$

where l is the half-length of the domain (i.e. $l = L/2$) and α is the thermal diffusivity. An expression similar to Eq. (5.5) exists for the y-direction. Then, the product of the

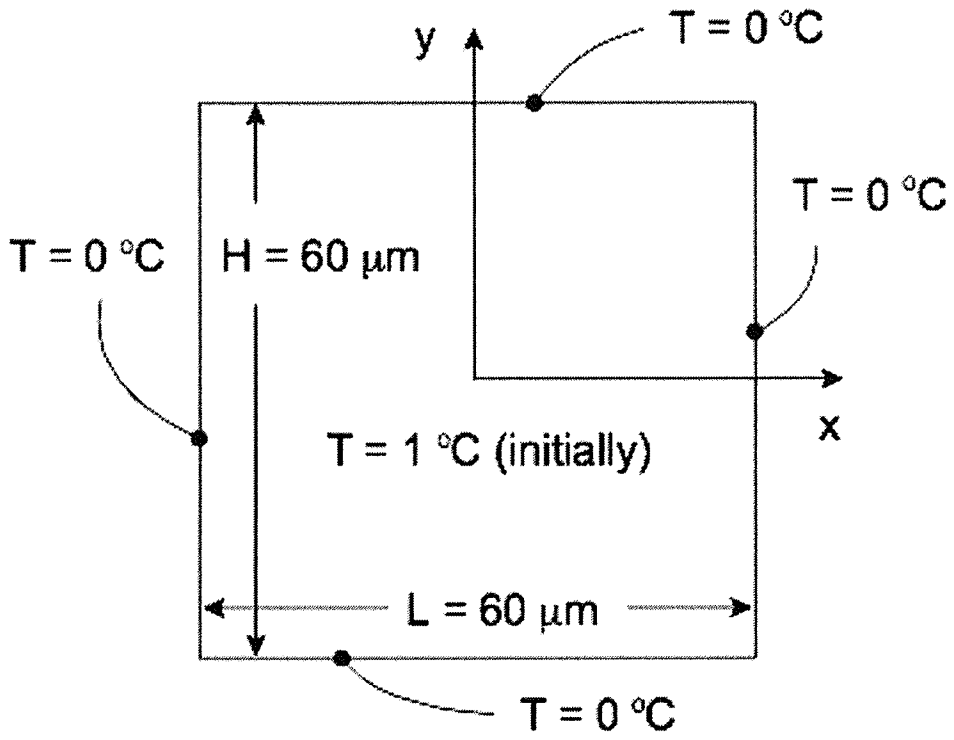

Figure 5.8: Domain for Two-Dimensional Transient Conduction.

two 1-D solutions becomes

$$T(x, y, l, h, t) = T(x, l, t)\, T(y, h, t) \tag{5.6}$$

The 1-D solution of Eq. (5.5) was predicted first, with zero gradient boundary conditions imposed along the upper and lower boundaries of the domain. Figure 5.9 shows a plot of the errors for the first ten time steps of the 1-D solution in the region

of $0 \leq x \leq 30 \times 10^{-6}$. The error was defined as

$$\text{Error} = \frac{T_S - T_A}{T_{A,\max}} \tag{5.7}$$

where the subscripts S and A refer to simulated and analytical results, respectively. The absolute errors were normalized by the maximum temperature within the domain, rather than local temperatures, because the temperatures are very close to zero near the boundaries and higher time step values.

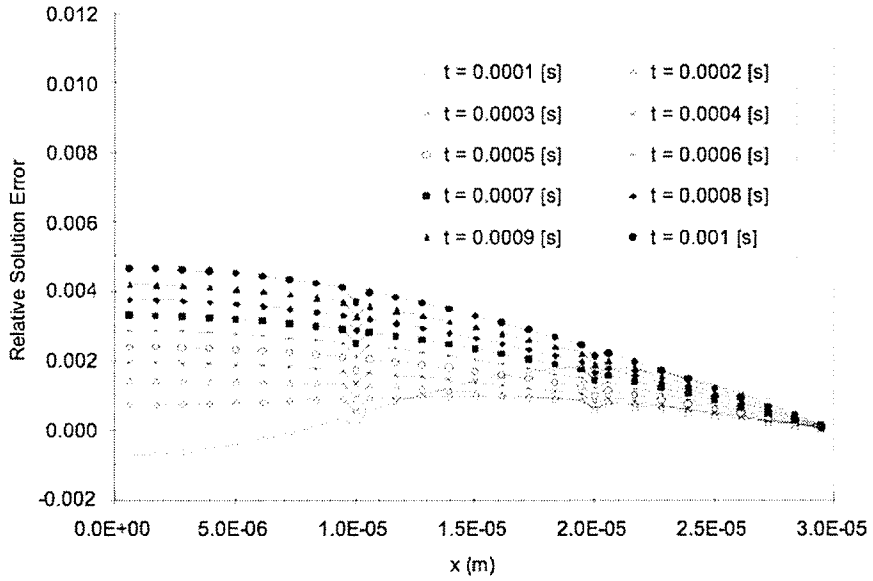

Figure 5.9: Relative Solution Error of Predicted Temperature for Transient Cooling.

The discontinuities in the error curves, located at $x = 10$ μm and $x = 20$ μm, correspond to the locations of the zero-width control-volumes that would be located at phase boundaries when simulating TCP. It can be seen that the error is rising for each time step. The error is everywhere less than one percent for the time steps

shown. This error could be lowered with grid refinement and a reduction in the time step. It was confirmed that the steady-state temperature field of $T = 0°C$ was achieved.

After the 1-D solution was validated, a 2-D simulation of Eq. (5.7) was performed. Figure 5.10 shows a plot of the average error for the domain defined by $0 \leq x \leq 30 \times 10^{-6}$ and $0 \leq y \leq 30 \times 10^{-6}$ for the first 10 time steps of the 2-D solution, where the error is defined as

$$\overline{\text{Error}} = \frac{\text{average}\,(T_S - T_A)}{T_{A,\max}} \tag{5.8}$$

The errors are slightly larger than the case of the 1-D solution. This result is expected when errors from the 1-D solutions are combined.

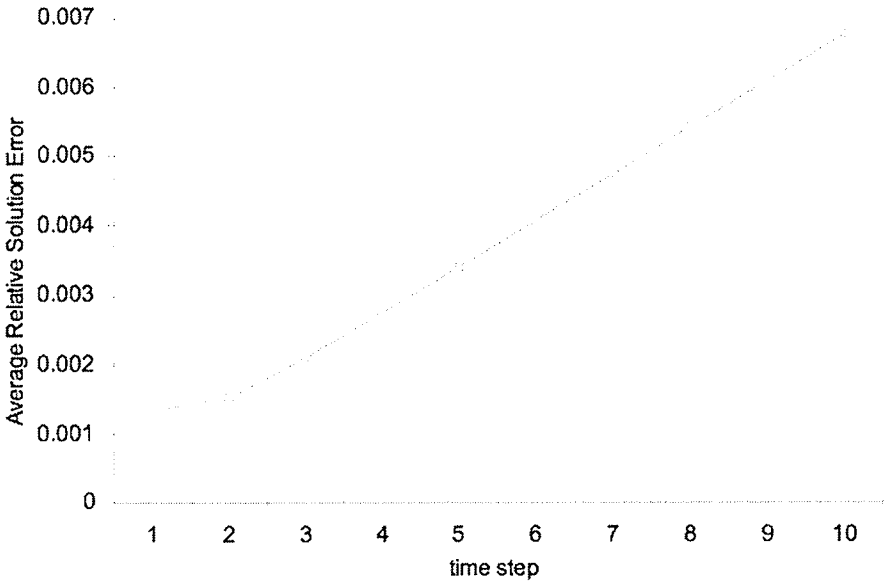

Figure 5.10: Relative Solution Error for Two-Dimensional Transient Cooling.

This study indicates that the FVM accurately predicts transient cooling of a stationary fluid element, even for a coarse mesh. Transient heating of a stationary

fluid element is considered next.

5.3.2 Transient Heating of a Stationary Fluid Element

In order to further validate the use of zero-thickness control volumes in the finite volume model, transient heating of a droplet was simulated. The domain was discretized to match the case of solving cyclic thermocapillary pumping in closed-end microchannels (refer back to Figure 4.2). A heat source was applied to the entire bottom surface of the domain and the thermal bridge was removed. Zero-flux boundary conditions were specified along the left and right edges of the domain. The properties of water were specified everywhere in the domain, in order to compare predicted results with the analytical solution for the heating of a semi-infinite solid [55]. The simulation parameters are the same as values used in the upcoming thermocapillary pumping problem (see Table 5.1). In Figure 4.2, both air and substrate regions were replaced with water. The simulation was performed until the temperature of the top surface (line of symmetry) changed from its initial value. Figure 5.11 compares the simulated temperature profiles against analytical values for two time steps. There was no lateral variation of temperature across the zero-width control volumes corresponding to the liquid / gas interfaces during thermocapillary pumping. Figure 5.11 shows that no discontinuity in the temperature gradient exists along the horizontal plane of the zero-height control volumes (where the horizontal spacing of symbols on the graph changes). It was also verified that no temperature discontinuity existed across the zero-width control volumes corresponding to the liquid / gas interfaces.

The simulations in this section and the previous section confirm that conduction within the domain is accurately predicted during both heating and cooling periods.

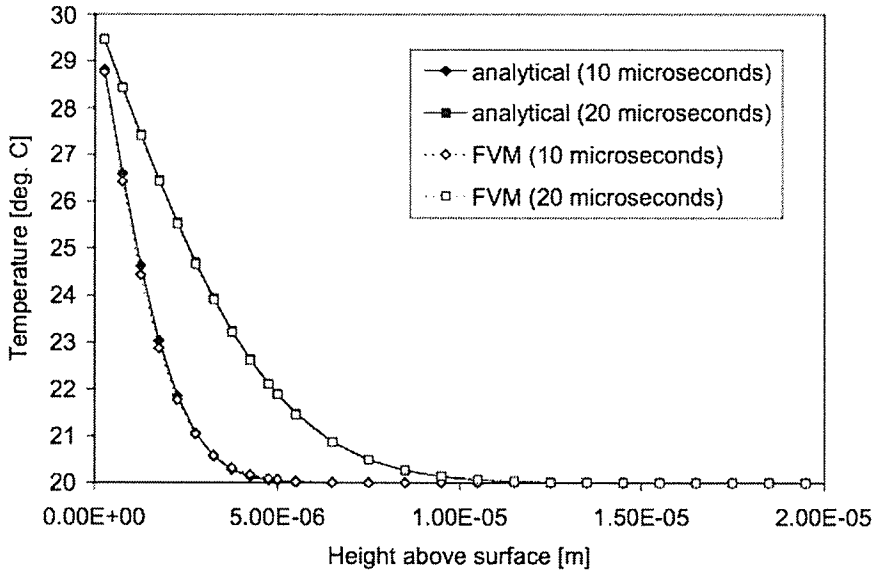

Figure 5.11: Transient Heating of Stationary Fluid Element (Semi-Infinite Solid) with Zero-Width Boundary Control Volumes.

The following simulations validate the predictions of fluid flow within the domain.

5.3.3 Transient Poiseuille Flow in an Open Microchannel

The numerical formulation for fluid flow was initially validated by simulation of transient Poiseuille flow in an open-ended microchannel. The flow is induced by a suddenly applied pressure gradient at time $t = 0$. Water was enclosed between two parallel plates separated by a distance of $d = 30$ microns. Initially ($t = 0$), the liquid was motionless and a constant pressure gradient was applied across the channel, thereby setting the fluid into motion. The pressure drop across the channel was specified as 1 Pa and the time step size was 0.0001 ms. A summary of the simulation parameters may be found in Table 5.1.

Table 5.1: Simulation Parameters for Transient Poiseuille Flow in an Open-Ended Microchannel.

Property	Value
Density of Droplet (ρ)	1000.0 kg/m^3
Dynamic Viscosity (μ)	0.001 Ns/m^2
Time Step (Δt)	0.001 ms
Domain Length (L)	30 μm
Domain Height(d)	30 μm
Number of x **control volumes** (nx)	20
Number of y **control volumes** (ny)	20 / 80
Pressure Difference (ΔP)	1.0 Pa

The analytical solution for transient developing channel flow is given by

$$u(y,t) = -\frac{d^2}{2\mu}\frac{\partial P}{\partial x} \left\{1 - \left(\frac{y}{d}\right)^2 - \frac{32}{\pi^3}\sum_{k=1}^{\infty}\frac{(-1)^{k+1}}{(2k-1)^3}\cos\left[\frac{(2k-1)\,\pi}{2}\frac{y}{d}\right]\exp\left[-\frac{(2k-1)^2\,\pi^2}{4d^2}\nu t\right]\right\} \quad (5.9)$$

This analytical result is compared against predicted velocities from the FVM formulation. In the numerical simulations, the applied boundary conditions were no-slip conditions along the top and bottom walls and a zero flux along the inlet and outlet faces of the channel for both u and v velocity components. A reference pressure was specified as zero in the wall control volumes at the channel outlet. At the channel inlet, the pressure was specified in the wall control volumes as ΔP_{spec}. The length for specifying the pressure gradient is the distance between two pressure specification points in the staggered grid formulation.

Figure 5.12 illustrates close agreement between analytical and predicted velocities at different times in the microchannel. The spatial velocity profile is symmetric about

the centerline of the microchannel, so only results in a half-portion of the microchannel are depicted. For each time increment of plotted data (0.0002 ms), the fluid velocity in the core of the microchannel increases by about 6.7 μm/s. During this period, the thickness of the boundary layer increases due to transient diffusion of momentum along the wall. The flow becomes fully-developed when boundary layers along each wall merge in the centerline of the microchannel. Such fully-developed conditions are shown in Figure 5.12. For both developing flow (Figure 5.12) and fully-developed flow in a microchannel (Figure 5.12), close agreement between analytical and predicted FVM results is obtained.

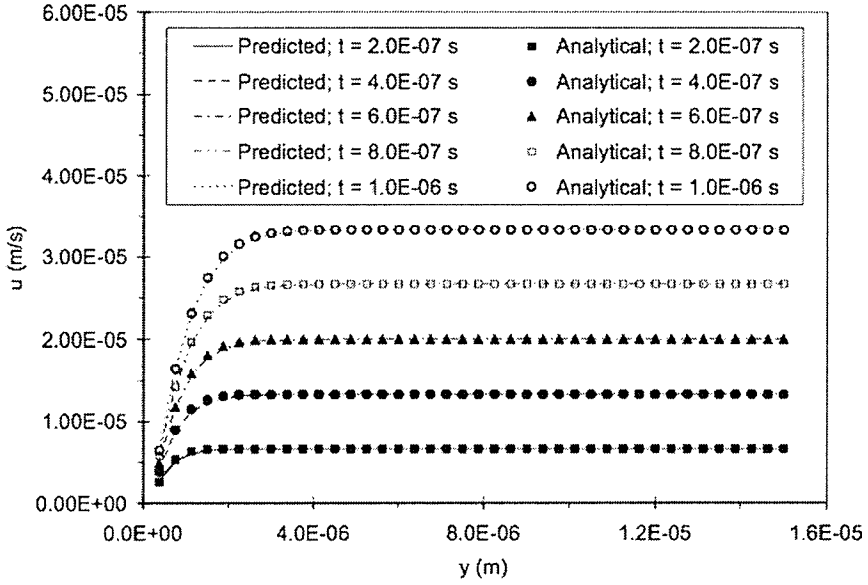

Figure 5.12: Predicted Developing Velocity Profiles and Comparison with Analytical Solutions.

The solution error of velocity was calculated at each location (see Figure 5.14) and time step number (Figure 5.15, note: each time step corresponds to 0.0001 ms), based on

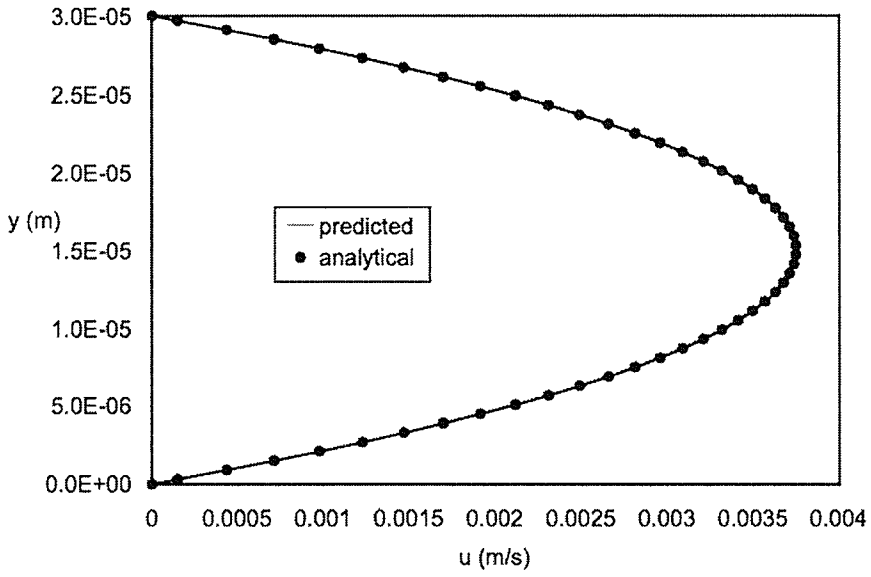

Figure 5.13: Fully Developed Velocity Profile in Open-Ended Microchannel Flow.

$$\text{Error} = \frac{u_p - u_a}{u_{A,\max}} \tag{5.10}$$

where u_p and u_a refer to the predicted (FVM) and analytical velocities, respectively. The spatial variations of solution error are shown in Figure 5.14. It can be seen that significant error exists only near the walls where the velocity gradients are very steep. A maximum error of about 8% occurs in the first time step. This error decreases with each time step and the steady-state results exhibit high accuracy. These trends are confirmed in Figure 5.15, which illustrates that the average u-velocity error within the domain decreases to below about 0.05% at the steady-state.

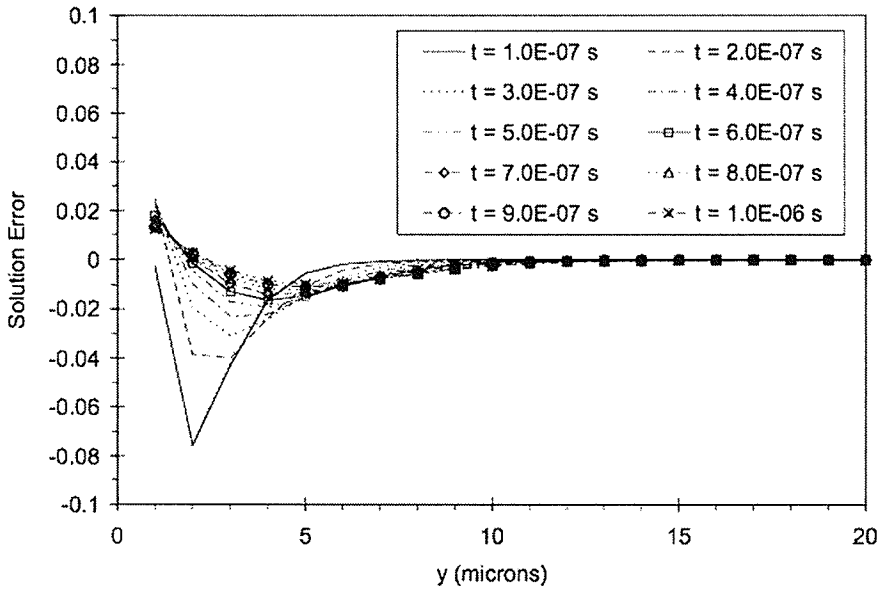

Figure 5.14: Solution Error of Predicted Transient Velocity Profiles.

The steady-state centerline velocity may be calculated in the following manner,

$$u_c = -\frac{d^2}{8\mu}\frac{\partial P}{\partial x} \tag{5.11}$$

which yields a centerline velocity of 3.75 mm/s. This implies that it would take about 8 ms for the fluid to traverse the entire domain. Additional sensitivity results are presented in Table 5.2, where the errors have been calculated according to Eq. (5.10). Solution errors are summarized for 20 × 20 and 20 × 80 mesh simulations. In both cases, the percentage error was less than about 1% at different locations within the microchannel, so grid-independent results could be confidently obtained with the 20 × 20 mesh discretization.

In addition to this analytical solution for transient Poiseuille flow, the numer-

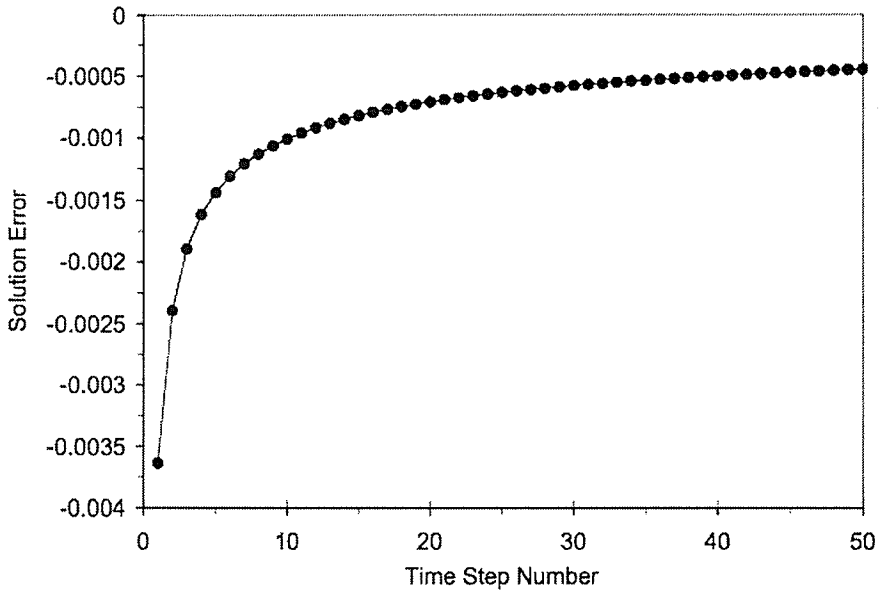

Figure 5.15: Spatially Averaged Error of Predicted Velocity.

ical model is comapred against experimental examinations of TCP in open-ended microchannels in the following section.

Table 5.2: Percentage Error for Grid Refinement Study ($t = 0.005$ ms)

% Error	20 × 20 mesh	20 × 80 mesh
$y = 3.75$ mm	0.1352	-2.04×10^{-3}
$y = 7.5$ mm	-0.16	-6.42×10^{-3}
$y = 11.25$ mm	-0.0118	-6.36×10^{-3}
$y = 15$ mm	-0.0011	-3.36×10^{-3}

5.4 TCP in an Open-End Microchannel

Sammarco and Burns [49] used TCP to move nanoliter- and picoliter-sized droplets of liquid within microfabricated flow channels. The authors presented the following equation for the steady-state TCP velocity for a droplet,

$$v = \frac{dGB\cos\theta_R}{LS\mu}(\Delta T - \Delta T_{\min}) + \frac{d^2}{S\mu L}(\Delta P_e + \rho g L \sin\phi) \tag{5.12}$$

where

$$\Delta T = T_R - T_A \tag{5.13}$$

and

$$\Delta T_{\min} = \left(\frac{A}{B} - T_A\right)\left(1 - \frac{\cos\theta_A}{\cos\theta_R}\right) \tag{5.14}$$

The variables G, d, A and B, along with the subscripts A and R were introduced in section 1.3. The variables L, S, $\Delta T_{\min}$, ΔP_e and ϕ are the length of the microdroplet, a geometry-specific constant, the minimum temperature difference across the droplet to overcome surface tension hysteresis, the external (air) pressure difference across the microdroplet and the inclination angle of the microchannel. For the case of an open-ended microchannel, the external pressures are assumed equal and the microchannel is not assumed to be inclined.

The microchannels were etched into 500 μm thick Corning glass No. 7740 wafers using an HNO_3:HF [3:7] etching solution, yielding microchannels of trapezoidal cross-section. A series of poly-silicon resistive heating elements beneath the microchannels were used to control the droplet motion, while a separate series of poly-silicon resistive temperature detectors were used to measure the temperature field within the

Table 5.3: Parameters for Open-Ended TCP Experiments with Mineral Oil.

Property	Value
Channel Height (d)	32 μm
Chanel Depth (b)	500 μm
Droplet Length (L)	5726 μm
Receding Contact Angle (θ_R)	47.6°
Advancing Contact Angle (θ_A)	49.8°
Minimum Temperature Difference (ΔT_{min})	19°C
Geometry-Specific Constant (S)	37
Viscosity (μ)	26×10^{-9} Ns/m^2

microdroplet. The experimental parameters of Ref. [49] may be found in Table 5.3. The value of $T_{\text{min}} = 19°\text{C}$ and $S = 37$ that were used in the numerical simulations were determined experimentally [49]. These values were determined from experimental data based on comparisons with data in Fig 5.16. Although a value of $T_{\text{min}} = 24°\text{C}$ appears to better match the experimental data, existing values from Ref. [49] will be adapted in this section.

The microchannels manufactured for this thesis are formed by reactive ion etching and they have a rectangular cross section. Slit-like microchannels have an S value of approximately 12, making comparisons with the data of Figure 5.16 difficult. The theoretical value of S for the trapezoidal microchannels of Ref. [49] was determined by comparisons with values of the Poiseuille number, P_0, calculated for similar microchannels of other authors. Richter et. al. [56] reported that the geometry coefficient C_R can be derived from the Poiseuille Number as follows,

$$C_R = \frac{U^2}{8A} P_0 \tag{5.15}$$

where U is the wetted perimeter and A is the cross sectional area of the microchannel. The value of C_R may be calculated according to

$$C_R = \frac{12 - 1.38a + 4a^2}{a - 0.85a^2 + 0.28a^3} \tag{5.16}$$

where

$$a = \frac{\text{height}}{\text{average width}} \tag{5.17}$$

A channel height of 32 microns and an average channel width of 500 microns yield $a = 0.064$, so Eq. (5.16) yields a geometry coefficient of $C_R = 196.864$. Rearranging Eq. (5.15) and solving for the Poiseuille number yields $P_0 = 22.258$. Urbanek et. al. [57] reported a Poiseuille number of $P_0 = 22.94$ for a trapezoidal microchannel with a height/width ratio of $a = 0.0277$. They wrote the Poiseuille number in terms of experimental quantities,

$$P_{0,\text{exp}} = \frac{AD_h^2 \Delta P}{2\mu QL} \tag{5.18}$$

Noting that the bulk droplet velocity may be expressed as $u_b = Q/A$, we may rearrange Eq. (5.18) as follows,

$$u_b = \frac{D_h^2 \Delta P}{2\mu L P_{0,\text{exp}}} \tag{5.19}$$

The value of S for the trapezoidal microchannels of Ref. [49] is determined by comparing Eq. (5.19) with the value predicted by Sammarco and Burns [49],

$$u_b = \frac{D^2 \Delta P}{S\mu L} \tag{5.20}$$

Equating Eqs. (5.19) and (5.20), the value of S for the parameters shown in table 5.3 is $S = 12.6$. This is inconsistent with the value reported by Sammarco and Burns of

$S = 37$ [49]. It is possible that their microchannel was not a perfect trapezoid, due to manufacturing limitations. The scaling factor $S_{\text{Num}}/S_{\text{Exp}}$ used to compare numerical and experimetal data in Figure 5.16 was chosen to be $12/37 = 0.32432$.

TCP in open-ended microchannels was simulated for a variety of fixed temperature differences of ΔT = 8°C, 10°C, 11°C, 16°C, 21°C, 36°C and 51°C in a rectangular microchannel (see table 5.3 for simulation parameters). Equation (5.14) suggests $\Delta T_{\text{min}} = 7.88$°C. The steady-state bulk microdroplet velocities corresponding to this minimum temperature difference are labeled as "Numerical (FVM)" in Figure 5.16. The curve representing the theoretical steady-state bulk microdroplet velocities is labeled as "Theory ($S = 37$)" in Figure 5.16. The slopes of the curves are identical, but the minimum temperature differences required to overcome surface tension hysteresis (corresponding to the intersections of the curves with the x-axis) differ by approximately 2 degrees. It is unclear why the "theory" line of Sammarco and Burns [49] does not coincide with the value of ΔT_{min} suggested by Eq. (5.14). It should be noted that the dashed lines represent the uncertainty of the experimental parameters.

Examination of Figure 5.16 reveals that the experimental velocities do not agree with values predicted by Eq. (5.12). Sammarco and Burns [49] reported that the error may lie with the measurment of the advancing and receding contact angles. They mentioned that a difference as slight as having $\theta_A \approx 50 \rightarrow 52°$ and $\theta_R \approx 48 \rightarrow 47°$ (limits of uncertainty) would shift ΔT_{min} from approximately 7°C to 18°C [49]. Unfortunately, predictions are highly sensitive to parameters that have difficulties of measuring and confirming accurately.

In order to compare the simulated data with the experimental data with $\Delta T_{\text{min}} =$ 19°C, the simulated data was shifted by $T_{\text{min}} = 19$°C $- 7.88$°C $= 11.12$°C along

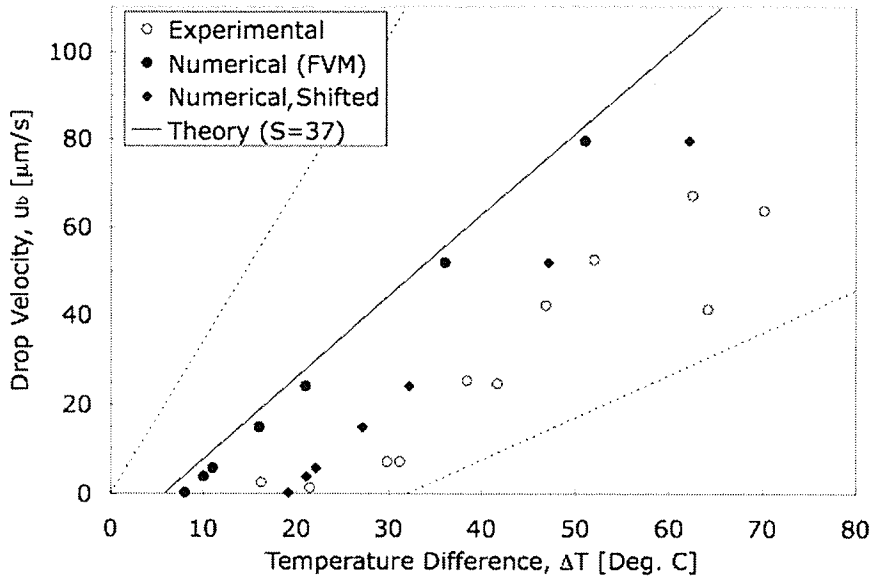

Figure 5.16: Comparison of Experimental and Numerical Predictions of Steady-State TCP-Driven Droplet Velocities for Mineral Oil in Open-Ended Microchannels.

the x-axis. The resulting steady-state bulk microdroplet velocities are labeled as "Numerical, Shifted" in Figure 5.16. The shifted velocities show excellent agreement with the experimentally determined values of Sammarco and Burns [49]. The shifting to represent the effect of surface tension hysteresis could be readily incorporated into the numerical simulations if the values of θ_A and θ_R were known, such as this case when experimental data exists.

Excellent agreement with the exerimental results above suggest that the numerical formulation can accurately predict thermocapillary pumping, given a fixed temperature difference across the droplet in an open-ended microchannel. Additional validation was performed by comparing simulated results against experimental data of Sammarco and Burns [49] for mineral oil droplets pumped through rectangular

microchannels against an applied external pressure. Droplets of length 2.5 mm, 12.8 mm and 21 mm were considered. The theoretical line in Figure 5.17 is defined by

$$\frac{v}{d/L} = \left(\frac{d}{S\mu}\right)\Delta P_e - \frac{\Delta T_{\min} Gb\cos\theta_R}{S\mu} \tag{5.21}$$

It was derived by dividing Eq. (5.12) by d/L and setting both ϕ and ΔT to zero. The velocities of the numerical simulations in Figure 5.17 were reduced by 2.28 cm/s to account for surface tension hysteresis, through the second term of Eq. (5.21). The dashed lines represent the range of uncertainty in the theorectical line of Sammarco and Burns [49] due to experimental parameters. Sammarco and Burns [49] also note that the microchannels were not perfectly rectangular, so the value of $S = 12$ yielded slightly poorer agreement with experimental data than actually exists. It is again unclear why the theory line does not coincide with data of Sammarco and Burns [49]. The slope of the theory curve closely matches the experimental data, although the velocity appears to increase slightly slower than predicted results when the driving pressure is increased. This could occur because the dynamic contact angles vary with velocity. It is again possible that the error in contact angle measurement is responsible for the deviation of experimental velocities from their theoretical values.

Section 5.3 presented validations of various portions of the finite volume method. Both transient heat transfer and fluid flow were examined. The full solution of cyclic thermocapillary pumping in closed-end microchannels will be studied in the next section. The complexity of the composite domain and the thermal bridge make an analytical solution difficult. In addition, there exists no solution to this problem in the archival literature (to my knowledge).

Table 5.4: Parameters for Open-Ended Pumping Experiments with Mineral Oil and an Externally Applied Pressure.

Property	Value
Channel Height (d)	50 μm
Chanel Depth (b)	500 μm
Droplet Length (L)	2.5 / 12.8 / 21 mm
Receding Contact Angle (θ_R)	39.6°
Advancing Contact Angle (θ_A)	50.6°
Surface Tension Hystersis Correction	2.28 cm/s
Geometry-Specific Constant (S)	12
Viscosity (μ)	26×10^{-9} Ns/m^2

5.5 Cyclic TCP in a Closed-End Microchannel

Unlike past studies of thermocapillary pumping in open microchannels, droplet transport in a closed microchannel is considerably different, as the adjoining pressures around the droplet are unequal. Large droplet velocities reported previously in open microchannels are not attainable, since smaller droplet displacements create adverse external pressures with a similar magnitude as the thermocapillary pressure. Also, past assumptions of steady-state Poiseuille flow become unrealistic, when the droplet is accelerating / decelerating and the heat source is cycled on / off.

Various practical applications besides micro heat engines may require a periodic cycling of droplet motion within a microdevice, rather than a uniform cycle. In such cases, the periods of heating / cooling could be manipulated to establish precise control of droplet displacement. The following results of droplet transport could be used for such purposes. Some examples include matching a resonance frequency or pressure requirement for a thermal switch, optical switch or micro-valve. For instance,

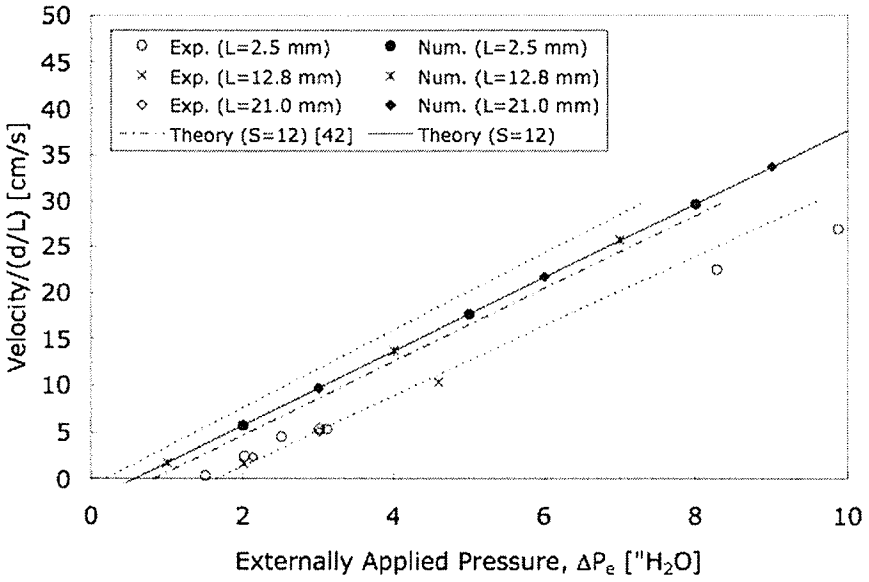

Figure 5.17: Comparison of Experimental and Numerical Predictions of Steady-State Pressure-Driven Droplet Velocities for Mineral Oil in Open-Ended Microchannels.

the moving micro-droplet could re-direct a light beam by reflection to a different path in optical fiber applications [37]. Thermocapillary pumping of the micro-droplet could facilitate an optical "switch" by re-directing light from one fiber to another fiber through this micro-droplet reflection. For such innovative applications and others, the following results will provide useful new insight regarding thermocapillary forces and droplet transport in closed microchannels.

Simulation results for the theoretical model and finite-volume method were compared to provide further validation for each of the models. In order to facilitate meaningful comparisons, the heat source in the FVM was modified to span the entire height of the domain and it remains aligned with the left edge of the droplet. The parameters of the simulations may be found in Table 5.5.

Table 5.5: Simulation Parameters for Validating Semi-Infinite Solid Assumption.

Property	Units	Value
Density of Droplet	kg/m^3	998.0
Thermal Conductivity of Droplet	W/mK	0.606
Specific Heat of Droplet	J/kgK	4181.0
Kinematic Visocity of Droplet	Ns/m^2	595×10^{-6}
Density of Air	kg/m^3	1.1614
Thermal Conductivity of Air	W/mK	0.0623
Specific Heat of Air	J/kgK	1007.0
Density of Substrate	kg/m^3	2500.0
Thermal Conductivity of Substrate	W/mK	0.96
Specific Heat of Substrate	J/kgK	837.0
Channel Length	m	2000×10^{-6}
Channel Height	m	2×10^{-6}
Channel Depth	m	100×10^{-6}
Heat Flux	W/m^2	5×10^6

The temperatures predicted from the theoretical model are plotted against values of the FVM solution in Figure 5.18. The curve labeled Dirichlet condition corresponds to the case for which the bottom surface of the substrate was maintained at a temperature of $T = 20°C$, while the curve labeled Neumann condition corresponds to the case where the bottom surface of the substrate was insulated. The Figure indicates that approximations of the specific heats in the composite regions of the theoretical model result in fairly accurate predictions of the thermocapillary temperature, except near the end of the heating period. At that point, the droplet has moved past the heat source and the heat source is removed. The thermocapillary force (resulting from the capillary pressure) drops rapidly, while the compressed air continues to exert resistance to droplet motion. Some of the errors in the capillary pressure occur from i) treating the solid and fluid regions as one region with uniform properties, ii) neglecting heat transfer to the surroundings, iii) neglecting convection in the droplet and iv) assuming that the right temperature of the droplet remains constant. These simplifications lead to small discrepancies between numerical and theoretical results.

During the heating period, close agreement between theoretical (SA Model) and numerical FVM predictions of the external pressure difference across the droplet is observed in Figure 5.19. Thermocapillary forces are offset by the opposing air pressure (compressed and expanded gas phases at the right and left ends of the closed microchannel, respectively) and frictional resistance along the walls of the microchannel. These combined forces and internal inertia within the droplet lead to a nearly linearly decreasing pressure difference across the micro-droplet in Figure 5.19. This magnitude of the pressure difference increases more slowly during early times, as the heat input requires a certain amount of time to heat the receding end

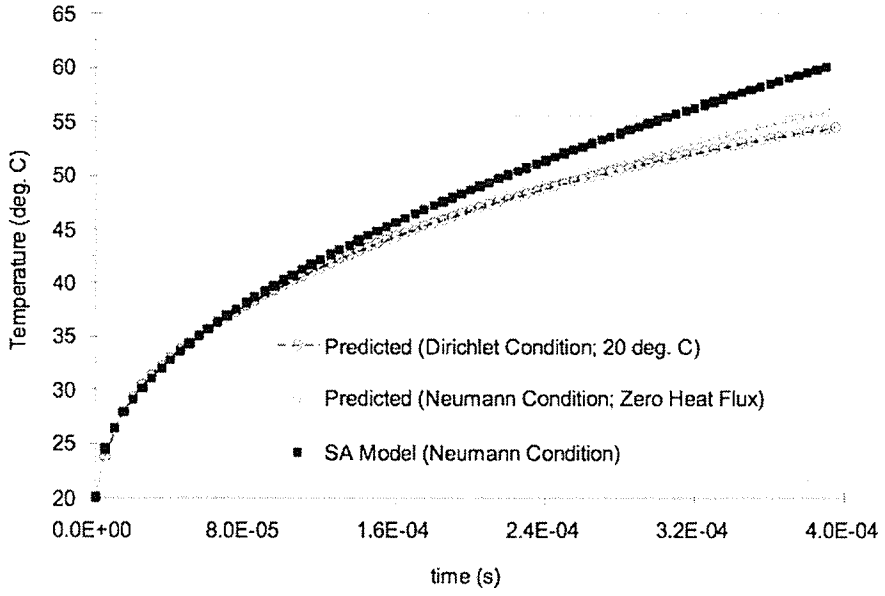

Figure 5.18: Comparison of Theoretical and FVM Predictions of the Temperature of the Receding Edge of the Droplet During Heating.

of the micro-droplet, causing the droplet to accelerate.

In Figure 5.20, numerical predictions of the bulk droplet velocity show reasonably close agreement between the two models. The theoretical model agrees well with numerical simulations at early times. But droplet velocities are over-predicted by the SA Model at later times, as lateral heat flow through the substrate is neglected. Additionally, the temperature along the right meniscus of the droplet is assumed to remain at 20°C. As a result, the thermocapillary force on the droplet is over-predicted. A partial heating / cooling cycle is illustrated in Figure 5.20. The droplet velocity increases when the heat source is located near the back edge of the droplet (heating period). But it decreases when the droplet has moved past the heat source (cooling period), when the opposing pressure of the compressed air and friction produce a net force against the direction of droplet motion. Unlike past studies with a moving heat

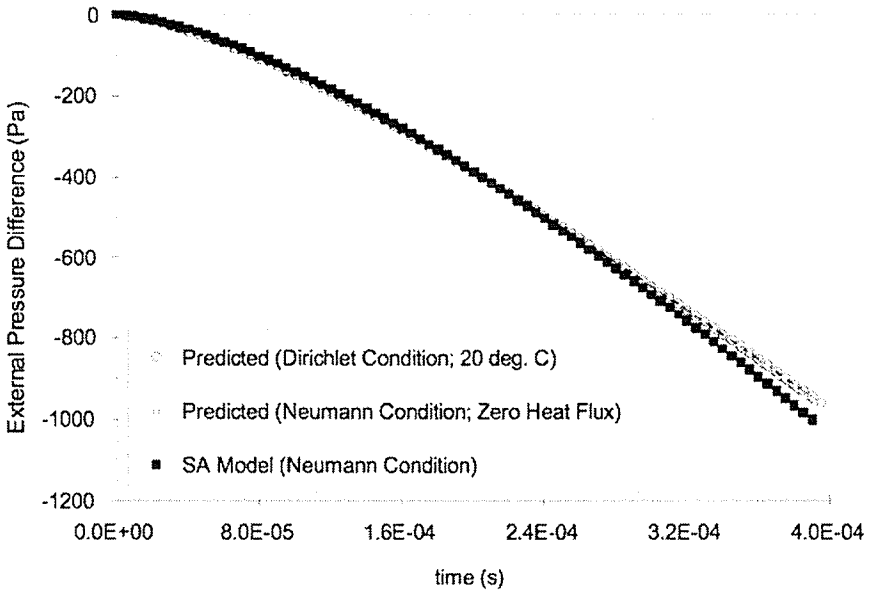

Figure 5.19: Comparison of Theoretical and FVM Predictions of External Pressure During Heating.

source at the back edge of the droplet, the current results indicate that thermocapillary pumping can be sustained with a stationary heat source. But cycling of the heat source is needed for continuous operation. The droplet returns back to its initial position when the opposing pressure of the compressed air phase and friction produce a net leftward force on the micro-droplet. The heat source is turned off during this leftward motion. Otherwise, the gas pressure could not overcome the thermocapillary resistance in the direction of droplet motion.

The simplifications made in the theoretical model lead to slight discrepancies in temperature, as seen in Figure 5.18. The effect of these assumptions on the droplet displacement may be seen in Figure 5.21, which plots the droplet displacements predicted by the theoretical and FVM simulations. The theoretical model over-predicts the droplet displacement by approximately 4 percent due to over-prediction of the

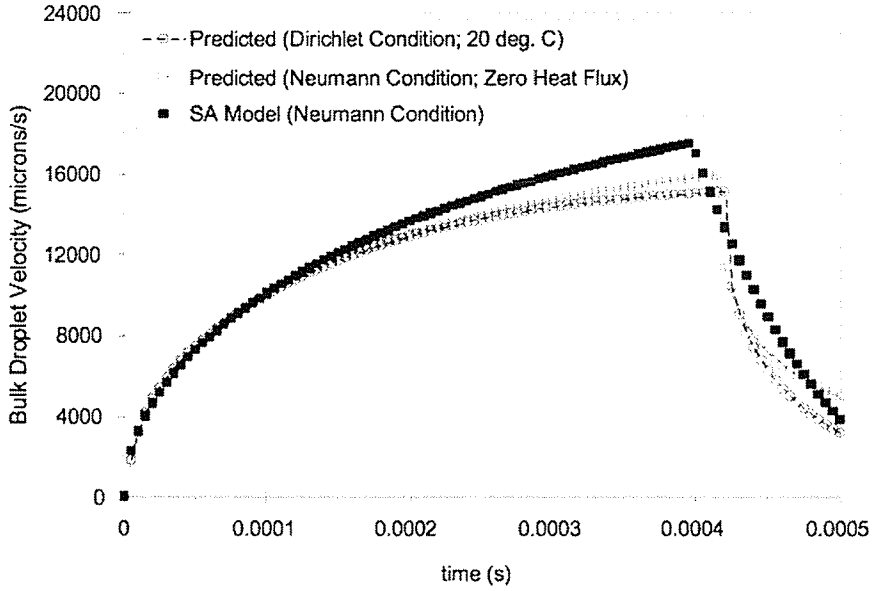

Figure 5.20: Comparison of the Theoretical and FVM Predictions of Bulk Droplet Velocity During Heating.

droplet's left temperature and the neglected rise in the droplets right temperature. Nevertheless, the droplet displacements predicted by both models show good agreement during heating.

Figure 5.22 compares the droplet displacements predicted by the theoretical and FVM models after the droplet had reached a displacement of five microns in the FVM. At this time, the heat source was removed and the cooling algorithm of each model was initiated. Figure 5.22 indicates that the theoretical model's approximation of the cooling curve leads to reasonable predictions of the droplet displacement, as the droplet returns towards its equilibrium position. During the cooling period, the right gas expands when the droplet moves leftwards. The heat source is turned off during this period. Otherwise, the gas pressure would be insufficient to overcome thermocapillary forces in a heated region near the thermal bridge.

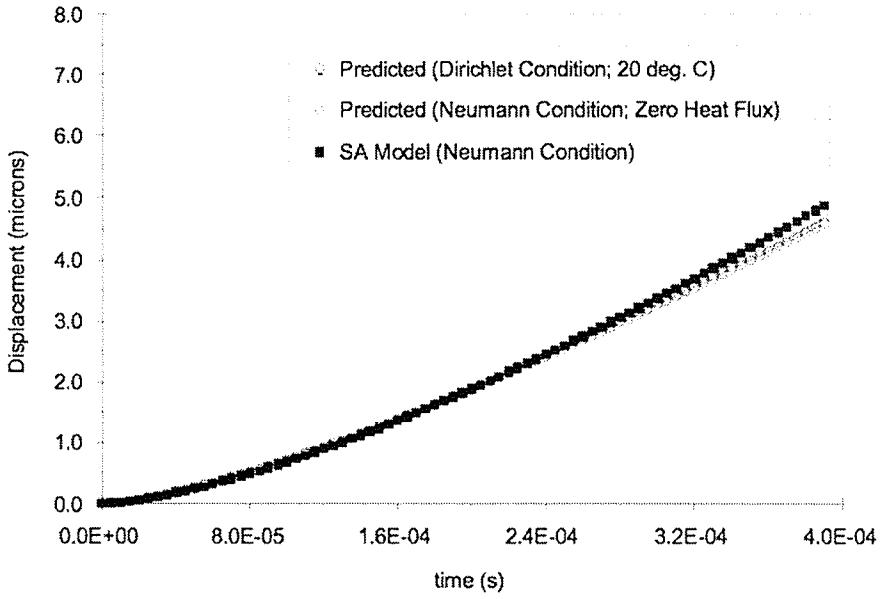

Figure 5.21: Comparison of the Theoretical and FVM Predictions of Droplet Displacement During Heating.

The droplet dynamics predicted by each of the models has been compared and shown to have relatively good agreement. Simplifications in the heat transfer analysis of the theoretical model yielded errors in the temperature field, which adversely affected the microdroplet dynamics. The trends, however, agreed well and they indicate that the FVM accurately predicts the physics of thermocapillary pumping in closed-end microchannels. A more detailed analysis of the FVM is presented in Section 5.6.

5.6 Detailed Examination of FVM Simulations

This chapter has thus far been devoted to the validation of both the theoretical and numerical models. The theoretical model may be used to predict how changes

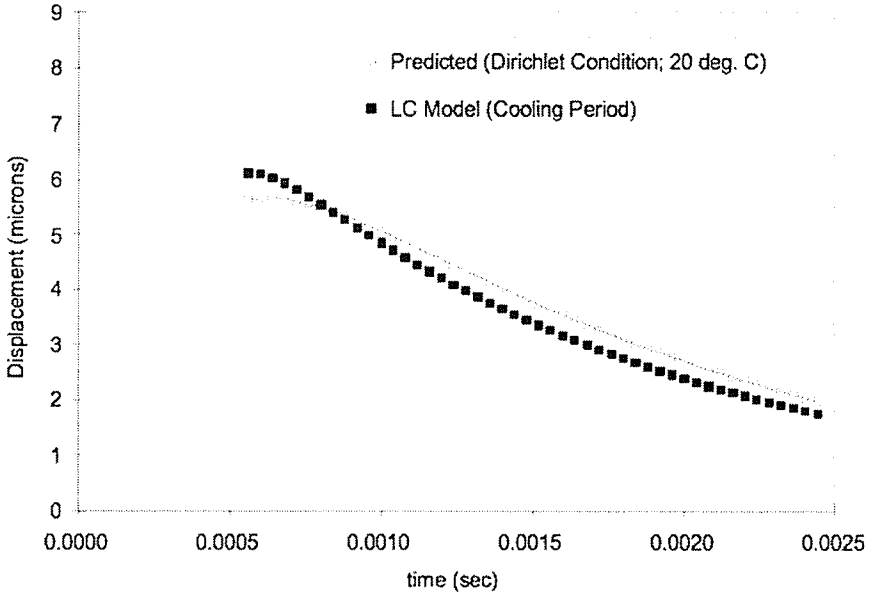

Figure 5.22: Comparison of Theoretical and FVM Predictions of Droplet Displacement During Cooling.

in simulation parameters will affect thermocapillary pumping. It provided useful validation of the numerical method. The following detailed analysis of the FVM will ultimately be used to design the micro heat engines discussed in Chapter 2.

5.6.1 Conjugate Boundary Conditions

Moving the temperature boundary conditions away from the substrate / droplet interface allows known boundary conditions to be applied at the interface between the substrate and its surroundings. Heat addition to the droplet still occurs at the substrate / droplet interface, but it must be predicted by the finite volume method (FVM) without "internal" boundary conditions. This section describes how the method predicts heat transfer between the different phases.

Conduction in the substrate matches convection in the fluid along the solid / fluid interface. Along a phase interface, heat transferred from phase 1 (I) flows into phase 2 (II), i.e.,

$$\left(k\frac{\partial T}{\partial x_i}\right)_I = \left(k\frac{\partial T}{\partial x_i}\right)_{II} \tag{5.22}$$

Discretization of Eq. (5.22) must eventually be written in terms of nodal temperatures. All temperatures are stored at nodal points, which are centrally located within the control volumes. Full-width control volumes do not provide a temperature value at the solid / fluid interface, where there is a discontinuity in the spatial temperature gradient, due to a step change in thermophysical properties. A weighting scheme can be used to estimate the interface temperatures, when generating the coefficient matrices for the energy equation.

Alternatively, this thesis uses zero-width control volumes (10^{-32} m thickness in the numerical model) along the conjugate phase boundaries. These zero-width control volumes successfully enforce Eq. (5.22) without receiving any special attention at the substrate / droplet, substrate / air, or droplet / air interfaces, when generating the coefficient matrices of the energy equation. The energy balance for the P control volume at the solid/fluid interface becomes

$$k_S\frac{T_P - T_S}{(\Delta y)_s} = k_N\frac{T_N - T_P}{(\Delta y)_n} \tag{5.23}$$

Although temperatures within each region are solved simultaneously with the same coefficient matrices, each region receives slightly different treatment when generating the coefficient matrices. Heat transfer within the air regions adjacent to the droplet (see Figure 2.2) is governed by convection, while the Navier-Stokes equations are

solved within the moving micro-droplet. The air velocities are approximated to vary linearly from zero at the lateral walls to the bulk droplet velocity at the droplet / air interface. These velocity fields coincide with values at the lateral control volume faces within the air regions. The lengths of the left and right air regions stretch and shrink, respectively, as the droplet translates from left to right, while the Bernstein polynomial coefficients to generate the meshes remain constant. Any air flowing out of a control volume within a time step is "recovered" by the control volume when the mesh is re-generated. There is effectively no flow across the lateral faces of the air control volumes. Thus, convection terms were not included in the energy equations of the air regions.

The droplet region of the temperature mesh is moving through the domain at the droplet's bulk velocity. The velocity field within the droplet is solved on a separate mesh in the reference plane of the overall stationary system. It cannot be used directly in the energy equation for the droplet region, without modification. For reasons described previously for the air region, the droplet's velocity field must be considered in the droplet's reference frame, when determining advecting velocities in the energy equation. The droplet's bulk velocity is subtracted from the droplet's velocity field before calculating the advection terms. In the reference frame of the channel, the velocity field resembles a developing channel flow. When viewed in the droplet's reference frame, a re-circulating velocity field is observed. This re-circulation yields zero net mass flow in the x-direction.

Additional numerical simulations were conducted to investigate the detailed mechanisms of interfacial heat transfer within the microchannel. Only the bottom half of the symmetric domain was considered. A non-uniform Bezier mesh was used to in-

crease mesh densities along the fluid phase boundaries. Figure 5.23 shows a plot of the temperature profiles along the solid / fluid interface at various times. For each curve (time step), the symbol corresponding to the left air / fluid interface is drawn at half scale. The droplet reached a displacement of five microns after 1.865 ms, at which time the heat source was removed. All curves with white symbols represent time steps before the heat source was removed, while those with black symbols represent time steps after the heat source was removed. Heat flows from the droplet to the left air region for only the first time shown, when $t = 0.5$ ms. This observation is marked by a positive temperature gradient on the curve for $t = 0.5$ ms. Notice that the white square to the left of the small white interface square has a lower temperature.

For later time steps, Figure 5.23 shows heat flowing from the air to the droplet. As the droplet moves away from the heat source, a portion of the adjacent advancing air region will move over the heat source. The air heats up rapidly because the substrate onto which the air is expanding has a high temperature and the air has a much larger thermal diffusivity than the droplet ($\alpha = 2.2488 \times 10^{-5}$ m^2/s for air versus $\alpha = 1.4523 \times 10^{-7}$ m^2/s for water). These results would not be observed in open-ended microchannels of past studies, where the heat source was located along the substrate / fluid interface and assumed to remain aligned with the receeding edge of the droplet.

Figure 5.24 shows a plot of the vertical heat flux across the substrate / droplet interface at a time of $t = 1.5$ ms. A large positive heat flux exists directly above the thermal bridge. Immediately to the right of the thermal bridge, however, the heat flux is negative. In this region, heat is flowing "over" the insulation to the cooler substrate region, as illustrated in Figure 5.25. Further right of the heat source,

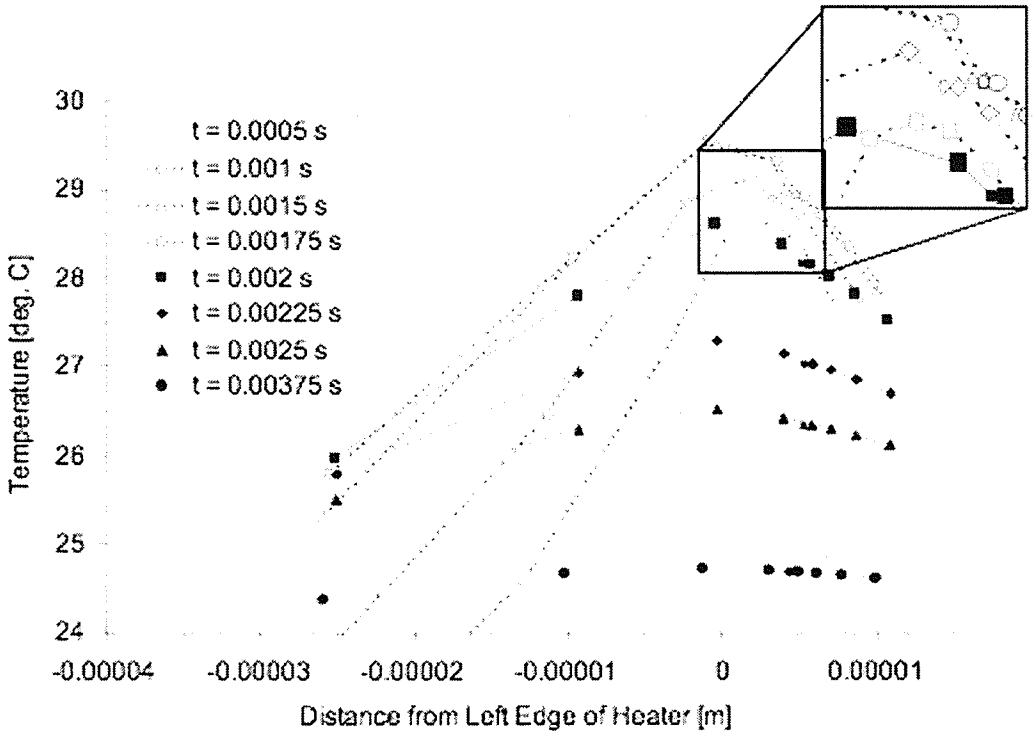

Figure 5.23: Temperature Profiles along the Substrate / Fluid Interface at Various Time Steps.

the heat flux again becomes positive. Heat conduction through the substrate (which scales horizontally with $k\Delta y/\Delta x$ and vertically with $k\Delta x/\Delta y$) is orders of magnitude larger than convection to the surroundings (which scales with $h\Delta x$). The substrate / surroundings interface resembles an insulated surface. Heat flows horizontally more readily through the substrate than the droplet, due to the higher thermal conductivity of the substrate. The higher thermal diffusivity of the substrate also means that it will heat up more than the droplet, given the same heat input. As a result, the substrate will heat up faster than the droplet, resulting in the positive heat flux of Figure 5.24. It should be noted that the temperature of the substrate does not

significantly exceed the droplet temperature at any x-position, due to the small height of the domain. The magnitude of the heat flux decreases, further away from the heat source due to decreasing temperatures, and thus decreasing temperature differences, across the substrate / droplet interface.

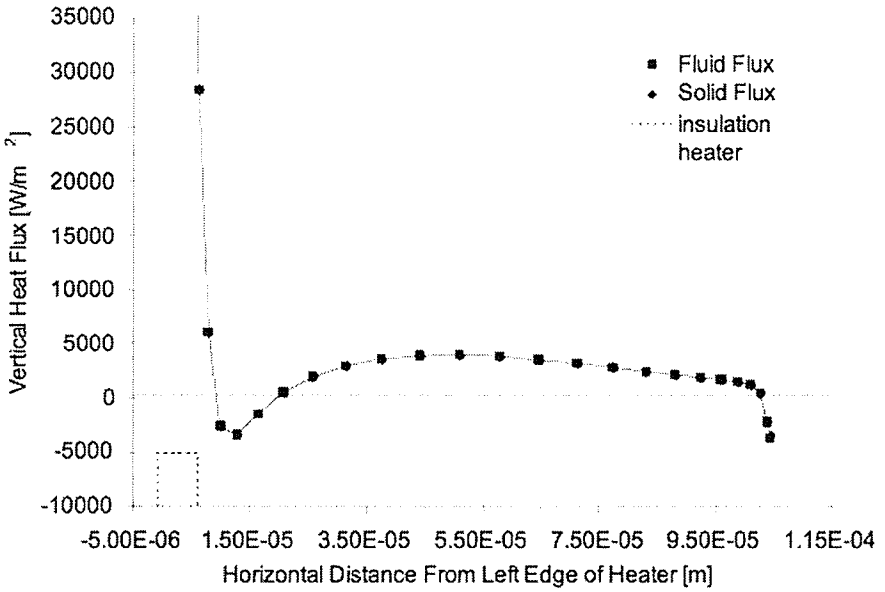

Figure 5.24: Heat Flux across the Substrate / Droplet Interface at time $t = 0.015$ ms.

The air to the right of the droplet causes a change in the aforementioned trend. Although the horizontal heat flux through the substrate is approximately fifty times greater than the value across the droplet / right air interface, the air has a higher thermal diffusivity than silicon (approximately thirty times larger). Thus, the air attains a higher temperature than the silicon, resulting in heat transfer from the air to the substrate. This leads to a negative flux across the substrate / fluid interface, as seen in the right portion of Figure 5.24.

Figure 5.26 shows the horizontal heat flux across the left air / droplet interface at

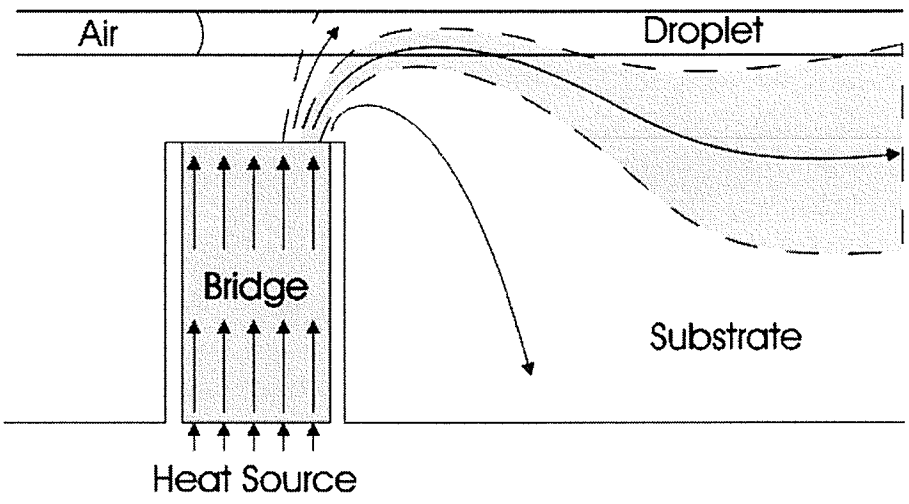

Figure 5.25: Illustration of Heat Flow Lanes.

time $t = 0.015$ ms. The air flux was calculated as

$$q"_{i,j} = -k_{\text{air}} \left(\frac{T_{i,j} - T_{i-1,j}}{x_i - xi - 1} \right) \tag{5.24}$$

where the subscript i refers to the interface and the subscript i-1 refers to the air control volume immediately to the left of the interface. The droplet flux was calculated as

$$q"_{i,j} = -k_{\text{droplet}} \left(\frac{T_{i+1,j} - T_{i,j}}{x_{i+1} - xi} \right) \tag{5.25}$$

where the subscript i refers to the interface and the subscript i+1 refers to the droplet control volume immediately to the right of the interface. The plot shows no visible difference between the two fluxes, which indicates that Eq. (5.22) is satisfied.

Figure 5.27a plots isolines of temperature in the vicinity of the thermal bridge. The isolines clearly show heat flowing "over" the insulation to the right of the thermal bridge. The plot suggests that the heat flow to the right side of the thermal bridge

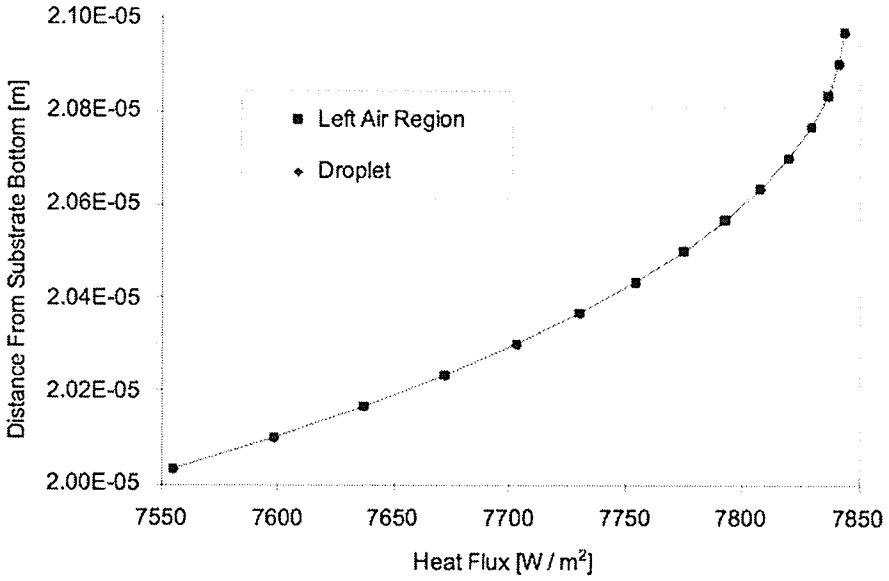

Figure 5.26: Heat Flux across Left Air / Droplet Interface at time $t = 0.015$ ms.

exceeds the value to the left of the thermal bridge. The contour plot, however, interpolates the supplied data onto a rectangular grid before plotting. Note that very steep temperature gradients exist across the insulation, beside the thermal bridge. As a result, the isolines change dramatically as nodal points move from one composite material to another. The isolines indicate a positive vertical heat flux across the left-most end of the droplet. This heat flux reverses direction at approximately x = 960 microns. Figure 5.27b plots isolines over the entire length of the droplet. It can be observed that, the right-most isoline within the droplet indicates a positive vertical heat flux, while the isolines to the right side of the droplet clearly indicate a negative vertical heat flux, as discussed with reference to Figure 5.23. Figure 5.27c shows isolines of temperature surrounding the thermal bridge. The nearly vertical isolines indicate that the heat transfer is nearly one-dimensional. Furthermore, the

temperature field is relatively uniform on both sides of the thermal bridge. Although the effective thermal conductivity of the composite is higher on the right side of the thermal bridge (1.343 W/mK for the substrate / droplet composite versus 1.316 W/mK for the substrate / air composite), the effective thermal diffusivity of the composite is higher on the left side of the thermal bridge (7.416×10^{-7} m^2/s for the substrate / air composite versus 6.809×10^{-7} m^2/s for the substrate / droplet composite).

It has been shown that the conjugate boundary conditions yield reasonable heat fluxes across phase boundaries. The following section examines the effect of the adaptive grid forumlation on the dynamics of thermocapillary puming.

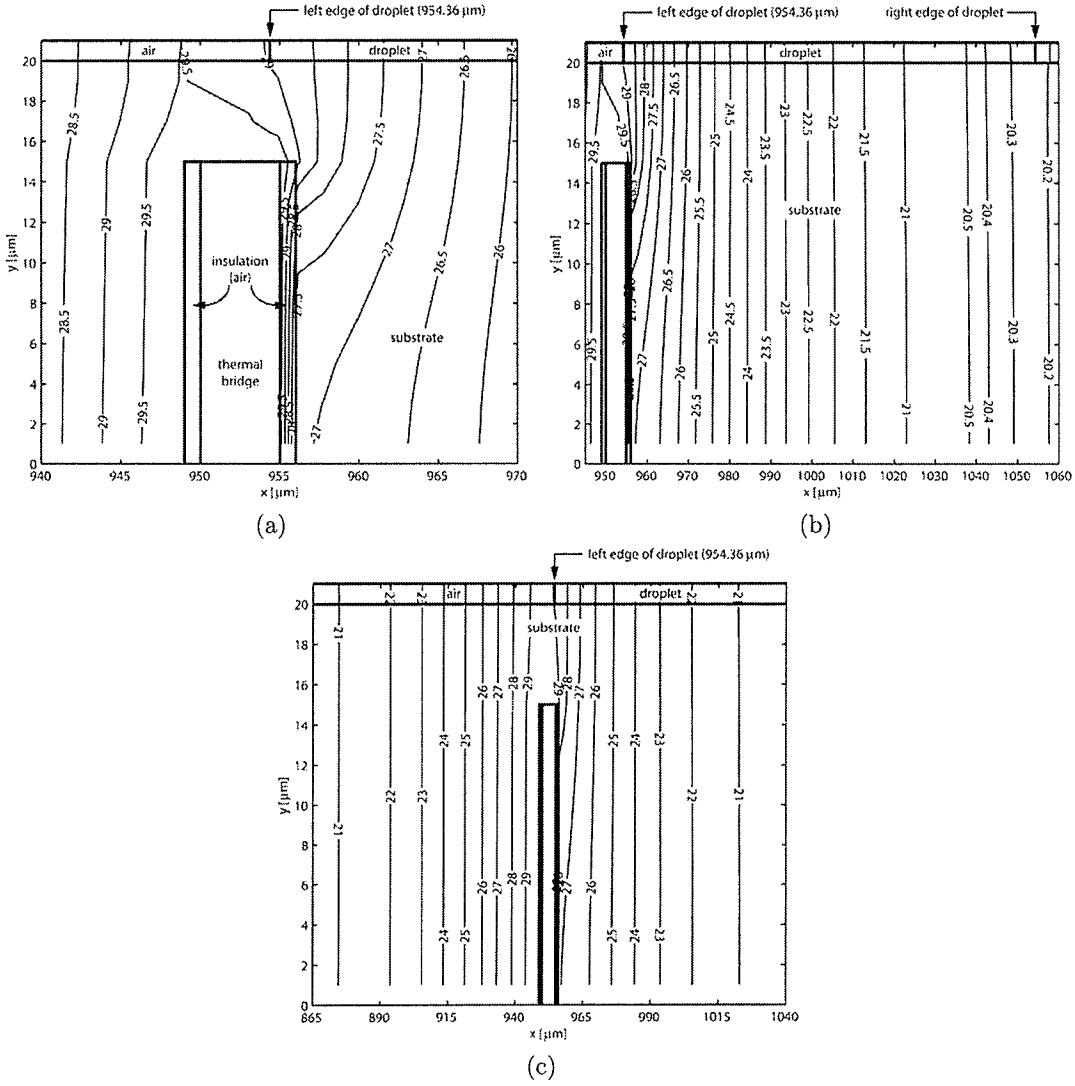

Figure 5.27: Isolines of Temperature at Time $t = 0.015$ ms: a) in the Vicinity of the Thermal Bridge, b) Around the Microdroplet and c) Surrounding the Thermal Bridge.

5.6.2 Effect of Adaptive Grid Formulation on TCP

The adaptive grid formulation was developed to permit separate solution domains for the droplet (momentum equation) and entire domain (temperature equation). This section examines how the adaptive grid, particularly in the vicinity of the thermal bridge, affects the droplet dynamics during thermocapillary pumping in closed-end microchannels.

Figure 5.28 shows the displacement and droplet corner temperatures for a portion of a heating cycle for the droplet. The heat source is removed when the droplet has been displaced by five microns. At this time, the left corner temperature immediately begins falling, while the right temperature continues to increase, due to convection through the droplet and conduction through the substrate. This leads to a lower thermocapillary driving force, so the droplet begins decelerating. It takes an additional 0.4 milliseconds before the droplet changes direction, during which time the droplet travels an additional 0.23 microns.

Oscillatory behavior of the left corner temperature can be observed at approximately 0.75 milliseconds. This result occurs from rapid changes in temperature of nodal points passing between the silicon and thermal bridge regions. Large artificial heat fluxes arise between nodal points surrounding the boundary of the thermal bridge, due to rapidly changing temperatures and thermophysical properties of translating control volumes near the thermal bridge.

Figure 5.29 compares the temperature profiles at the left end of the droplet for a variety of grid discretizations. Changing the grid spacing alters the time at which control volumes cross the boundary of the thermal bridge. Although increasingly refined grids capture the changes of thermophysical properties more accurately, smaller grid

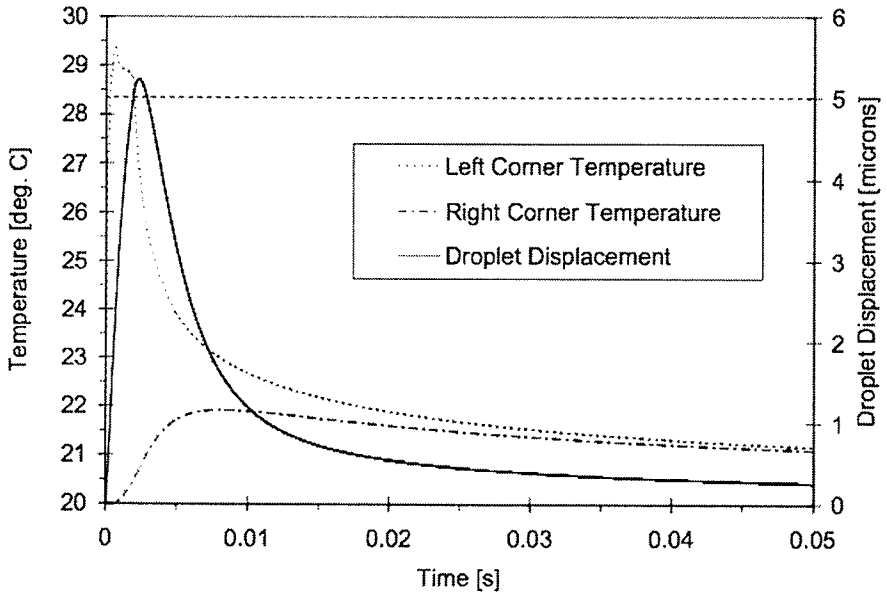

Figure 5.28: Transient Droplet Corner Temperatures and Associated Droplet Displacement.

spacing leads to more and larger artificial heat fluxes caused by these rapidly changing conditions. The line labeled "linear interpolation" corresponds to a case where linear interpolation, rather than Eq. (4.33), was used to update the temperature field near the thermal bridge. This temperature profile does not exhibit the rapid oscillations observed in other cases of Figure 5.29. Also, Figure 5.29 shows a comparison with a temperature profile corresponding to a case where the thermal bridge was removed from the silicon substrate. It can be observed that the rise of droplet temperature is significantly delayed, when lateral heat transfer is not discouraged.

Figure 5.30 shows the early trends of droplet displacement for various grids compared in Figure 5.29. It can be observed that the grid spacing has little effect on the predicted displacement of the droplet. Additionally, the temperature oscillations do not seem to have adverse effects on predictions of the droplet displacement. Without

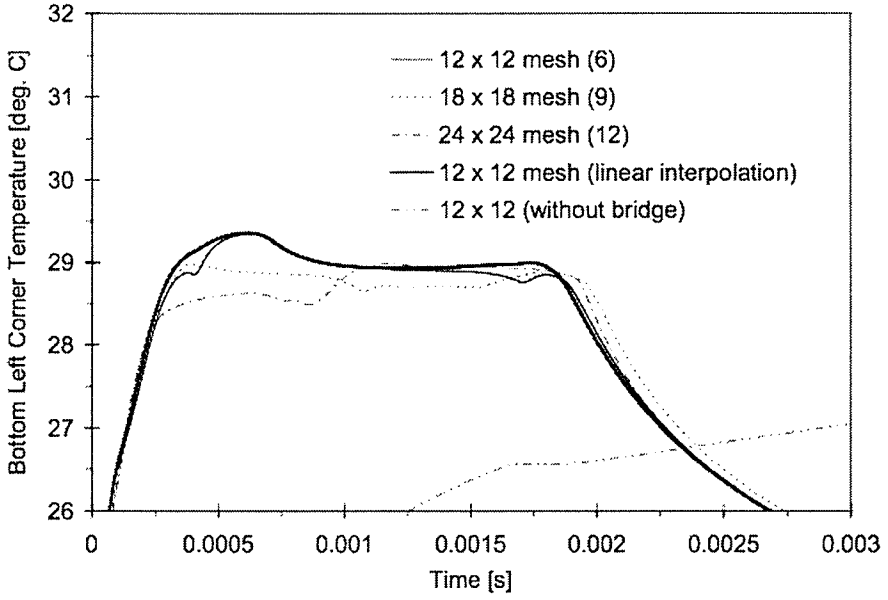

Figure 5.29: Temperature of Left Corner of Droplet with Varying Grid Spacings.

the thermal bridge, the droplet displacement is delayed, since the thermocapillary force is reduced when the temperature is lower (see results of Figure 5.29).

This section has shown that the mesh density affects the time and frequency of oscillations in the temperature of the receding edge of the droplet. The overall receding temperature and the droplet displacement, however, are not significantly affected.

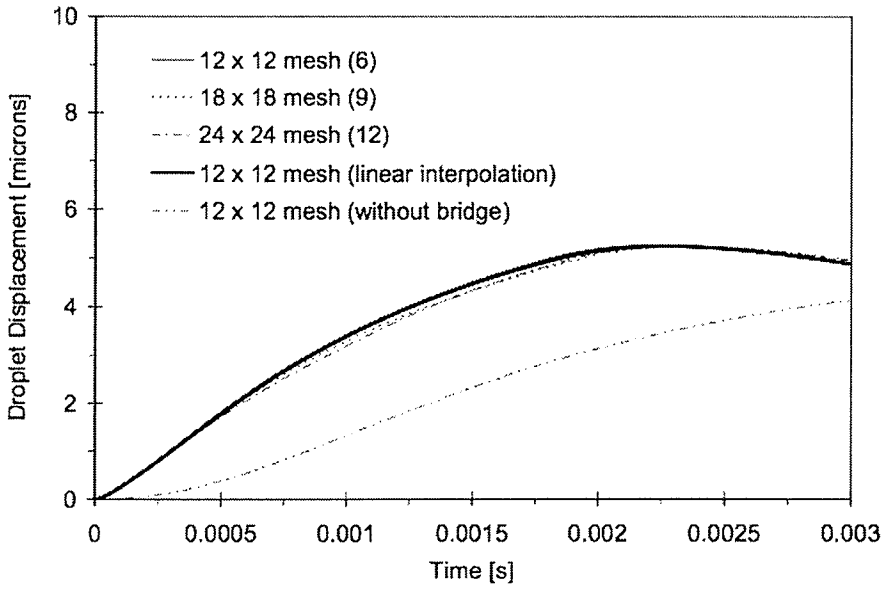

Figure 5.30: Droplet Displacement with Various Grid Spacings.

5.6.3 Coupled Velocity and Capillary Pressure at the Moving Droplet / Air Interface

Figure 5.31 shows the pressure distribution along the droplet / air interfaces. The values have been normalized by the average interface pressure. Results after 10, 20, 30 40, 50, 100, 150, 200, 250, 300, 350, 400, 600, 800, 1000 and 1500 time steps are plotted. It can be seen that the normalized pressure distribution is independent of the time step (bulk droplet velocity). This suggests that the pressure distribution is reaching a quasi-steady distribution for each time step in the simulation. For sufficiently small droplets and sufficiently slow heating of the micro-droplet, it appears that the velocity distributions collapse onto a single profile, which depends only on the driving pressure of the micro-droplet (thermocapillary pressure plus external air pressure).

The bulk velocity was plotted against the instantaneous pressure difference across the channel. In Figure 5.32, the plot appears to be linear, thereby indicating a direct relationship between the average pressure difference across the droplet and the bulk droplet velocity. For a given time step, this indicates that the bulk droplet velocity can be determined from the steady state Poiseuille velocity distribution, based on a given pressure difference across the micro-droplet. The expression for the steady-state velocity distribution for laminar Poiseuille flow may be written as

$$u(y) = -\frac{d^2}{2\mu}\frac{\partial P}{\partial x}\left[\left(\frac{y}{d}\right)^2 - \frac{y}{d}\right] \tag{5.26}$$

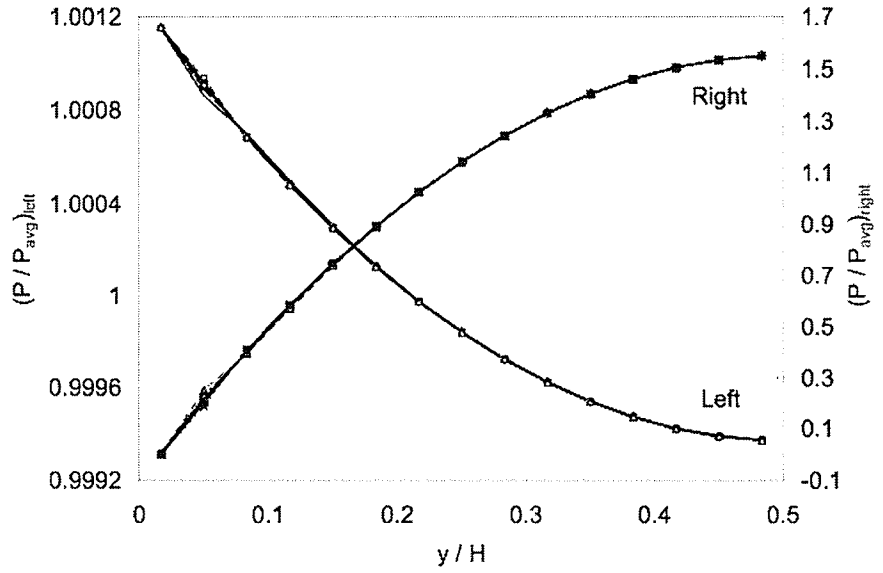

Figure 5.31: Transient Normalized Pressure Distributions Along Droplet / Air Interfaces.

from which u_b can be determined as

$$u_b = -\frac{d^2}{12\mu\Delta x}\Delta P \tag{5.27}$$

Equation (5.27) is depicted in Figure 5.32 as a dashed line. Substituting the problem parameters into Eq. (5.27) yields a bulk velocity of $u_b = -3.5637\Delta P$, where the value of Δx is the distance between the left-most and right-most pressure nodal points (not the length of the droplet). A curve fit of the FVM data using Microsoft Excel suggests a line with $u_b = -3.4854\Delta P$. The steady-state bulk velocities exceed the predicted values by about 2.25 percent for the given problem parameters. Decreasing the mass of the droplet or the magnitude of the heat source would likely enlarge this difference.

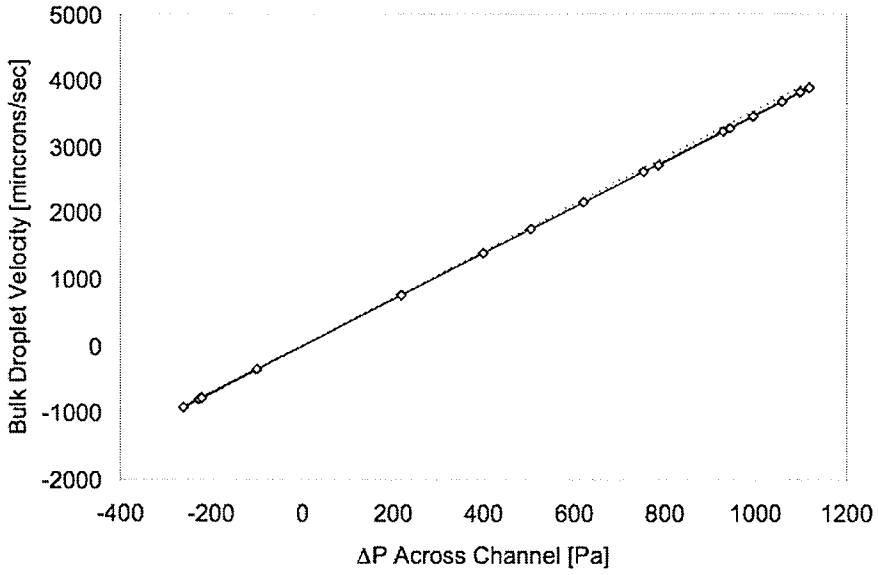

Figure 5.32: Transient Normalized Pressure Distributions Along Droplet / Air Interfaces.

The vertical pressure difference between the channel wall and the channel centerline ($\Delta P_v = P_{cl} P_w$) along the advancing and receding edges of the droplet was examined. Figure 5.33 shows how $(P_v)_L$ and $(-\Delta P_v)_R$ vary with the bulk velocity of the droplet. The curves appear to be overlapping straight lines. Pressure profiles scaling directly with the average pressures along the droplet edges (see Figure 5.31) indicate that the pressure required to redirect the flow from the channel wall to the channel centerline varies directly with the bulk droplet velocity.

5.7 Effects of Wall Slip

The effect of wall slip on thermocapillary pumping in closed-end microchannels was examined. A slip formulation proposed by Choi et. al. [58] was incorporated into

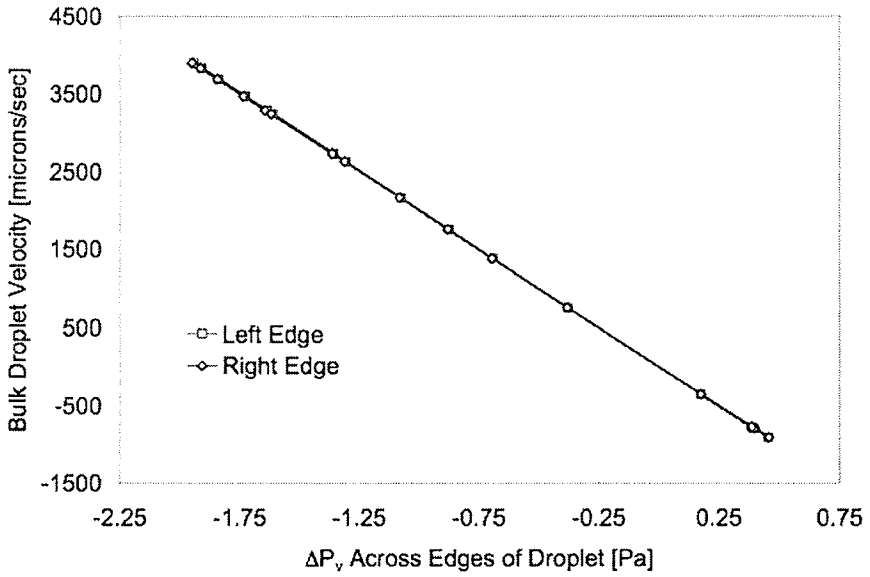

Figure 5.33: Comparison of the Pressure Differences Across the Droplet / Air Interfaces.

the numerical model. A generic dependence of the slip length on the shear rate was assumed. Volume flow rates were experimentally determined and compared with values predicted by the Navier-Stokes equations. This procedure allowed the slip velocity to be determined from experimental quantities. The formulation suggests that the slip length has a power-law dependence on shear rate,

$$\delta = A\dot{\gamma}^B \tag{5.28}$$

The values of A and B were determined from experimental data of flow rate versus pressure characteristics. The data was collectively fitted to the analytical model of Eq. (5.28) using a least-squares minimization to determine values of A and B. For hydrophilic droplets, these values are $A = 0.059$ and $B = 0.485$. The authors further

suggest $B = 0.5$, for which the mean-square error is effectively identical.

In a later paper [59], Choi et. al. suggest that upon inspection of the data, it is possible (and in fact more likely) that the shear-length depends linearly on the shear rate,

$$\delta = A + B\dot{\gamma} \tag{5.29}$$

The values of A and B were determined from experimental data of flow rate versus pressure characteristics. The data was collectively fitted to the analytical model of Eq. (5.29) using a least-squares minimization to determine values of A and B. For hydrophilic droplets, these values are $A = 0.6$ and $B = 1.1 \times 10^{-4}$. The authors noted that the power-law dependence on shear rate was found to fit the experimental data slightly better than the linear dependence. However an exponent of $B = 0.5$ seemed somewhat arbitrary and the linear dependence was deemed more plausible.

The effect of slip at the channel walls on TCP in closed-end microchannels was exmamined using the formulations of both Eqs. (5.28) and (5.29). TCP was simulated in microchannels of three different heights: 2 μm, 200 nm and 20 nm. Other simulation parameters are shown in table 5.6. The maximum shear rate for the 200 nm channel is approximately 14,000. It should be noted that the parameters in Eqs. (5.28) and (5.29) were fitted for shear rates between 0 and 125,000, with little experimental data for shear rates below 14,000. The simulated slip length and slip velocity dependencies on shear rate are shown in Figures 5.34 and 5.35, respectively. It is clear from the Figures that the power law formulation will more greatly affect the droplet displacement than the linear displacement assumption. The effect of slip at the wall on the droplet displacement characteristics may be seen in Figure 5.36. The power law formulation predicts that the droplet will reach a given displacement

Table 5.6: Simulation Parameters for Slip Flow in Microchanels.

Property	Value
Density of Droplet	998.0 kg/m^3
Thermal Conductivity of Droplet	0.606 W/mK
Specific Heat of Droplet	4181.0 J/kgK
Kinematic Visocity of Droplet	595×10^{-6} Ns/m^2
Density of Air	1.1614 kg/m^3
Thermal Conductivity of Air	0.0623 W/mK
Specific Heat of Air	1007.0 J/kgK
Density of Substrate	2500.0 kg/m^3
Thermal Conductivity of Substrate	0.96 W/mK
Specific Heat of Substrate	837.0 J/kgK
Channel Length	2000×10^{-6} m
Channel Height	20 / 200 / 2000 nm
Channel Depth	100μm

(5 microns) earlier than values from the linear formulation.

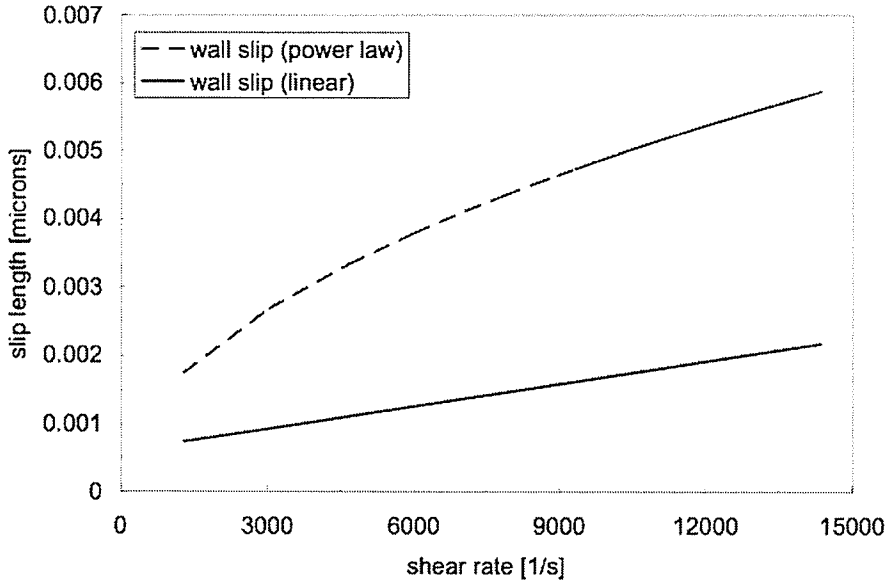

Figure 5.34: Slip Length Dependence on Shear Rate.

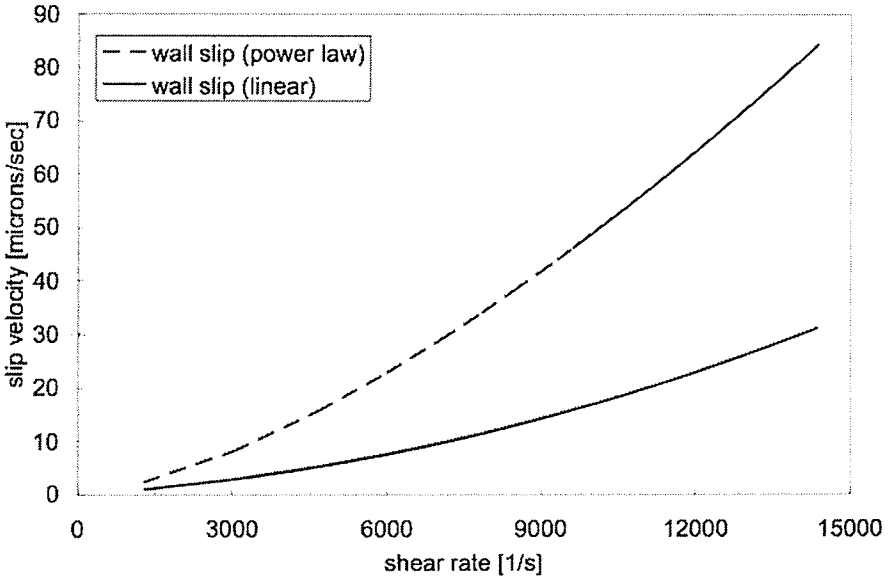

Figure 5.35: Slip Velocity Dependence on Shear Rate.

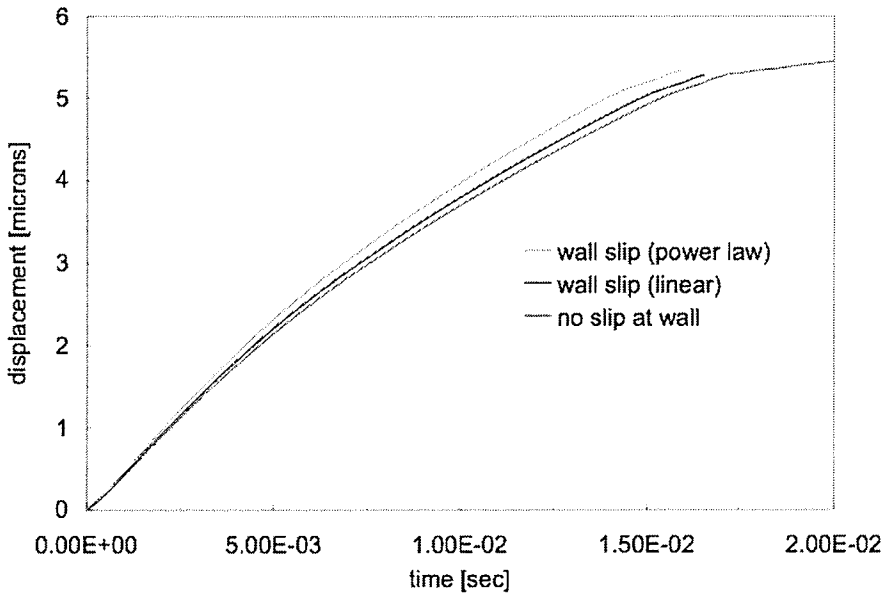

Figure 5.36: The Effect of Wall Slip on Droplet Displacement.

Chapter 6

Conclusions and Recommendations for future Research

6.1 Conclusions

This thesis has investigated thermocapillary pumping in closed-end microchannels, as a foundation for driving a micro heat engine. Droplets within microchannels are differentially heated, thereby inducing a surface tension imbalance across the droplet ends. The difference in capillary pressures across the droplet produces droplet motion. The air chambers surrounding the droplet are compressed or expanded, thereby causing changes in air pressure. The pressure changes flex piezoelectic membranes, across which electrical potentials develop. Conditioning circuitry converts the electical potential into an electric current, which may be used to charge a battery or power a microdevice.

A prototype of a micro heat engine proposed in chapter 2 (without the piezoelectric

membranes) was manufactured in the Nanofabrication Laboratory at the University of Manitoba. The purpose of the prototype was to determine practical feasibility of the manufacturing processes. Fluid access holes, ranging in width from 14 to 112 μm, were plasma etched to a depth of 20μm. Plasma etching to a depth of 20μm had not yet been attempted at the University of Manitoba. Four of eight holes etched completely through the wafer, with no correlation between hole width and penetration success. The walls of the holes tapered inward at an angle of approximately 57.2°, as opposed to the expected angle of 90°. This likely arose from the unusually large depth of the etch. Plasma may not be able to effectively penetrate such deep and narrow cavities. The plasma chemically etches the silicon, but it also mechanically etches by a bombardment process. The base of the hole may have been shadowed by the walls of the hole, thereby contributing to incomplete etching in the bottom corners. The surfaces of the microchannels were sufficiently smooth, so they were undetectable by the alpha step. Water droplets deposited within any of the trenches were imbibed into the corresponding microchanels without any external pumping.

A KOH etch was determined to be a suitable method of creating backside trenches for wafer thinning the application of resistance heaters and the boring of fluid access holes. The etch rate was accurately predicted to be 1.07μm/minute and the silicon was thinned down to 23μm (target was 22μm). The etch rate was sufficiently fast to yield very smooth trenches of uniform thickness. Aluminum and chrome were thermally evaporated onto the surface of the silicon wafer to become heaters and heater leads. The aluminum heater leads were succesffully etched on the backsides of the wafers along the slopes of the trench walls to the trench bases. The thin chrome heaters, however, were discontinuous in many places. The photresist for lithography

flowed unevenly into the trenches during spincoating. Thick regions of photoresist were not exposed properly, leading to discontinuities in the photresist mask. There was also evidence that the etchant undercut the thin photoresist mask, leading to further discontinuities. These problems can be alleviated in the future by employing wider heaters.

An experimental examination of thermocapillary pumping was performed using polymer-based microchannels manufactured by Epigem. A heating strip affixed to a 30 mm delay chip was chosen for experimentation because it provided the longest straight section of microchannel, onto which the microcsope could focus. The fluid was injected and positioned within the microcannel using a Kloehn V6 syringe drive module. Smooth fluid motion was realizable within the flexible tubing connected to the board, as well as within the microchannels. The receding edge of the droplet was positioned over the heating strip using the syringe drive module. A heater temperature of 35°C yielded a droplet displacement of approximately 83μm. The droplet motion was recorded using Particle Image Velocimetry (PIV) software. This recording revealed that the interface of the droplet did not remain backside to the microchannel walls and the droplet flowed in an irregular manner. It was the relatively large surface roughness caused by the manufacturing procedure that leads to this irregular droplet motion. The surface of the microchannels have a surface roughness that was undetectable with the alpha step in the Nanofabriaction Lab.

A theoretical model was developed based on an approximation whereby a micro-droplet is treated as a non-deformable slug transported through a closed-end microchannel. A heat source located at the receding edge of the micro-droplet generated a thermocapillary force and fluid motion occured. Newton's Second Law of Motion

was used to predict the droplet motion. Thermocapillary forces, external air forces and frictional drag forces were considered. The thermocapillary forces depend on the droplet temperature distribution. The droplet / air regions were approximated by two adjacent quasi one-dimensional semi-infinite domains. This approximation was supported by full numerical simulations, which indicated that convective cooling at the interface between the substrate and its surroundings is small compared to axial conduction across the domain. During droplet transport, the enclosed air section on the right side was compressed and the air on the left side was expanded. As a result, the rightward acceleration of the droplet was reduced, relative to a corresponding case for droplet motion in an open-ended channel. The resulting external air pressures were calculated from the ideal gas law. Frictional resistance also reduced the rightward acceleration of the droplet. The frictional drag force was approximated from a comparison of the droplet's bulk velocity and an assumed steady-state Poiseuille velocity profile. Based on the resulting net force (F), the droplet velocity (u) and displacement (x) were determined from temporal integration over a discrete time step, Δt, of Newton's Second Law.

The theoretical model was shown to accurately predict droplet motion when accurate temperature data was available. When temperature data was provided from numerical simulations, the droplet displacement history was nearly identical to that predicted by the full numerical simulation. The complexity of the problem and the unknown conjugate boundary condition at the substrate / droplet interface made accurate temperature predictions difficult. Furthermore, the composite nature of the domain rendered any general solution difficult. The theoretically predicted thermocapillary pumping trends were similar to those of the full numerical simulation. This

indicated that the theoretical model may be used to predict the effects of varying thermophysical properties of the fluids (or substrate), the geometry of the components or the heater boundary conditions.

A numerical formulation was also developed to predict thermocapillary pumping in closed-end microchannels. The formulation used a finite volume method (FVM) to discretize the governing equations and a SIMPLEC solution procedure. Unlike the theoretical model, the numerical formulation solved the internal flow within the accelerating droplet and the heat transfer throughout the entire domain, with temperature boundary conditions applied only along the outer boundary of the domain. The numerical formulation also incorporated a thermal bridge, which is a laterally insulated strip of highly-conductive metal that directs heat from the heat source towards one edge of the droplet.

The pressure and velocity distribution within the droplet were solved on a momentum equation mesh, while the temperature distribution was solved on a separate temperature equation mesh. Non-uniform Bezier grids, based on Bernstein polynomials, provided grid refinement near the phase boundaries. The momentum equation mesh overlapped the droplet portion of the temperature equation mesh, with pressure nodal points from the momentum equation mesh aligned with temperature nodal points from the temperature equation mesh. When the droplet moved within the microchannel, the temperature equation mesh was regenerated. The droplet portion of the mesh translated, so it remained beneath the momentum equation mesh, but it remained undistorted. The mesh of the upstream air chamber was stretched to accommodate the droplet translation, while the mesh of the downstream air chamber was compressed. The substrate mesh was distorted to maintain alignment with the

control volumes of the adjacent fluid phases.

Dirichlet pressure boundary conditions were specified in control volumes at the droplet/air/substrate interfaces. The pressures were iterated until the average pressure difference across the droplet equaled the sum of the external and thermocapillary pressures across the droplet. Dirichlet u-velocity boundary conditions were specified along the droplet/air interfaces. The velocity was chosen so it would yield the same average mass flow rate as the value caused by the specified corner pressures from the previous iteration. Specifying the same value along the entire interface ensured that the droplet remained undistorted.

The droplet portion of the temperature mesh exactly matched the pressure momentum equation mesh, because the velocity field (predicted on the momentum equation mesh) was used in the advection terms of the temperature equation (predicted on the temperature equation mesh). Conjugate boundary conditions were needed for implicit coupling between heat conduction in the substrate and convection in the fluids. The heat fluxes through adjacent phases must be equal, thereby requiring discontinuous temperature gradients along phase boundaries. Zero-thickness control volumes were implemented along all phase boundaries, with temperature nodal points located along the phase boundaries. The zero-thickness control volumes successfully applied the correct boundary conditions without requiring special consideration. It was verified that the resulting heat fluxes through adjacent phases were equal.

A thermal bridge was implemented to effetively transfer heat from an external source to the receding edge of the droplet, while minimizing lateral heat flow into the substrate. Special attention was required when calculating the temperature field near the thermal bridge, where control volumes are composed of several materials and they

have composition changes with each time step. The assumption of a constant heat flux through these composite control volumes was made to approximate the temperature profile between nodal points and specify the temperatures within the thermal bridge and surrounding insulation. Simulations indicated that the formulation did not yield significantly different driving temperatures or droplet displacements than results using linear interolation bewteen nodes. Different mesh densities produced slight variations in the temperature profiles by changing both when and how often nodal points were assigned to new phases.

TCP in open-ended microchannels was simulated for a variety of fixed temperature differences in a rectangular microchannel. The resulting steady-state bulk droplet velocities were compared with experimental results of Sammarco and Burns [49]. The slopes of the simulated (present work) and theoretical (Sammarco and Burns [49]) velocity vs. temperature difference curves were identical, but the minimum temperature differences required to overcome surface tension hysteresis differed by approximately 2 degrees. Both simulated and theoretical curves were offset along the temperature difference axis, with respect to the experimental data. It is unclear why the experimentally-determined minimum temperature difference to overcome surface tension hysteresis did not agree with the theoretical value. Excellent agreement between other predicted results and the exerimental suggest that the numerical formulation could accurately predict thermocapillary pumping, given a fixed temperature difference accross the droplet in an open-ended microchannel.

Additional validation was performed by comparing simulated results against experimental data of Sammarco and Burns [49] for mineral oil droplets pumped through rectangular microchannels using an applied external pressure. The simulated veloc-

ities agreed well with the proposed theory, but they were shifted with respect to the applied pressure. It is unclear why the theory line did not coincide with the experimental data of Sammarco and Burns [49]. The slope of the theory and simulation curves closely matched results of the experimental data, although the velocity appeared to increase slightly slower than predicted, when the driving pressure is increased. This result could arise from the fact that the dynamic contact angles vary with velocity. Errors in contact angle measurement may be responsible for the deviation of experimental velocities from their theoretical values.

The droplet motion predicted by the theoretical model was compared against results of the numerical formulation. The theoretical model slightly over-predicted the temperature of the receding edge of the droplet during the heating period. This led to over-prediction of the droplet displacement and external pressure. The cooling period was also reasonably well predicted, with the theoretical model under-predicting the droplet displacement (i.e. droplet returned too rapidly).

The simulations revealed that the normalized pressure distributions along the droplet/air interfaces were independant of time, although the pressure difference between the wall and droplet centerline increases with droplet velocity. The bulk droplet velocity was shown to match the steady-state value. The interface pressure difference required to reverse fluid motion scaled linearly with the droplet"s bulk velocity. All of these observations indicate quasi-steady state droplet dynamics for droplet size and driving temperature difference considered in this thesis.

The effects of a linear and a power-law slip model on thermocapillary pumping in closed-end microchannels were examined. It was found that the slip velocity and slip length predicted by the power law model were larger than results of the linear

model. Both models increased the droplet velocitie and thus reduced cycle times. It is thus concluded that slip within microchannels would be beneficial when using thermocapillary pumping to drive a micro heat engine.

The theoretical and numerical predictions of droplet motion compare well with experimental and theoretical results for thermocapillary pumping in open-ended microchannels. Additionally, trends predicted by the theoretical model agree with those predicted by the numerical formulation for thermocapillary pumping in closed-end microchannels. It may be concluded that a micro heat engine may be manufactured and driven by thermocapillary pumping in closed-end microchannels. Ideally, a waste heat source could provide the required heat input.

6.2 Recommendations for Future Research

Experimentation, prototype manufacturing and numerical simulations, as well as examination of the literature, suggest that a micro heat engine can be constructed and driven by thermocapillary pumping of liquid droplets in closed-end microchannels. In order to prove this hypothesis, the micro heat engine developed in this thesis needs to be manufactured, including piezoelectric membranes. It is suggested that this task should be contracted out to a company that specializes in the manufacturing of microdevices. It should have appropriate facilites, equipment and staff to take the full design to completion.

The micro heat engine proposed in this thesis would require a sufficiently high efficiency for it to be an economically viable alternative for powering microdevices, replacing batteries or increasing the efficiency of devices such as laptop computers

or hybrid vehicles. The extent to which the piezoelectric membranes will deflect and the amount of power production during flexure is unknown. To this end, the power output of the manufactured micro heat engine should be measured and efficiencies should be determined.

The droplet dynamics should be measured during operation of the micro heat engine in order to validate the results of the numerical formulation. Micro Particle Image Velocimetry (micro-PIV) measurements permit measurement of the internal recirculation within the droplet. The challenging experiments should be carried out to determine whether slip exists at the microchannel walls. If slip conditions exist, the dependence on channel size and effects on the performance of the micro heat engine should be determined. It should be stressed that these goals will not be easily achieved, if indeed they can be achieved with currently available technology.

Bibliography

[1] [Online]. Available: http://www.ipt.arc.nasa.gov/nanotechnology.html

[2] The race to commercialize the ultra-small. [Online]. Available: http://www.the-infoshop.com/study/tak14962_nanotechnology_mems.html

[3] K. Coleman. Nanotechnology and the fight against terrorism. [Online]. Available: http://www.locationintelligence.net/articles/375.html

[4] M. Gad-el Hak, "The fluid mechanics of microdevices - the freeman scholar lecture," *ASME Journal of Fluids Engineering*, vol. 121, pp. 5–33, 1999.

[5] S. Wu, J. Main, Y. C. Tai, and C. M. Ho, "Micro heat exchanger using mems impinging jets," in *Proceeding of the 12th Annual International Worksho[on Micro Electro Mechanical Systems*, Orlando, FL, January 1999, pp. 191–176.

[6] K. Vafai and L. Zhu, "Analysis of a two-layered micro channel heat sink concept in electronic cooling," *International Journal of Heat and Mass Transfer*, vol. 42, no. 12, pp. 2287–2297, 1999.

[7] A. J. Tudos, G. A. J. Besselink, and R. B. M. Schasfoort, "Trends in miniaturized total analysis systems for point-of-care testing in clinical chemistry," *Lab on a Chip*, vol. 1, pp. 83–95, 2001.

[8] G. F. Naterer, "Adaptive surface micro-profiling for microfluidic energy exchange," *AIAA Journal of Thermophysics and Heat Transfer*, vol. 18, no. 4, pp. 494–501, 2004.

[9] S. Whalen, M. Thompson, D. Bahr, and R. Richards, "Design, fabrication and testing of the p3 micro heat engine," *Sensors and Actuators*, vol. 104, pp. 200–208, 2003.

[10] G. F. Naterer, P. S. Glockner, S. R. Chomokovski, G. Richardson, and G. Venn, "Surface micro-grooves for near-wall exergy and flow control: Application to aircraft intake de-icing," *Journal of Micromechanics and Microengineering*, vol. 15, pp. 501–513, 2005.

[11] S. Lim and H. Choi, "Optimal shape design of a pressure driven curved micro channel," in *AIAA Paper 2004-624, AIAA 42nd Aerospace Sciences Meeting and Exhibit*, Reno, NV, 2004.

[12] P. Dutta, A. Beskok, and T. C. Warburton, "Electroosmotic flow control in complex microgeometries," *Journal of Microelectromechanical Systems*, vol. 11, no. 1, pp. 36–44, 02.

[13] S. A. Jacobsen and A. H. Epstein, "An informal survey of micro power systems," in *The International Symposium on Micro-Mechanical Engineering*, December 2003.

[14] E. Smalley. Engine fires up electrical devices. [Online]. Available: http://www.trnmag.com/Stories/053001/Engine_fires_up_electrical_devices_053001.html

[15] E. Hardy. Six hot technologies that could profoundly change handhelds. [Online]. Available: http://www.brighthand.com/default.asp?newsID=11468

[16] A. R. C. Inc. Alberta research council reaches major milestone in development of micro fuel cell technology. [Online]. Available: http://www.scienceblog.com/community/older/2002/A/2002919.html

[17] J. Yang, F. Lu, L. W. Kostiuk, and D. Y. Kwok, "Electrokinetic microchannel battery by means of electrokinetic and microfluidic phenomena," *ournal of Micromechanics and Microengineering*, vol. 13, pp. 963 – 970, 2003.

[18] A. Hoover. An "aaaaaaaaa" battery? uf researchers make progress on tiny cell. [Online]. Available: http://news.ufl.edu/2002/10/09/nanobattery/

[19] What is mems technology? [Online]. Available: http://www.memsnet.org/mems/what-is.html

[20] C. J. Kim, *Chapter 18: The Use of Surface Tension for the Design of MEMS Actuators*, S. M. Hsu and Z. C. Ying, Eds. Boston, MA: Kluwer Academic Publishers, 2003.

[21] V. Singhal, S. V. Garimella, and A. Raman, "Microscale pumping techniques for microchannel cooling systems," *Applied Mechanics reviews*, vol. 57, pp. 191–221, 2004.

[22] M. Mala and D. Li, "Flow characteristics of water through microtubes," *International Journal of Heat and Fluid Flow*, vol. 20, pp. 142–148, 1999.

[23] W. Qu, M. Mala, and D. Li, "Pressure-driven water flows in trapezoidal silicon microchannels," *International Journal of Heat and Mass Transfer*, vol. 43, pp. 353–364, 2000.

[24] J. Lee and C. J. Kim, "Liquid micromotor driven by continuous electrowetting," in *Proceedings of IEEE MEMS Conference*, Heidelberg, Germany, 1998, pp. 538–543.

[25] ——, "Microactuation by continuous electrowetting phenomenon and deep silicon RIE process," in *Proceedings of MEMS (DSC vol. 66), ASME IMECE Conference*, Anaheim, CA, November 1998, pp. 475–480.

[26] K. S. Yun, I. J. Cho, J. U. Bu, C. J. Kim, and E. Yoon, "A surface-tension driven micropump for low voltage and low power operations," *ASME Journal of Microelectromechanical Systems*, vol. 11, no. 5, pp. 454–461, October 2002.

[27] S. Gurrum, S. Murthyl, and Y. Joshi, "Numerical simulation of thermocapillary pumping using a level set method," in *Proceedings of the 5th ISHTM/ASME Heat and Mass Transfer Conference*, Kolkata, India, January 3-5 2002.

[28] T. S. Sammarco and M. A. Burns, "Heat transfer analysis of microfabricated thermocapillary pumping and reaction devices," *Journal of Micromechanics and Microengineering*, vol. 10, pp. 42–55, 2000.

[29] H. Yoshida, M. Saito, H. Toda, and R. Haraguchi, "Performance analysis on micropump system driven by marangoni effect," in *Proceedings of the Twelfth International Heat Transfer Conference*, Grenoble, France, August 18 - 23 2002.

[30] G. F. Naterer, "Pressure weighted upwinding for flow induced force predictions: Application to iced surfaces," *International Journal for Numerical Methods in Fluids*, vol. 44, no. 9, pp. 927–956, 2004.

[31] ——, *Heat Transfer in Single and Multiphase Systems.* Boca Raton, FL: CRC Press, 2002.

[32] ——, "Sub-grid volumetric quadrature accuracy for transient compressible flow predictions," *International Journal for Numerical Methods in Fluids*, vol. 25, pp. 143–149, 1997.

[33] G. F. Naterer and D. Rinn, "Toward entropy detection of anomalous mass and momentum exchange in incompressible fluid flow," *International Journal for Numerical Methods in Fluids*, vol. 39, no. 11, pp. 1013–1036, 2002.

[34] R. R. Riehl, J. M. Ochterbeck, and P. Seleghim, "Effects of condensation in microchannels with a porous boundary: Analytical investigation on heat transfer and meniscus shape," *Journal of the Brazilian Society of Mechanical Sciences*, vol. 24, no. 3, pp. 186–193, July 2002.

[35] A. K. Sen and S. H. Davis, "Steady thermocapillary flows in two-dimensional slots," *Journal of Fluid Mechanics*, vol. 121, pp. 163–186, August 1982.

[36] G. F. Naterer, "Conduction shape factors of long polygonal fibres in a matrix," *Numerical Heat Transfer A*, vol. 30, no. 7, pp. 721–738, 1996.

[37] C. W. Hirt, "Thermocapillary sample problems," Flow Science Inc., Santa Fe, NM, Technical Report FSI-98-00-TN47, March, 1998.

[38] S. Troian, "Thermocapillary flow on patterned surfaces: A design concept for microfluidic transport," in *ASME IMECE Microfluidics Symposium*, New York, November 2001.

[39] A. A. Darhuber, J. Z. Chen, and J. M. Davis, "A study of mixing in thermocapillary flows on micropattered surfaces," *Philosophical Transactions: Mathematical, Physical and Engineering Sciences*, vol. 362, no. 1818, pp. 1037–1058, May 2004.

[40] B. S. Dandapat, B. Santra, and H. I. Andersson, "Thermocapillarity in a liquid film on an unsteady stretching surface," *International Journal of Heat and Mass Transfer*, vol. 46, pp. 3009–3015, 2003.

[41] S. M. Ghiaasiaan and R. C. Chedester, "Boiling incipience in microchannels," *International Journal of Heat and Mass Transfer*, vol. 45, no. 23, pp. 4599–4606, 2002.

[42] R. C. Chedester and S. M. Ghiaasiaan, "A proposed mechanism for hydrodynamically-controlled onset of significant void in microtubes," *International Journal of Heat and Fluid Flow*, vol. 23, no. 6, pp. 769–775, 2002.

[43] N. T. Nguyen and S. T. Wereley, *Fundamentals of Applications of Microfluidics.* Norwood, MA: Artech House Publishers, 2002.

[44] M. J. DeBar and D. Liepmann, "Fabrication and performance testing of a steady thermocapillary pump with no moving parts," in *Proceedings of the Fifteenth IEEE International Conference on Micro Electro Mechanical Systems*, Las Vegas, NV, January 20-24 2002, pp. 109–112.

[45] V. Ha and C. Lai, "Onset of marangoni instability of a two-component evaporating droplet," *International Journal of Heat and Mass Transfer*, vol. 45, pp. 5143–5158, 2002.

[46] R. Xu and G. F. Naterer, "Controlled interface acceleration in unidirectional solidification," *International Journal of Heat and Mass Transfer*, vol. 47, no. 22, pp. 4821–4832, 2004.

[47] G. F. Naterer, "Establishing heat - entropy analogies for interface tracking in phase change heat transfer with fluid flow," *International Journal of Heat and Mass Transfer*, vol. 44, no. 15, pp. 2903–2916, 2001.

[48] G. F. Naterer, W. Hendradjit, K. J. Ahn, and J. E. S. Venart, "Near-wall microlayer evaporation analysis and experimental study of nucleate pool boiling on inclined surfaces," *ASME Journal of Heat Transfer*, vol. 120, no. 3, pp. 641–653, 1998.

[49] T. S. Sammarco and M. A. Burns, "Thermocapillary pumping of discrete droplets in microfabricated analysis devices," *AIChE*, vol. 45, pp. 350–366, 1999.

[50] G. P. Sasmal and J. I. Hochstein, "Marangoni convection with a curved and deforming free surface in a cavity," *ASME Journal of Fluids Engineering*, vol. 116, p. 577, 1994.

[51] H. Togo, M. Sato, and F. Shimokawa, "Multi-element thermo-capillary optical switch and sub-nanoliter oil injection for its fabrication," in *Proceedings of the IEEE MEMS Conference*, Orlando, FL, 1999, pp. 418–423.

[52] W. Salhala and E. Zussman, "Nanowire assembly using microfluidics: An experimental investigation," in *ICTAM Conference*, Warsaw, Poland, August 15-21 2004.

[53] M. R. Clements, "Microfluidic handling on a thermally responsive surface," Master's thesis, UWEE Technical Report UWEETR-2003-0016, Department of Electrical Engineering, University of Washington, 2003.

[54] S. V. Patankar, *Numerical Heat Transfer and Fluid Flow*, ser. Series in Computational and Physical Processes in Mechanics and Thermal Sciences, W. J. Minkowycz and E. M. Sparrows, Eds. Hemisphere Publishing Corporation, 1980.

[55] H. S. Carslaw and J. C. Haeger, *Conduction of Heat in Solids.* Oxford University Press, 1959.

[56] M. Richter, P. Woias, and W. D., "Microchannels for applications in liquid dosin and flow-rate measurement," *Sensors and Actuators A*, vol. 62, pp. 480–483, 1997.

[57] W. Urbanek, J. Zemel, and H. Bau, "An investigation of the temperature dependence of poiseuille numbers in microchannel flow," *Journal of Micromechanics and Microengineering*, vol. 3, pp. 206–208, 1993.

[58] C.-H. Choi, K. J. A. Westin, and K. S. Breuer, "To slip or not to slip - water flows in hhydrophilic and hydrophobic microchannels," in *2002 International Mechanical Engineering Conference and Exposition*, New Orleans, Louisiana, USA, November 13-16 2002, pp. 1–8.

[59] ——, "Apparent slip flows in hydrophilic and hydrophobic microchannels," *Physics of Fluids*, vol. 15, no. 10, pp. 2897–2902, October 2003.